NASA TECHNICAL NOTE

NASA TN D-5159

C. 1

NASA TN D-5159

LONGITUDINAL VIBRATION CHARACTERISTICS OF 1/10-SCALE APOLLO/SATURN V REPLICA MODEL

by Larry D. Pinson and H. Wayne Leonard

Langley Research Center
Langley Station, Hampton, Va.

NATIONAL AERONAUTICS AND SPACE ADMINISTRATION • WASHINGTON, D. C. • APRIL 1969

LONGITUDINAL VIBRATION CHARACTERISTICS OF 1/10-SCALE APOLLO/SATURN V REPLICA MODEL

By Larry D. Pinson and H. Wayne Leonard

Langley Research Center
Langley Station, Hampton, Va.

NATIONAL AERONAUTICS AND SPACE ADMINISTRATION

For sale by the Clearinghouse for Federal Scientific and Technical Information
Springfield, Virginia 22151 – CFSTI price $3.00

LONGITUDINAL VIBRATION CHARACTERISTICS OF 1/10-SCALE APOLLO/SATURN V REPLICA MODEL

By Larry D. Pinson and H. Wayne Leonard
Langley Research Center

SUMMARY

A 1/10-scale replica model of the Apollo/Saturn V launch vehicle has been tested and analyzed to determine its free-free, longitudinal vibration characteristics during first-stage burn. A lumped-parameter analysis was employed to assess the applicability of such an analysis to a complex Saturn V type of launch vehicle and to investigate the effects of tank orthotropy and the method of representing the mass of contained liquids on the calculated natural modes and frequencies of the system. An approximate theory which accounts for tank wall orthotropy is developed for the calculation of springs associated with liquid-tank systems. A simple analysis is presented which shows that the actual value of the mass of the contained liquid may not be the correct value for incorporation into a lumped-parameter analysis. Model test results are presented for first-stage propellant loading conditions corresponding to several time points during first-stage burn.

The experiment and analysis show generally good correlation in both frequency and deflection shape for structural modes; however, discrepancies are found when the system responds in either propellant modes or in coupled structural-propellant modes. The results also show that vehicle structural modes are less sensitive to shell orthotropy than are the modes involving significant liquid-tank interactions. Also, use of an analytical equivalent liquid mass value for contained liquids produces better agreement with experiment for the liquid-tank modes whereas actual liquid mass values produced better agreement for structural modes.

INTRODUCTION

As the size and complexity of space-flight launch systems have increased, the acquisition of reliable vibration data for use in control-system and loads-alleviation studies, payload environmental parameters, and Pogo instability studies has become increasingly difficult and expensive. Such data are usually obtained in two ways – by analysis and by ground tests of a full-scale prototype. The full-scale ground testing of

large boosters can involve large time and money expenditures and can create technical and logistics problems of such magnitude as to render this approach unattractive. Furthermore, data from full-scale tests must be preceded by design and construction of the prototype vehicle; hence, the data are not available until late in the vehicle development cycle. This late availability may reduce the usefulness of the full-scale data since many of the design and control parameters may have already been fixed. It is desirable that relatively inexpensive structural dynamics data be available early in the vehicle-development cycle in order to evaluate structural design proposals, to identify potential vibration problems, and to provide some reference for the evaluation of structural analysis techniques.

As one possible solution to the problem, the Langley Research Center has developed the concept of utilizing test results from detailed subscale models as a source of experimental vibration data. (See, for example, refs. 1 to 7.) Application of the dynamic-model concept has been further extended to the Saturn V vehicle. A 1/10-scale replica model, described in reference 8, which is essentially a reduced-scale replica of the prototype, and a 1/40-scale dynamic model, described in reference 9 in which the mass and bending stiffness properties are scaled, have been constructed and have been subjected to extensive ground vibration surveys in which natural frequencies, deflection shapes, and damping values have been determined for various boundary restraints, simulated flight times, and directions of excitation. Companion analytical studies have also been conducted, the correlation between experimental results and analytical predictions being used to evaluate and improve the analyses.

The purposes of this paper are to document the experimental free-free longitudinal vibration characteristics of the 1/10-scale Apollo-Saturn V model for the configuration and weight conditions corresponding to first-stage burn as part of the Saturn V model program and to present a lumped-parameter analysis which includes the effects of stiffening elements such as stringers and ring frames by basing spring-constant calculations on equivalent, orthotropic membrane properties of the model shell structure. Experimental response frequencies, deflection shapes, and damping values are presented and compared with natural frequencies and mode shapes predicted by the lumped-parameter analysis.

SYMBOLS

A area

a radius of cylinder

b	depth of lower bulkhead dome
b_1	depth of upper bulkhead dome
C_{ij}	element of orthotropic proportionality matrix
c	distance from liquid surface to upper bulkhead-cylinder intersection
d	deflection
E	Young's modulus
F	force
f	frequency
h	height of liquid
K	spring constant
k_n	spring constants where $n = 1,2, \ldots 32$
l	shell length
m	mass, also c/a
m_i	masses where $i = 1,2, \ldots 29$
$n = b/a$	
$n_1 = b_1/a$	
P	external load applied to shell
$p = l/a$	
$q = h/a$	

R_o	radius of cone at its base
r	radial coordinate
s	meridional coordinate
t	thickness of shell
u	displacement of shell in meridional direction
$\tilde{u}$	displacement of liquid in longitudinal direction
u_o	displacement of upper bulkhead-cylinder intersection in longitudinal direction
u_1	displacement of liquid center of gravity in longitudinal direction
V	volume of liquid
W	weight of liquid
w	displacement of shell normal to surface of shell
$\tilde{w}$	displacement of liquid in radial direction
x	longitudinal coordinate
α_{ij}	element of flexibility matrix
γ	unit weight of liquid
δ	deflection in x-direction
ϵ	strain
ζ	damping ratio
ν	Poisson's ratio

ρ mass density of liquid

φ_o cone angle

ω natural circular frequency

Subscripts:

a analytical

BH bulkhead

c cylinder

e experimental, also equivalent

f fluid

i isotropic

s meridional

o orthotropic

θ circumferential

Matrix notations:

[ ] denotes square matrix

{ } denotes column matrix

Dots over symbols denote derivatives with respect to time.

APPARATUS AND TEST PROCEDURE

1/10-Scale Model

The 1/10-scale model of the Apollo/Saturn V vehicle consists of three model booster stages, the model payload, and model launch escape system. The model

components are referred to by full-scale nomenclature: for example, S-IC, S-II, and S-IVB stages; instrument unit (IU); Saturn LM adapter (SLA); lunar module (LM); service module (SM); command module (CM); and launch escape system (LES). A complete description of the model, scaling concepts, solutions to typical problems encountered in design and fabrication, and illustrative examples of subscale components are presented in reference 8. Therefore, only a brief illustration of model components is included in this paper. The complete model is shown photographically in figure 1 and schematically in figure 2. Also noted on the schematic are the major structural joints and subassemblies. The model is 39.6 inches (1.01 meters) in diameter at the base and is 435.5 inches (11.06 meters) tall. Propellants and oxidizers are shown symbolically in their respective tanks with flight-vehicle nomenclature. Simulation of these liquids in the model is discussed in a subsequent paragraph.

Some details of the model construction are shown in figures 3 to 8. Figure 3 is a view of the base of the model with the engines removed. Some details of interest include actuator support assemblies for the outboard engines, engine fairings, S-IC fuel-tank lower bulkhead, thrust pads, and the cross-beam support for the center engine. Also noted is the point at which the excitation force was applied for the tests reported herein. Figure 4 shows the simulated LOX suction duct and a sketch illustrating installation of the duct in the model. Of particular interest here are the bellows assemblies in the lower section of the line. Resonances associated with the deflections of the simulated pressure-volume control (PVC) on the bellows springs is discussed subsequently. Figure 5 is a photograph of the complete S-II stage with major substructures identified and figure 6 shows a closeup view of one of the simulated S-II engine assemblies. The accelerometers shown are oriented in the pitch and yaw planes and were monitored during the tests to determine the magnitude, if any, of lateral engine responses. Figure 7 shows the complete S-IVB stage and is presented solely for the convenience of the reader. The SLA and the IU are shown in figure 8 with the model LM mounted inside the SLA.

Liquid Propellants

The onboard liquids, with the exception of the LH_2, were simulated with water. The actual specific gravities of these liquids are 0.80 for RP-1 and 1.14 for LOX. Proper control of tank water levels, as discussed in a subsequent section, then permitted the representation of the correct propellant weight but resulted in some deviation in mass distribution from that of the full-scale vehicle along the length of the model.

The low specific gravity of LH_2 dictated an extremely lightweight simulant having a specific gravity of 0.07. Small, hollow, styrene plastic beads with a specific gravity of 0.07 were procured and used as the LH_2 simulant. All tests were conducted with the tank ullage pressure at 10 psi (6.89×10^4 N/m^2).

Suspension System

The suspension system utilized to simulate the free-free flight condition consisted of four, symmetrically located, vertical, steel cables extending from overhead beams to a cradle at the base of the model. Each cable was 403 inches (10.24 meters) long and made of steel strands of 7 by 19 construction. The total weight including turnbuckles and end fittings was approximately 9 pounds (39.6 N) per cable. Figures 9 and 10 show the support cradle and illustrate the method of attachment to the model. Figure 9 is an oblique view of the cradle and model base as seen from below. The cradle is esentially a square frame constructed of aluminum tubing with I-beam projections extending diagonally outward from the corners of the frame. Also visible in figure 9 are the center engine gimbal through which the excitation force was applied, RP-1 tank fill line and liquid-level sight tube, S-IC thrust structure cross beams, and an inside view of one of the outer engine fairings. Figure 10 shows a horizontal view of the base of the suspended model. Visible in this figure are the adjustable clevises used to connect the cradle to one of the four holddown posts, the cable attachment to the cradle, the fill tube and sight glass for the RP-1 tank, and two of the support cables. Also visible is the single-drive dual-post jack used to position the model during cable hookup. The four support posts are used to support the model when it is not attached to the cables. The outboard engines, present during the tests, were not attached when the photos were made. The weight (18 lb (80 N)) of the cradle and shaker armature is approximately equal to the weight of the center engine which was removed during the tests. The length, diameter, and thus the cable spring constant were chosen so that the highest rigid-body natural frequency of the model on the cables (5.7 cps at S-IC burnout) was much lower than the lowest structural resonant frequency (30.9 cps).

Test Weights and S-IC Propellant Levels

Tests were performed for S-IC propellant loadings corresponding to five time points during the first-stage burn. The amount of liquid in each S-IC tank was scaled on a mass basis from full-scale values. Table I is a listing of the nominal weight conditions in terms of the ratio of liquid mass in the S-IC tankage to the S-IC liquid mass at lift-off (in percent). The table shows the weight of the liquid in each S-IC tank, the model station number of the liquid surface in each S-IC tank, and the total model weight for each time point. The percentage values listed are nominal values. Actual time points were: 146 seconds (burnout); 110 seconds (24 percent); maximum dynamic pressure (48 percent); 40 seconds (73 percent); and lift-off (100 percent).

Instrumentation

Instrumentation for the tests consisted of four basic groups: input force generator, acceleration response transducers, monitoring and recording equipment, and on-site data-analysis equipment. The input-force generator was a servocontrolled electromagnetic exciter acting through a force gage at the gimbal point of the S-IC center engine. The servocontrol maintained a constant, preselected, root-mean-square force level. The acceleration response transducers were Kistler model 303 servo accelerometers located on the model in such a manner as to permit determination of model deflection shapes in the longitudinal direction. A typical accelerometer attachment is shown in figure 11. The figure shows one of the accelerometers on the S-II aft skirt. This transducer was photographed during lateral tests; however, the attachment procedure is the same as that for longitudinal testing. A square solid-base plate was bonded to the surface of the model and four equally spaced holes were tapped in the base plate. An accelerometer mounting bracket was then attached to this plate, and finally the accelerometer was fitted through a hole in this bracket and fastened by bolting a retainer plate to the bracket. The equally spaced holes in the base plate permitted the orientation of the sensitive axis of the accelerometer to be easily changed by 90°. To accomplish the reorientation, the entire accelerometer—retainer-plate—mounting-bracket assembly is removed from the base plate, rotated 90°, and then refastened. In addition, structural elements such as engines, simulated LM, and selected internal structural members, were instrumented. The location and orientation of the sensitive axis of each primary transducer is shown in the drawing in figure 12. The transducers are represented by solid diamond symbols, the acute angle of the diamond corresponding to the direction of the sensitive axis. Station numbers are given referenced to the S-IC gimbal plane (which is station 10.0 inches (0.254 meter)).

Additional instrumentation consisting of strain and pressure transducers was selectively located in the S-IC structure. The locations, type, and orientation of these transducers are given in figure 13. Each upper bulkhead was fitted with a pressure transducer and three pairs of strain gages. The gages were located along a meridian of the bulkhead and were oriented so that each pair of gages could detect horizontal, or circumferential, strains and vertical, or meridional, strains. Each pair of gages was assigned an identification number and the letters H and V were used to denote horizontal or vertical sensitivity. The lower bulkheads were instrumented with pressure transducers and with six pairs of strain gages located on orthogonal meridians oriented to detect circumferential and meridional strains. Each tank was also instrumented at selected tank wall locations with longitudinally sensitive strain gages. Other strain gages were located at both ends of the LOX suction duct tunnel which contains the simulated LOX suction duct and on selected tension straps at the forward end of the S-IC forward skirt. A single pressure transducer was installed in the closure plate of the simulated PVC.

Data Acquisition and Reduction

The data-acquisition system used in this investigation is shown schematically in figure 14. Data signal cables from each transducer were connected to data group switches in prearranged combinations so that a desired group of 12 selected channels of information could be monitored on either the oscilloscope, meter, or x,y plotter. The data were recorded on analog tape for subsequent reduction by digital computer. Preliminary qualitative analyses were also performed on site.

All data recorded on analog tape were converted to digital format through a 24-point-per-cycle direct conversion. The data were then analyzed in order to determine the amplitude and phase angle with respect to the input force of the fundamental harmonic. The amplitude of the fundamental harmonic, when plotted as a function of the transducer station number, was then used to define the model deflection shapes.

To obtain damping data, the force was removed from the model by suddenly cutting power to the shaker armature. The amplitude decay of a selected transducer was recorded as an oscillogram. The amplitudes of several cycles of the decaying signal were plotted and the slope of a straight line faired through these points was used to compute the damping value. To insure realistic data, at least 10 cycles of the decaying signal were used for each damping value.

Test Procedure

The experimental data were obtained in basically the same manner for all test conditions. The input force generator was programed to supply a constant-amplitude, sinusoidal force to the model at slowly increasing frequency. Selected output signals from the various transducers were automatically plotted as diagrams of total amplitude as a function of frequency. Selected signals were simultaneously monitored as Lissajous patterns on an oscilloscope and peak frequencies and phase shifts were noted. Individual peak response frequencies were then examined by manually tuning the frequency of excitation to obtain peak response and recording the output of all transducers for subsequent harmonic analysis. The input force was then suddenly removed and the decaying signals were recorded as oscillograms from which the previously discussed damping values were measured.

ANALYSIS

The mathematical representation of the 1/10-scale Saturn V model consists of masses m_i concentrated at discrete points along the vehicle's length connected by massless linear springs k_n. Figure 15 shows this representation and table II gives the mass and spring values. This procedure has been used in other analyses, for example,

those of references 10 and 11. The procedure is based upon the assumption that the motion of a system with an infinite number of degrees of freedom can be approximated by analyzing an appropriate spring-mass system which has a finite number of degrees of freedom. The relationship between spring-mass and continuous systems is discussed in reference 12. The selection of the number of masses to be used in a particular analysis is somewhat arbitrary as is the manner in some cases in which these masses are interconnected by the springs. The approach used herein is to select an arrangement which results in a single type of geometry to analyze to obtain stiffness representations between two mass locations. This method locates mass concentration points where changes in shell geometry occur or where branch masses join the main structure. An alternate approach is to select displacements at closely spaced vehicle stations as generalized coordinates, assume a displacement distribution between succeeding coordinate locations, and derive stiffness and mass matrices from the potential and kinetic energies which are calculated by using the assumed displacement functions. A notable feature of this method is that the mass matrix is not, in general, diagonal. This procedure is discussed in reference 13.

Some of the results of the present analysis have been presented in reference 14; however, the results presented herein reflect improvements in the lumped parameter analysis of reference 14. In the present mathematical representation of the 1/10-scale Saturn V model, an improved set of orthotropic spring constants were derived for the S-IC intertank section, the model LM representation was extended to include two degrees of freedom, and the elastic properties of the IU/S-IVB forward skirt joint were empirically revised based upon static load-deflection tests of the model. These static tests and isolated LM tests are discussed in appendix A.

The natural frequencies and mode shapes of the Apollo/Saturn V model were found by generating and solving the standard eigenvalue problem

$$\left[K - M\omega^2\right]\{y\} = \{0\} \tag{1}$$

by a method of the Givens type (see ref. 15) where $[K]$ is the stiffness matrix, $[M]$ is the mass matrix, ω is the natural circular frequency, and $\{y\}$ is the mode shape.

Three weight conditions were considered: (1) 100 percent with the liquid oxygen and fuel tanks of the S-IC stage filled to simulate the lift-off weight condition, (2) 50 percent, corresponding roughly to the state at maximum dynamic pressure, and (3) empty, corresponding approximately to S-IC burnout.

Mass Distribution

The concentrated masses were found, in general, by locating one-half the structural mass between the end points of a shell at each of the end-point stations. A shell is taken here to mean a segment of the main structure which is essentially comprised of a single type of geometry, such as an intertank section or an interstage adapter. If one of the end-point stations was the junction point of a tank bulkhead and tank wall, the entire mass of the bulkhead was concentrated at the junction station. Engines in the upper stages were considered as separate concentrated masses. The outer engines in the first stage, however, were grouped with the support cradle and one-half the aft skirt mass. This arrangement was used because the attachment of these engines to the main structure is virtually rigid. The simulated lunar module (LM) was considered to be a two-degree-of-freedom branch system. Each liquid element in the vehicle was represented by a single lumped mass. The plastic beads, used to simulate the liquid hydrogen in the S-II and S-IVB stages, were treated in the same manner as the water which was used to simulate the liquid oxygen in all the stages and the fuel in the S-IC stage.

Because the liquid motion is potentially more complex than that of any other component of the vehicle, care must be exercised in its representation. A representation which has been used is that which is proposed by Wood in reference 16 and which is applied, with slight modifications, in references 10 and 11. The liquid is represented as a mass supported with certain springs and the coordinate used to describe the motion is the deflection of the liquid center of mass. The magnitude of the concentrated mass is equal to the total liquid mass. This representation was used for the liquid masses given in table II. A discrepancy between the analysis and experiment, which is discussed in the section "Results and Discussion," however, led to further consideration of this representation of the liquid.

The following analysis shows that the actual liquid mass is not necessarily appropriate for use with the center-of-mass deflection when this deflection is selected to be the generalized coordinate which characterizes the liquid motion. The kinetic energy of the liquid is written in terms of assumed motions. The magnitudes of these motions are determined by the deflection of the liquid center of mass. This deflection is therefore used as a generalized coordinate. The equivalent mass associated with this generalized coordinate is derived from the kinetic energy; thus, a mass consistent with the Rayleigh-Ritz procedure results. The analysis thus indicates approximately the deviation of the equivalent mass from the actual mass when the center-of-mass deflection is chosen as the generalized coordinate.

Consider the greatly simplified propellant tank of figure 16. It is assumed that the bending stiffness of the cylindrical shell which contains the liquid is negligible. With

this assumption, the radial displacement of the shell under static conditions is

$$w = \frac{\gamma a^2}{Et} x \tag{2}$$

where γ is the unit weight of the liquid, E is Young's modulus, t is the shell thickness, and a and x are defined in figure 16.

If it is assumed that a disk-shaped element of the liquid remains disk-shaped after the tank deformation, the longitudinal displacement of the liquid, denoted by $\tilde{u}$, is given by

$$\tilde{u} = 2 \int_x^h \frac{w}{a} d\xi \tag{3}$$

where ξ is a dummy variable of integration. Expressing w in terms of u_1, the movement of the center of mass of the liquid, gives

$$\tilde{u} = \frac{3}{2h^2} u_1 \left(h^2 - x^2\right) \tag{4}$$

It is assumed that the radial displacement of the liquid, denoted by $\tilde{w}$, varies linearly from zero at the center of the tank to a value equal to the shell displacement at the tank wall. The radial displacement of the liquid is then given in terms of u_1 by

$$\tilde{w} = \frac{3rx}{2h^2} u_1 \tag{5}$$

The kinetic energy of the liquid can be expressed in terms of u_1 which is now regarded as a generalized coordinate. The expression for the kinetic energy T is

$$T = \pi \int_0^h \int_0^a \rho r \left(\dot{\tilde{u}}^2 + \dot{\tilde{w}}^2\right) dr\, dx \tag{6}$$

The equivalent mass m_e is found by differentiating the kinetic energy twice with respect to the time derivative of the generalized coordinate u_1:

$$m_e = \frac{\partial^2 T}{\partial \dot{u}_1^2} \tag{7}$$

From this procedure it is found that

$$m_e = m_f \left[1.2 + 0.375\left(\frac{a}{h}\right)^2\right] \tag{8}$$

where m_f is the actual mass of liquid.

Equation (8) shows that if the shell responds to axisymmetric dynamic loading with the same characteristic shape as in the case of hydrostatic loading and if the liquid motion is that which is assumed, the actual mass of the liquid should be increased by more than 20 percent to obtain the equivalent mass.

It should be pointed out that the factor derived here was obtained through the use of a greatly simplified model of a propellant tank. The derivation did not account for the presence of bulkheads and the distribution of the radial and longitudinal displacements of the liquid was obtained by assumption. The adequacy of these assumptions is discussed in the section "Propellant Tanks."

Stiffness Representation

The calculations made to obtain the spring constants fell into three categories: (1) calculations for shell components having a conical shape, of which the cylinder is a special case, (2) calculations for springs to represent the stiffnesses in the liquid-tank interactions, and (3) calculations for branch systems such as the lunar module and engines in the S-II and S-IVB stages.

In order to include as accurately as practicable for a lumped-parameter analysis the effect of stiffening elements such as stringers and ring frames, the spring constants were derived by using equivalent orthotropic properties of the shells which comprise the total model. The major effects can be included relatively simply if the theory used is restricted to an axisymmetric membrane theory for orthotropic shells. This theory, when isotropic elastic constants are used and the shell is a cylinder, produces the conventional spring constant of AE/l. As a consequence of the neglect of bending stresses, all eccentricity effects are also ignored. Reference 17 is devoted exclusively to anisotropic shell theory and it includes the orthotropic membrane theory used herein.

Conical shell.- A typical conical shell and its associated coordinate system are shown in figure 17. The coordinate in the meridional direction is s and the coordinate in the circumferential direction (not shown) is θ.

The spring constant for the conical shell is defined as

$$K = \frac{F}{\delta} \tag{9}$$

where F is the force and δ is the distance in the x-direction through which it acts, if it is assumed that the base is not allowed to move longitudinally.

The relation between the stress resultants and the strains for a membrane shell of revolution loaded axisymmetrically is, in matrix form,

$$\begin{Bmatrix} N_s \\ N_\theta \end{Bmatrix} = \begin{bmatrix} C_{11} & C_{12} \\ C_{12} & C_{22} \end{bmatrix} \begin{Bmatrix} \epsilon_s \\ \epsilon_\theta \end{Bmatrix} \tag{10}$$

where N_s is the stress resultant in the meridional direction, N_θ is the stress resultant in the circumferential direction, ϵ_s and ϵ_θ are the corresponding strains, and the matrix $[C_{ij}]$ is a proportionality matrix which reflectes the orthotropic elastic properties of the shell.

For the force F, the stress resultants are found from equilibrium to be

$$N_s = -\frac{F}{2\pi(R_o - l \cot \varphi_o + s \cos \varphi_o)\sin \varphi_o} \tag{11}$$

$$N_\theta = 0 \tag{12}$$

The strains are, from reference 18,

$$\epsilon_s = \frac{\partial u}{\partial s} \tag{13}$$

$$\epsilon_\theta = \frac{u \cos \varphi_o + w \sin \varphi_o}{R_o - l \cot \varphi_o + s \cos \varphi_o} \tag{14}$$

where u is the displacement in the meridional direction and w is the displacement normal to the shell.

When equation (10) is inverted and the previously determined relations for the stress resultants in terms of the load (eqs. (11) and (12)), and the strain displacement relations (eqs. (13) and (14)), are substituted, two simultaneous equations result which may be used to determine displacements in terms of the load. These equations are:

$$\frac{\partial u}{\partial s} = -\frac{F}{2\pi C_{11}\left(1 - \frac{C_{12}}{C_{11}}\frac{C_{12}}{C_{22}}\right)(R_o - l \cot \varphi_o + s \cos \varphi_o)\sin \varphi_o} \tag{15}$$

$$w = -u \cot \varphi_o + \frac{C_{12}F}{2\pi C_{11}C_{22}\left(1 - \frac{C_{12}}{C_{11}}\frac{C_{12}}{C_{22}}\right)\sin^2 \varphi_o} \tag{16}$$

When equations (15) and (16) are solved simultaneously and the relation

$$\delta = u(0)\sin \varphi_o - w(0)\cos \varphi_o \tag{17}$$

is applied, the displacement is given by

$$\delta = \frac{F}{2\pi C_{11}C_{22}\left(1 - \frac{C_{12}}{C_{11}}\frac{C_{12}}{C_{22}}\right)\sin^2\varphi_o \cos \varphi_o}\left(C_{22} \log_e \frac{R_o}{R_o - l \cot \varphi_o} - C_{12}\cos^2\varphi_o\right) \tag{18}$$

and therefore, from equation (9), the equivalent spring for a conical shell is given by

$$K = 2\pi C_{11}\left(1 - \frac{C_{12}}{C_{11}}\frac{C_{12}}{C_{22}}\right)\frac{\sin^2\varphi_o \cos \varphi_o}{\log_e\left(\frac{R_o}{R_o - l \cot \varphi_o}\right) - \frac{C_{12}}{C_{22}}\cos^2\varphi_o} \tag{19}$$

The equation for the equivalent spring constant for the cylinder can be obtained as a special case of the cone by allowing φ_o to approach the value $\pi/2$. When this is done, equation (19) becomes, in the limit,

$$K_c = \frac{2\pi a}{l} C_{11}\left(1 - \frac{C_{12}}{C_{11}}\frac{C_{12}}{C_{22}}\right) \tag{20}$$

The quantity K_c, which represents the equivalent spring constant for an orthotropic membrane cylinder, depends primarily upon C_{11} and to a much lesser extent on C_{22} and C_{12}. This dependence suggests that shells which do not contain liquids, such as intertank and interstage sections, are probably adequately represented by springs determined by the value AE/l where A represents the total cross-sectional area of the shell. Although this approach would yield some savings in time, some degradation in accuracy could result.

An illustrative example of the calculation of an equivalent spring for a conical shell is given in appendix B along with the calculation for one of the engine springs. The purpose of this appendix is to show the general degree of detail employed in the analysis of the Apollo/Saturn V model.

Propellant tanks.- A typical propellant tank is shown in figure 18. It is assumed that the behavior of the cylindrical portion of this tank can be described by equation (10); that is, the membrane theory for orthotropic shells is valid. The ellipsoidal bulkhead shown, of which the sphere is a special case, is assumed to be isotropic and to have a constant thickness. The height of liquid in the tank is assumed to be greater than the

length of the cylinder; that is, the liquid is standing within the upper bulkhead as shown in the figure.

It is further assumed that for practical tanks, the contribution of the upper bulkhead deformation to the total center-of-mass motion is small relative to that of the cylinder and lower bulkhead. In the analysis which follows, the upper bulkhead deformation is therefore neglected.

It is arbitrarily assumed that a structural mass is to be located at the junction of the upper bulkhead and the cylinder and that motion of the liquid is characterized by the movement of the center of mass of the liquid, that is, the liquid is represented as a mass supported in some manner by springs. The base of the cylinder is assumed to be fixed against longitudinal movement. Consistent with these assumptions, the two coordinates describing the tank motion are taken to be u_o and u_1, as indicated in figure 18.

The system is assumed to be linear. Therefore, the deformation is proportional to the load. If the loads P and W are applied as shown in the figure, the relationship between the load and the deformation can be written in matrix form as

$$\begin{Bmatrix} u_o \\ u_1 \end{Bmatrix} = \begin{bmatrix} \alpha_{11} & \alpha_{12} \\ \alpha_{21} & \alpha_{22} \end{bmatrix} \begin{Bmatrix} P \\ W \end{Bmatrix} \tag{21}$$

The matrix $[\alpha]$ is the flexibility matrix of the system. The inversion of this matrix yields the stiffness matrix for the propellant-tank system. It is more convenient to proceed with the loads P and W regarded as known quantities and obtain the flexibility matrix than to assume that the displacements are known and obtain the stiffness matrix directly.

By assuming a hydrostatic pressure variation for the liquid and neglecting any tank pressurization as a static load whose effect may be added subsequently to obtain the total stress, the equilibrium equations for the cylinder are:

$$N_s = \frac{P}{2\pi a} \tag{22}$$

$$N_\theta = \frac{3W}{\pi a^2 \Gamma} x \tag{23}$$

where $\Gamma = 3q + 2n - \left(m^3/n_1^2\right)$ and, referring to figure 20, $q = \frac{h}{a}$, $n = \frac{b}{a}$, $m = \frac{c}{a}$, and $n_1 = \frac{b_1}{a}$.

Substituting equations (22) and (23) for the stress resultants, along with equations (13) and (14) for the strains into equation (10), the stress-strain law, letting $\varphi_o = \frac{\pi}{2}$, and inverting yields

$$\begin{Bmatrix} \frac{\partial u}{\partial x} \\ \frac{w}{a} \end{Bmatrix} = \begin{bmatrix} C_{11} & C_{12} \\ C_{12} & C_{22} \end{bmatrix} \begin{Bmatrix} -\frac{P}{2\pi a} \\ \frac{3W}{\pi a \Gamma} x \end{Bmatrix} \tag{24}$$

Integration of the first of equations (24) and application of the boundary condition $u(h) = 0$ yield the displacements in terms of the applied loads.

$$u = \frac{1}{C_{11}C_{22}\left(1 - \frac{C_{12}}{C_{11}}\frac{C_{12}}{C_{22}}\right)}\left[\frac{C_{22}P}{2\pi a}(h - x) + \frac{3C_{12}W}{2\pi q \Gamma}(h^2 - x^2)\right] \tag{25}$$

$$w = \frac{1}{C_{11}C_{22}\left(1 - \frac{C_{12}}{C_{11}}\frac{C_{12}}{C_{22}}\right)}\left(\frac{C_{12}P}{2\pi} + \frac{3C_{11}W}{\pi a \Gamma} x\right) \tag{26}$$

When the radial displacements of the cylinder and bulkhead are known, it is possible to calculate the longitudinal displacement of the center of mass of the liquid. This displacement is given, as shown in reference 18, as

$$u_1 = \frac{\Delta M}{V} \tag{27}$$

where ΔM is the first moment of the total volume change of the tank about an axis located in the surface of the liquid. This volume change is made up of two parts – the volume change which occurs because of the expansion of the cylinder wall and the volume change which occurs because of the expansion of the bulkhead. For small deflections the first moment of this volume is obtained by the relation

$$\Delta M = 2\pi a \int_c^h wx\, dx + \frac{\pi \gamma a^6}{2Et}\left[H(n,\nu) + 2qG(n,\nu) + q^2F(n,\nu)\right] \tag{28}$$

where γ is the unit weight of the liquid and $F(n,\nu)$, $G(n,\nu)$, and $H(n,\nu)$ are the functions obtained in reference 18 in connection with equivalent bulkhead stiffness.

If the integration of equation (28) is performed and the result is substituted into equation (27), equation (21) which contains the flexibility matrix may be written explicitly, by using the fact that $u_o = u(c)$, as

$$\begin{Bmatrix} u_o \\ u_1 \end{Bmatrix} = \frac{1}{2\pi C_{11}C_{22}\left(1 - \frac{C_{12}}{C_{11}}\frac{C_{12}}{C_{22}}\right)} \begin{bmatrix} C_{22}(q - m) & \frac{3C_{12}\left(q^2 - m^2\right)}{\Gamma} \\ \frac{3C_{12}\left(q^2 - m^2\right)}{\Gamma} & \frac{12C_{11}\left(q^3 - m^3\right)}{\Gamma^2} + \frac{2\pi C_{11}C_{22}\left(1 - \frac{C_{12}}{C_{11}}\frac{C_{12}}{C_{22}}\right)}{K_{BH}} \end{bmatrix} \begin{Bmatrix} P \\ W \end{Bmatrix} \tag{29}$$

where

$$K_{BH} = 2\pi Et \frac{\Gamma^2}{9\left[H(n,\nu) + 2qG(n,\nu) + q^2F(n,\nu)\right]} \tag{30}$$

The matrix relating the loads to the displacements in equation (29) is the flexibility matrix of the propellant-tank combination. When this matrix is inverted, the resulting stiffness matrix is seen to represent a system having three springs. The off-diagonal term represents a spring connecting the two masses while the difference between the off-diagonal and the diagonal terms represents a spring connecting a mass to the ground. Application of these facts leads to the conclusion that the set of springs represented by the stiffness matrix is that shown in figure 18. The value of each of these springs is

$$K_1 = K_c \frac{C_{22}}{C_{11}} \frac{1 - 3\frac{C_{12}}{C_{22}}\frac{\left(q^2 - m^2\right)}{p\Gamma}}{\Lambda} \tag{31}$$

$$K_2 = K_c \frac{C_{22}}{C_{11}} \frac{3\frac{C_{12}}{C_{22}}\frac{\left(q^2 - m^2\right)}{p\Gamma}}{\Lambda} \tag{32}$$

$$K_3 = K_c \frac{\frac{12\left(q^3 - m^3\right)}{p\Gamma^2} - 3\frac{C_{12}}{C_{11}}\frac{q^2 - m^2}{p\Gamma} + \frac{2\pi}{p}\frac{C_{22}}{K_{BH}}\left(1 - \frac{C_{12}}{C_{11}}\frac{C_{12}}{C_{22}}\right)}{\Lambda} \tag{33}$$

where

$$\Lambda = 12\,\frac{q^3 - m^3}{p\Gamma^2} - 9\,\frac{C_{12}}{C_{11}}\,\frac{C_{12}}{C_{22}}\,\frac{q^2 - m^2}{p^2\Gamma^2} + \frac{2\pi}{p}\,\frac{C_{22}}{K_{BH}}\left(1 - \frac{C_{12}}{C_{11}}\,\frac{C_{12}}{C_{22}}\right)$$

and K_c is given by equation (20).

If a similar analysis is performed with the assumption that the liquid does not stand within the upper bulkhead, the equations for K_1, K_2, and K_3 are the ones obtained by setting $m = 0$ in equations (31), (32), and (33). In this case $q \leqq p$.

Although the springs of equations (31) to (33) are interrelated through the various geometric parameters, the orthotropic constant to which each spring is most sensitive can be determined by an examination of each spring. The quantity K_c, as shown by equation (20), depends primarily upon C_{11}, the longitudinal membrane stiffness. Examination of equation (31), the expression for K_1, shows that there is a product of K_c with C_{22}/C_{11}. The C_{11} of K_c cancels the C_{11} in the denominator; thus, K_1 is shown to be most sensitive to the value of C_{22}, the circumferential membrane stiffness. Since K_1 is directly connected to the liquid mass, as shown in figure 18, it is of primary importance in determining the natural frequency of the liquid-tank system. This examination also shows that if an isotropic membrane theory is used in the liquid-tank problem and the circumferential and longitudinal stiffnesses are substantially different, significant response errors could result. Examination of equation (32), the expression for K_2, shows that this spring is most sensitive to the value of C_{12}, the constant which couples longitudinal stress resultants and strains to those in the circumferential direction. This quantity therefore produces an effect in orthotropic membrane shells which is equivalent to that of Poisson's ratio in isotropic membrane shells. A similar examination of equation (33), the expression for K_3, shows that its dependence is primarily upon C_{11}, the longitudinal membrane stiffness.

Various special cases can be obtained from equations (31), (32), and (33). The springs for the simplified tank of figure 18, which was analyzed in connection with the equivalent mass of the liquid, are obtained by setting $m = n = n_1 = 0$, $p = q$, and K_{BH} approaching ∞, and by assuming isotropy. The result is

$$K_1 = \frac{2\pi Et}{q}\,\frac{3(1 - \nu)}{4 - 3\nu^2} \tag{34}$$

$$K_2 = \frac{2\pi Et}{q}\,\frac{3\nu}{4 - 3\nu^2} \tag{35}$$

$$K_3 = \frac{2\pi Et}{q}\,\frac{4 - 3\nu}{4 - 3\nu^2} \tag{36}$$

If the structural mass is taken to be zero, the system reduces to a single-degree-of-freedom system with an equivalent spring

$$K_e = \frac{3\pi Et}{2q} \tag{37}$$

With this result the natural frequency of the system can be calculated by using the equivalent mass of equation (8) and the result can be compared with available data on this configuration. References 19 and 20 contain such data based upon more rigorous, but more complex, analyses. Figure 19 shows a comparison of the frequencies from each of these analyses for various tank height-radius ratios. The results show a maximum deviation of about 6 percent for the range of heights investigated, the greatest difference occurring for the most shallow tank. It is felt that these comparisons tend to justify as being reasonable the various assumptions made to obtain the greatly simplified analysis from which the equivalent mass of equation (8) was derived.

RESULTS AND DISCUSSION

Experimentally measured and analytically determined longitudinal, free-free vibratory characteristics of the 1/10-scale Apollo/Saturn V model are presented in figures 20 to 51 and in table III which lists both analytical and experimental resonant frequencies and experimental damping values, where obtainable, for various S-IC liquid loading conditions. A summary plot of the experimental resonant frequencies as a function of S-IC loading condition is presented as figure 20. The closed symbols of figure 20 represent data from table III whereas the open diamond symbols are values obtained from supplementary, intermediate tests conducted during the course of the program, but otherwise not documented in the present paper. The purposes of this figure are to give the reader a visual summary of the model behavior and to illustrate the coupling between the S-IC LOX mode and structural and branch mass resonances. The faired curves represent the authors' interpretation of the model behavior based upon nonrecorded intermediate tests and recorded intermediate test points such as those shown.

In general, the experimental data are presented in the same format for each propellant loading condition. Diagrams of acceleration as a function of frequency are shown wherein the magnitude of the total response of selected accelerometers is displayed as a function of the forcing frequency for a constant-magnitude sinusoidal-input force. The trace associated with a given transducer has its zero at or near the location of the transducer referenced to the schematic of the model as shown on the left-hand side of each of the diagrams. Plus and minus signs indicate, respectively, in-phase or out-of-phase response with respect to the input force. Although all traces on a given diagram are

plotted with approximately equal sensitivities, the sensitivities are not necessarily the same on different diagrams.

After the acceleration-frequency diagram, the experimental deflection patterns for constant-frequency excitation, and where applicable, the mode shapes calculated by utilizing the orthotropic analysis are shown. The liquid mass in these calculations was taken to be the actual mass of the contained liquid. After the data presentation, a discussion of analytical results using both isotropic and orthotropic membrane theory for stiffness and using the actual and equivalent mass concepts for the liquid is presented. Both the experimental and analytical results are normalized to unity at the forward end, or tip, of the model wherever possible; however, in some instances, low experimental tip amplitudes necessitated the selection of alternate normalization points. The normalized amplitudes are plotted as a function of the nondimensional longitudinal coordinate x/L, where x is the model coordinate and L is the total length of the model. On each plot, the experimental resonant frequency, the appropriate analytical natural frequency, and the measured free-decay damping value are tabulated.

Lift-Off Configuration

Data from the lift-off configuration (100-percent S-IC propellant loading) are shown in figures 21 to 30. Figures 21 and 22 show two acceleration-frequency diagrams for this particular configuration. The trace-deflection sensitivities are the same for the two plots; however, the data of figure 21 were obtained with a 6-pound (27 N) nominal force input and the data of figure 22 were obtained with a nominal 12-pound (53 N) input force. The data show that doubling the input force approximately doubled the response amplitude and thus indicated that the structure is nearly linear for this range of input force. The acceleration-frequency diagrams also reveal that the response of the model is divided into two distinct frequency domains. At lower frequencies ($f_e < 80$), the structure above the S-II stage is very active whereas the remainder of the model is relatively quiescent. Conversely, in the higher frequency domain ($f_e > 80$), the S-IC and S-II structures respond to the input force whereas the S-IVB and payload structures experience minimal accelerations. This divided response trend was observed for all simulated flight times.

The behavior of the trace associated with the thrust structure can best be explained by considering the relative locations of the input force and the accelerometer. The accelerometer was located on the top of the thrust structure cross beam and immediately above the shaker attachment point. If the cross beam is considered to be a system with a high stiffness-mass ratio, the accelerometer senses the reaction of a force applied to a mass through a spring. The lowest, experimentally determined, resonant frequency of the thrust structure cross beam is approximately 260 cps. Below this resonant frequency, the acceleration response is proportional to the square of the forcing frequency. When

this response is plotted as a function of the forcing frequency, as is done in the acceleration-frequency diagrams, a nearly parabolic curve results with superimposed peaks caused by system resonant responses.

Experimental resonant deflection shapes and calculated mode shapes for the lift-off configuration are shown in figures 26 to 30. All data are normalized to unity at the forward end or tip of the model with the exception of figure 30 wherein low tip amplitude necessitated normalization at the aft end or base of the model. The analytical curves shown are faired through discrete calculated deflections.

The experimental data in figure 26 show that the entire instrumented portion of the model structure is moving in phase with the input force. Maintenance of momentum balance in the system precludes the existence of such a condition for the total system since the excitation frequency (30.9 cps) is well above the rigid-body frequency (3.5 cps) of the model on its support cables. With no analytical data available, it would be reasonable to assume that momentum balance is achieved through out-of-phase motion of some large noninstrumented mass. The analysis verifies this assumption and shows the out-of-phase mass to be the liquid in the S-IC LOX tanks. Further experimental confirmation of the nature of this resonance may be found from examination of the strain and pressure data shown in figures 23 to 25. The locations of the transducers are given in figure 13. In figure 23, the pressure gage P-3 located in the LOX tank lower bulkhead shows a small pressure response peak and phase change at about 30 cps. Likewise, in figure 24 both horizontal and vertical strain peaks in the LOX tank lower bulkhead are shown by the response of gages 22-H and 22-V. The data, however, are insufficient to determine the magnitude of the LOX mass motion. The surface strain data in figure 25 show no detectable longitudinal strain patterns in the S-IC LOX tank at 30 cps. Further, the orientation of the surface gages was such that circumferential strains in the tank walls could not be measured. In spite of these limitations, it is felt that the experimental data along with the analytical results are sufficient to identify qualitatively the LOX mass resonance.

The response of strain gages S-14 and S-16 in figure 25 also served to identify the LOX suction duct tunnel resonance at about 97 cps whereas the output of the pressure gage P-5 shown in figure 24 served to identify the resonance of the simulated PVC on its lower bellows spring.

Rather poor correlation between the results of the analysis and those obtained experimentally is evident in both frequency (f_o = 38.0 cps; f_e = 30.9 cps) and in deflection shape. One potential reason for the poor frequency correlation is the previously discussed representation of the contained liquid. Effects of the application of the equivalent mass concept as derived in equation (8) are discussed in the section "Equivalent Mass and Orthotropic Stiffness Effects."

Both analysis and experiment in figure 27 exhibit the classical first bar-type longitudinal deflection shape. Frequency correlation for this mode is excellent (f_o = 40.3 cps; f_e = 40.2 cps) and the deflection shape correlation is reasonably good with the exception of the simulated LM for which the experimental value is low by about 25 percent. The analysis also shows that the S-IC LOX mass is still moving out of phase with the tank structure; thus, considerable liquid-tank interaction in this mode is indicated.

These facts illustrate the difficulties associated with the lumped-parameter model in treating the liquid-tank interaction. Also, they show the need for an improved model. A continuous analysis which was obtained by NASA contract and which is applied in reference 14 predicts the LOX mode satisfactorily. In this analysis, several assumed shapes are used in the liquid-tank areas yielding more than one degree of freedom. Thus, work to improve lumped-parameter representations should be along the lines of including more degrees of freedom for the liquid. This approach is also suggested by noting that the equivalent mass reflects variations in the tank shape and liquid behavior which may occur with changes in the excitation frequency of the system; thus, a single-degree-of-freedom representation of the liquid will be inadequate for more than one system mode.

The test results indicate an unusually abrupt change in the deflection shape in the IU-SLA joint (s/L = 0.76). This effect is present in the results for all the weight conditions. To assess the contribution of this joint to the model deformation, static tests were performed. The analysis was revised accordingly since the effect could not be derived from model drawings. These static tests are discussed in appendix A.

The resonance depicted in figure 29 is primarily due to motion of the simulated LM mass. A relatively high force level was required to produce the low amplitude shown. For example, the tip acceleration amplitude measured for the 11-pound (49 N) input in figure 28 was 0.071g whereas the tip acceleration amplitude for the 15-pound (67 N) force in figure 29 was only 0.013g. The character of the simulated LM response as determined by separately testing the simulated LM is discussed in appendix A.

The poor correlation between analytical and experimental deflection shapes in the S-IC tank areas in figure 29 may originate from several sources. One possible reason for the measured amplitudes may be harmonic excitation of the transducers on their mounting pads. By considering the tank wall as a rotational spring and the relatively massive transducer attached to the wall, cantilever resonances of the transducers on their mounting springs were found by plucking each transducer and monitoring the decay frequency. Resonances occur at approximately 200 cps for the S-IC transducers in the lift-off condition. All the surface transducers on the S-IC stage in the lift-off condition exhibited 200 cps responses with amplitudes approximately one-fourth that of the fundamental at 71.3 cps. This explanation is not entirely satisfactory, however, since the

surface strain data of figure 25 show some evidence of longitudinal strain in the S-IC fuel tank walls at about 70 cps and figures 23 and 24 give indications of strain and pressure responses in the S-IC LOX tank lower bulkhead. It must, therefore, be assumed that the experimental deflection shape in figure 29 is at least partially associated with tank response patterns. The analysis does not consider higher order axisymmetric tank modes or nonaxisymmetric modes. The instrumentation, also, does not yield sufficient data to describe the response properly.

The resonance shown in figure 30 was not predicted by the analysis; therefore, only experimental data are presented. In addition, there are no clear-cut indications as to the source or sources of the resonant amplitudes. Surface strain gages (fig. 25) indicate what appears to be a second LOX suction duct tunnel resonance and longitudinal strains in the S-IC fuel tank at 136 cps. Bulkhead strain gages (fig. 24) show both radial and circumferential strains in both the LOX and fuel tank lower bulkheads. S-IC pressure responses (fig. 23) show a large PVC pressure response at 136 cps as well as lesser pressure responses in both lower bulkheads. In addition, all S-IC engines and the S-II thrust structure exhibit large longitudinal response peaks at this frequency.

75-Percent-Full Condition

Experimental data from the 1/10-scale Apollo/Saturn V model with the S-IC stage loaded to 75 percent of its lift-off propellant weight are presented in figures 31 to 33. In this configuration, the lowest resonance encountered has the classical bar-type, first longitudinal deflection shape. The LOX mode is shifted upward in frequency and appears to couple with the second structural mode. The resonance of the simulated LM mass was barely detectable at this weight condition with nominal-input force levels.

50-Percent-Full Condition

Analytical and experimental data from the configuration in which the propellant loading in the S-IC stage is half that at lift-off are shown in figures 34 to 39. As in previous cases, the data consist of plots of experimental acceleration against frequency and plots of combined analytical and experimental resonant deflection shapes. The agreement between experimental and analytical data for the first two longitudinal resonances of this condition is generally good in both frequency and deflection shape.

It should be recognized that the experimental data presented in this paper do not necessarily represent a complete set of vehicle modes. Often the natural frequencies of a complex system are not separable by the techniques and instrumentation employed in this investigation since they can exist very close together. Such is probably the case in figure 37 wherein no experimental resonance which corresponds to the analytical resonance was found. The frequency associated with the mode presented in figure 38

corresponds roughly to the uncoupled frequency of the S-IC LOX mass on its supporting springs. However, as seen from the summary plot in figure 20, the experimental LOX mode is found in proximity to the LM resonance and is not separated experimentally from it. The coupled resonant deflection shape is presented as figure 38. This coupling effect as well as previously discussed bulkhead and nonaxisymmetric tank motions may account for the deflection shape disagreement in the region $0 \leqq x/L \leqq 0.4$. The experimental resonant deflection shape of figure 39 is shown in the same context as discussed for figure 30.

25-Percent-Full Condition

Experimental data from the 25-percent S-IC propellant loading condition are presented in figures 40 to 45. As was the case with the 75-percent data, no analytical data were calculated. The experimental data follow the trends of previously presented responses with the exception that there appears to be no simulated LM response in the vicinity of 70 cps. Neither the acceleration-frequency diagram nor the deflection shape plots show evidence of any LM response at the anticipated frequency.

Burnout Condition

Experimentally determined response characteristics of the 1/10-scale Saturn V model at the S-IC burnout condition are correlated with the analytically derived mode shapes and frequencies in figures 46 to 51. The lowest mode (fig. 47) agrees very well in both frequency and deflection shape with the experimental data. Evidence of the inseparability of proximate modes by conventional experimental techniques is shown in figures 48 and 49. Analytically, two natural modes were found at 70.8 cps and 74.7 cps. A single resonance at 69.6 cps was observed experimentally. Examination of the experimental deflection shape reveals both the LM resonance, which is predicted by the analysis as the dominant mass in motion at 70.8 cps, and significant motion in the region $0 \leqq x/L \leqq 0.5$, which is characteristic of the analytical mode shape at 74.7 cps. From these observations, it would appear that the experimental shape represents a coupling of the two analytically predicted mode shapes.

Frequency agreement between analysis and experiment for the third resonance (fig. 50) is only fair and there is some discrepancy in the magnitude of the deflection shape in the region $0 < x/L < 0.4$. The experimental resonant deflection shape at 135.1 cps is presented, previously noted comments for figure 30 being applicable.

Equivalent Mass and Orthotropic Stiffness Effects

The present paper characterizes as an improvement the reflection of the orthotropic properties of the structure in the calculation of system spring constants, and

equation (8) in the analysis indicates a potential improvement in representation of liquid-tank interactions by the inclusion of a liquid equivalent mass. In an effort to define qualitatively the effects of both orthotropy and liquid mass value on the natural frequencies and mode shapes of launch vehicle structures, natural frequencies and mode shapes of the 1/10-scale Apollo/Saturn V model were calculated for three S-IC propellant loading conditions (100-, 50-, and 0-percent full) using both isotropic and orthotropic spring constants and both the actual liquid mass and the liquid equivalent mass as defined in equation (8). For all modes except the lowest two modes in the lift-off weight condition, results from the orthotropic and isotropic analyses were nearly identical. Since these two modes exhibit the most pronounced liquid-tank interactions, it would appear that the orthotropy of the structure affects primarily modes of this type. This observation tends to support the rationale previously developed in the discussion of propellant tank stiffness.

Four calculated mode shapes and frequencies for the lowest, or LOX, mode of the 1/10-scale Apollo/Saturn V model are shown in figure 52. Figures 52(a) and 52(b) are results of the isotropic analysis using the actual liquid mass and equivalent liquid mass, respectively. Figures 52(c) and 52(d) are results of the orthotropic analysis with the two liquid mass representations. A comparison of the four figures with each other and with the experimental data in figure 26 shows that, as would be expected, the higher equivalent mass tends to lower the resonant frequency. The mode shapes associated with the equivalent mass are also distorted in the region $0 \leqq x/L \leqq 0.25$. In none of the cases is the mode shape correlation between analysis and experiment considered good; however, the orthotropic theory with actual liquid mass yields reasonably good agreement. From a frequency standpoint, all the calculated frequencies are high, ranging from 39.3 cps to 33.8 cps as compared with the experimental frequency of 30.9 cps. In both analyses, however, use of the equivalent mass yields much better frequency correlation, the orthotropic analysis yielding the closer value.

The calculated frequencies and mode shapes for the second mode, corresponding to the first structural mode of the model, are shown in figure 53. As in the previous figure, the plots shown result from application of the orthotropic and isotropic analyses with actual and equivalent liquid mass representations. In this mode, the variations in both mode shape and frequency are less pronounced than in the LOX mode. A comparison with the experimental data in figure 27, however, shows that the orthotropic analysis with actual liquid mass yields the better mode shape correlation and nearly identical frequency (f_e = 40.2 cps; f_o = 40.3 cps). The degree of liquid-tank interaction in this mode as compared with the LOX mode is small. Therefore, the sensitivity of both mode shape and frequency to orthotropy in the tank structure is reduced. In the higher structural modes for this weight condition and in all structural modes for the other weight conditions analyzed, the sensitivity to orthotropy becomes negligible.

CONCLUSIONS

A 1/10-scale replica model of the Apollo/Saturn V launch vehicle has been tested and analyzed to determine its free-free longitudinal vibration characteristics during first-stage burn. A lumped-parameter analysis was employed to assess the applicability of such an analysis to a complex Saturn V type of launch vehicle and to investigate the effects of tank orthotropy and the method of representing the mass of contained liquids on the calculated natural modes and frequencies of the system. In addition, an approximate theory which accounts for tank-wall orthotropy is presented for the calculation of springs associated with liquid-tank systems. Model test results are presented and utilized in performing comparative evaluation of the various analytical predictions. Salient results of the combined analytical and experimental program may be summarized as follows:

1. Launch vehicle structures in which relatively large liquid masses are contained in thin walled tanks exhibit three principal types of longitudinal resonant response; one in which the motions are primarily those of the liquid masses deforming the elastic tanks; one in which bar-type structural deformations are involved; and the third in which elastically mounted components respond. The model tests show that system modes involving significant coupling exist when the frequencies of the propellant modes occur near structural or branch mass frequencies.

2. By using model tests as the standard for comparison, the analysis in which the stiffness coefficients reflect orthotropic properties of the structure yielded significantly better results for the modes involving liquid-tank interactions than the isotropic analysis did. Comparison of the two analyses for the structural modes showed little difference in either the mode shapes or natural frequencies. These findings indicate that the liquid-tank responses are much more sensitive to orthotropy than the structural responses are. This result would also indicate that even for liquid-tank modes, isotropic representation of non-liquid-carrying shells would result in little degradation in accuracy of calculated modes or frequencies.

3. Calculations performed by using both orthotropic and isotropic analyses and with both actual and equivalent liquid mass values show that use of an equivalent liquid mass produces better frequency agreement with experiment for the liquid-tank modes whereas the analyses utilizing actual liquid mass values were more accurate in the prediction of structural mode shapes and frequencies. The data indicate that a single-degree-of-freedom representation of the liquid is inadequate.

4. A comparison of the tank-bulging-mode frequency as calculated by refined methods and that calculated by the approximate method developed in the paper showed almost identical results for a wide range of ratios of liquid depth to tank radius.

5. Static and dynamic tests showed an abrupt change in model longitudinal deflection shapes at a joint in which thin-gage materials were used. This change necessitated revision of the analytical stiffness for this area on the basis of static tests since this effect could not be derived from model drawings. It is concluded therefore that stiffnesses in areas containing joints constructed of thin-gage materials should be verified by experiment whenever possible.

Langley Research Center,
National Aeronautics and Space Administration,
Langley Station, Hampton, Va., January 21, 1969,
124-08-05-18-23.

APPENDIX A

SUPPLEMENTARY TESTS

Longitudinal Static Load-Deflection Measurement

Examination of the dynamic-response data indicated that the joint between the IU and the SLA ($x/L = 0.76$) was contributing substantially to the deformation of the model. An examination of the joint revealed that the mating surfaces were not planar and that visible gaps existed on the circumference between fasteners. These gaps are attributed to limitations in the technology of the fabrication of thin-gage metals since the flanges of the ring frames which mate to form this joint are each only 0.009 inch (2.29×10^{-4} meter) thick. In order to determine the magnitude of this joint effect, the model was statically loaded and longitudinal displacements were measured along the external surface. Results of one such load-deflection test are shown in figure 54. The figure shows experimental and calculated longitudinal deflections resulting from a 400-lb (1780-N) load applied along the model center line through a plate at the top of the simulated service module. Since there was no way to predict this joint effect from the model drawings, the spring k_8 of the analysis was empirically revised to obtain an equivalent stiffness between stations 310 inches (7.875 meters) and 326 inches (8.277 meters). The figure shows calculated deflection curves from both the original and revised analyses. The representation employing the revised value of k_8 is used in all the analytical results shown in this report.

Vibration Tests of Simulated LM

Longitudinal vibration tests of the 1/10-scale Apollo/Saturn V model revealed a major resonance which appeared to consist primarily of motion of the simulated LM. Calculated spring constants for the LM body on the attachment truss members yielded predicted responses of much higher frequency than those observed. Consequently, the simulated LM was removed from the model and tested to determine the nature of the observed resonance. A simple test setup was employed as shown pictorially in figure 55. Each support truss apex was rigidly attached to an aluminum post which was, in turn, bolted to deep web steel I-beams set in a concrete floor. A small shaker was attached at the center of the aft end of the model LM. Responses were measured at selected points on the model and support structures. Some typical results are shown in figure 56. Acceleration-frequency plots from six of the transducers are given. The data indicate a resonance of the model LM at 67.9 cps. Examination of the vibrating model showed large deflections at the model center line; smaller in-phase deflections near the edge of the model body; no transverse motions; and no response of the support structure. It was,

therefore, concluded that the resonance was that of the internal ballast masses deflecting with the elastic model end plates. A new analysis was performed in which the LM model was treated as a two-degree-of-freedom system. One mass represented the ballast weights and end plates and the other mass represented the cylinder and attachment trusses. This representation predicted a LM model resonance at 67.7 cps. Because of the good agreement between the calculated and experimental resonant frequencies, the two-degree-of-freedom representation was incorporated into the mathematical model of the system.

The LM model was also statically tested and the results verified the initially calculated spring constants for the attachment truss members.

APPENDIX B

TYPICAL STIFFNESS CALCULATIONS

Some typical calculations are presented to illustrate the methods used in obtaining the orthotropic elastic membrane constants for the shells of the Apollo/Saturn V model which were used in the calculation of spring constants and to show the general degree of complexity of the structural theory used to calculate the spring constants in the spring-mass model. Accordingly, the numerical calculations associated with the S-IC liquid oxygen tank and those for a branch mass, the S-II center engine, are presented.

S-IC Liquid Oxygen Tank

The S-IC liquid oxygen tank is comprised of an aluminum skin which has constant thickness in the circumferential direction and which tapers linearly in the longitudinal direction, integrally milled, longitudinal, tee-section stiffeners, and baffle assemblies which are welded to the flanges of the longitudinal stiffeners. All stiffening elements are also aluminum. Typical repeating elements are shown in figure 57.

It was assumed that only the skin and stringers are effective in resisting the longitudinal loads and that the skin is the only element which couples longitudinal load to circumferential deformation and circumferential load to longitudinal deformation. Since the skin of this tank varies in thickness from 0.019 inch (4.8×10^{-4} meter) at the forward end to 0.025 inch (6.3×10^{-4} meter) at the aft end, it was assumed that the average value of 0.022 inch (5.5×10^{-4} meter) could be used. Poisson's ratio is assumed to be 0.3. Young's modulus is taken to be 10^7 lb/in^2 (6.89×10^{10} N/m^2).

Since a portion of the baffle web is corrugated, it cannot be fully effective in resisting the circumferential loads. Consequently, in the calculations which follow, the effective area of the corrugated portion of the baffle web was taken to be 50 percent of the actual area. The actual area of this component constitutes about 10 percent of the total area of the baffle assembly and skin. Therefore, even if the 50-percent factor is in error by as much as 30 percent, the membrane constant would contain only a 3-percent error as a result of this assumption.

For the longitudinal direction in which the total number of stringers is 168 the calculation for C_{11} yields the following values:

Stringer flange area, $168 \times 0.13 \times 0.015$	0.32760 in^2	(211.3×10^{-4} m^2)
Stringer web area, $168 \times 0.163 \times 0.010$	0.27384 in^2	(176.6×10^{-4} m^2)
Total stringer area	0.60144 in^2	(387.9×10^{-4} m^2)
Circumference, $2\pi \times 19.8$	124.407 in.	(3.16 m)

APPENDIX B

Average area of stringers per inch of circumference, 0.00483 in^2 (3.1×10^{-4} m)

$$C_{11} = \frac{0.022 \times 10^7}{1 - (0.3)^2} + 0.00483 \times 10^7 = 2.901 \times 10^5 \text{ lb/in. } (5.080 \times 10^7 \text{ N/m})$$

For the circumferential direction in which the total number of baffle assemblies is 13 the calculation for C_{22} yields the following values:

Outer ring flange area, $13 \times 0.015 \times 0.15$	0.02925 in^2	(0.19×10^{-4} m^2)
Outer ring web area, $13 \times 0.145 \times 0.012$	0.02262 in^2	(0.15×10^{-4} m^2)
Baffle web area (corrugated), $13 \times 2.460 \times 0.004 \times 0.5$	0.06396 in^2	(0.41×10^{-4} m^2)
Baffle web area (noncorrugated), $13 \times 0.305 \times 0.004$	0.01586 in^2	(0.10×10^{-4} m^2)
Inner ring flange area, $13 \times 0.203 \times 0.011$	0.02903 in^2	(0.19×10^{-4} m^2)
Inner ring web area, $13 \times 0.114 \times 0.011$	0.01630 in^2	(0.11×10^{-4} m^2)
Total circumferential stiffener area	0.17702 in^2	(1.14×10^{-4} m^2)

Shell length, 48.898 inches (1.24 meters)

Average circumferential stiffener area per inch of length, 0.00362 in^2 (0.02×10^{-4} m^2)

$$C_{22} = \frac{0.022 \times 10^7}{1 - (0.3)^2} + 0.00362 \times 10^7 = 2.780 \times 10^5 \text{ lb/in. } (4.869 \times 10^7 \text{ N/m})$$

The coupling coefficient is calculated by considering only the skin as a coupling element. This calculation yields:

$$C_{12} = \frac{0.3 \times 0.022 \times 10^7}{1 - (0.3)^2} = 0.7253 \times 10^5 \text{ lb/in. } (1.270 \times 10^7 \text{ N/m})$$

S-II Center Engine Support Spring

The S-II center engine is supported by a cross beam of I-configuration. For purposes of analysis, the cross beam was regarded as four identical beams, each of which is assumed to have zero slope at the vehicle center line and to be pinned at the juncture of the cross beam and thrust cone. The longitudinal spring constant for the S-II cross beam is taken to be four times the reciprocal of the relative end deflection when a unit shearing force is applied to one beam. Figure 58 shows the configuration of the beam and the area moment of inertia of the cross section as a function of the distance from the center line. Shear deformation is neglected. The beam is divided into sections Δx_i 1 inch (0.0254 m) long and the moment of inertia is assumed to be a constant equal to the average value in each of the sections.

APPENDIX B

The calculation of the spring constant for the cross beam follows:

Moment, M_i, $1(\ell - x_i)$		Distance to center line of section, x_i		Average moment of inertia, I_i	
lb-in.	N-m	inch	meter	$inch^4$	$meter^4$
8.67	0.22	8.67	0.22	0.0896	3.73×10^{-8}
7.67	.19	7.67	.19	.2238	9.31
6.67	.17	6.67	.17	.1681	6.99
5.67	.14	5.67	.14	.1325	5.51
4.67	.12	4.67	.12	.1035	4.31
3.67	.09	3.67	.09	.0790	3.29
2.67	.07	2.67	.07	.0585	2.43
1.67	.04	1.67	.04	.0403	1.68
.67	.02	.67	.02	.0424	1.76
.085	.002	.085	.002	.0215	.89

$$d = \sum_{i=1}^{10} \frac{M_i \, \Delta x_i x_i}{EI_i} = 2192 \times 10^{-7} \text{ in./lb } (12\,494 \times 10^{-10} \text{ m/N})$$

where d is the deflection due to a unit shear on one beam. The spring constant K for all four cross beams is

$$K = \frac{4}{2192 \times 10^{-7}} = 0.1824 \times 10^5 \text{ lb/in. } (0.3194 \times 10^7 \text{ N/m})$$

REFERENCES

1. Runyan, H. L.; Morgan, H. G.; and Mixson, J. S.: Use of Dynamic Models in Launch-Vehicle Development. AGARD Rept. 479, May 1964.

2. Mixson, John S.; Catherine, John J.; and Arman, Ali: Investigation of the Lateral Vibration Characteristics of a 1/5-Scale Model of Saturn SA-1. NASA TN D-1593, 1963.

3. Mixson, John S.; and Catherine, John J.: Comparison of Experimental Vibration Characteristics Obtained From a 1/5-Scale Model and From a Full-Scale Saturn SA-1. NASA TN D-2215, 1964.

4. Mixson, John S.; and Catherine, John J.: Experimental Lateral Vibration Characteristics of a 1/5-Scale Model of Saturn SA-1 With an Eight-Cable Suspension System. NASA TN D-2214, 1964.

5. Catherine, John J.: Torsional Vibration Characteristics of a 1/5-Scale Model of Saturn SA-1. NASA TN D-2745, 1965.

6. Thompson, William M., Jr.: An Investigation of the Response of a Scaled Model of a Liquid-Propellant Multistage Launch Vehicle to Longitudinal Excitation. NASA TN D-3975, 1967.

7. Jaszlics, Ivan J.; and Morosow, George: Dynamic Testing of a 20% Scale Model of the Titan III. AIAA Symposium on Structural Dynamics and Aeroelasticity, Aug.-Sept. 1965, pp. 477-485.

8. Leadbetter, Sumner A.; Leonard, H. Wayne; and Brock, E. John, Jr.: Design and Fabrication Considerations for a 1/10-Scale Replica Model of the Apollo/Saturn V. NASA TN D-4138, 1967.

9. Catherine, John J.: Experimental Vibration Characteristics of a 1/40-Scale Dynamic Model of the Saturn V—Launch-Umbilical-Tower Configuration. NASA TN D-4870, 1968.

10. Rose, R. G.: Dynamics of the Atlas 5-CPS Longitudinal Oscillation Following Launch As Related to the Tank Pressure Regulation System. Rep. GDA 63-0712 (Contracts AF 04(694)-196 and AF 04(694)-240), Gen. Dyn./Astronaut., Dec. 31, 1963. (Available from DDC as AD 435036.)
    Vol. I: Longitudinal Model Development.
    Vol. II: Pneumatic System Model Development.

11. Tai, C. L.; Loh, M. M. H.; and Kraft, L. E.: Evaluation Study of S-II Stage Longitudinal Oscillations (Pogo). Rep. No. SID 66-1455 (Contract NAS 7-200 MCR 607), N. Amer. Avia., Inc., Sept. 30, 1966.

12. Goldstein, Herbert: Classical Mechanics. Addison-Wesley Pub. Co., Inc., c.1950.

13. Archer, John S.: Consistent Matrix Formulations for Structural Analysis Using Finite-Element Techniques. AIAA J., vol. 3, no. 10, Oct. 1965, pp. 1910-1918.

14. Pinson, Larry D.; Leonard, H. Wayne; and Raney, John P.: Analyses of the Longitudinal Dynamics of Launch Vehicles With Application to a 1/10-Scale Saturn V Model. J. Spacecraft Rockets, vol. 5, no. 3, Mar. 1968, pp. 303-308.

15. Bodewig, E.: Matrix Calculus. Second rev. ed., Interscience Publ., Inc., 1959.

16. Wood, John D.: Survey on Missile Structural Dynamics. 7102-0041-NU-000, EM 11-11 (BSD-TN-61-42), Space Technol. Lab., Inc., June 1, 1961.

17. Ambartsumyan, S. A.: Theory of Anisotropic Shells. NASA TT F-118, 1964.

18. Pinson, Larry D.: Longitudinal Spring Constants for Liquid-Propellant Tanks With Ellipsoidal Ends. NASA TN D-2220, 1964.

19. Kana, Daniel D.; and Abramson, H. Norman: Longitudinal Vibration of Ring Stiffened Cylindrical Shells Containing Liquids. Tech. Rep. No. 7 (Contract No. NAS8-11045), Southwest Res. Inst., June 15, 1966.

20. Beal, T. R.; Coale, C. W.; and Nagano, M.: Influence of Shell Inertia and Bending Stiffness on the Axisymmetric Modes of a Partially-Filled Cylindrical Tank. AIAA Paper No. 65-412, July 1965.

TABLE I.- TEST WEIGHTS AND S-IC PROPELLANT LOADINGS

Nominal weight condition	S-IC LOX				S-IC fuel				Total model weight (a)	
	Weight		Liquid surface station		Weight		Liquid surface station			
	pounds	newtons	inches	meters	pounds	newtons	inches	meters	pounds	newtons
Burnout	4	18	78.3	1.99	12	54	24.5	0.62	1680	7 467
25 percent	784	3 488	99.5	2.53	284	1262	33.5	.85	2732	12 143
50 percent	1509	6 713	115.8	2.94	593	2638	40.5	1.03	3766	16 739
75 percent	2274	10 116	133.0	3.38	922	4102	47.9	1.22	4860	21 602
100 percent	2985	13 278	151.5	3.85	1282	5704	56.0	1.42	5931	26 362

[a]Does not include 15.25 pounds (67.8 N) support cradle or 36 pounds (160 N) of support cables.

TABLE II.- STIFFNESS AND MASS DATA FOR LUMPED-PARAMETER ANALYSIS

Branch mass name	Mass and spring constant numbers	Station		Mass		Spring constant	
		inches	meters	lb-sec^2/in.	kg	lb/in.	N/m
	1	420.0	10.688	0.011296	1.978	0.1414×10^6	0.2477×10^8
	2	384.0	9.754	.019906	3.486	1.0572	1.8514
	3	377.9	9.599	.072545	12.71	.0684	.1198
	4	359.6	9.130	.066717	11.68	.0755	.1322
	5	332.7	8.450	.003857	.6754	2.0850	.0226
LM	6	332.7	8.450	.017090	2.992	.0097	.01698
LM	7	332.7	8.450	.05132	8.987	.4120	.7215
	8	325.9	8.277	.010569	1.851	.1220	.2137
	9	310.1	7.875	.021213	3.715	.3802	.6658
	10	283.2	7.193	.024752	4.335	.0647	.1133
S-IVB engine	11	264.6	6.721	.008390	1.469	.0969	.1697
S-IVB LOX	12	283.2	7.193	.45336	79.40	.1876	.3285
S-IVB LH_2	13	301.5	6.758	.104904	18.37	.5198	.9103
	14	274.7	6.976	.02388	4.201	1.4485	2.5367
	15	251.9	6.398	.024788	4.341	.5487	.9609
	16	238.7	6.063	.058743	10.29	1.2956	2.2689
	17	184.8	4.694	.074142	12.98	.3455	.6051
	18	178.7	4.539	.092255	16.16	.0641	.1123
S-II outer engine	19	166.4	4.227	.033947	5.945	.1185	.2075
S-II center engine	20	166.4	4.227	.011089	1.942	.3916	.6858
S-II LOX	21	184.8	4.694	1.9933	349.1	5.0894	8.9129
S-II LH_2	22	211.8	5.379	.4059	71.08	1.2566	2.2006
	23	140.1	3.559	.136495	23.90	.0182	.0319
	24	91.2	2.317	.111689	19.56	.7002	1.2262
	25	60.2	1.529	.092247	16.16	[a].6162	1.0791
	26	36.5	.927	.178389	31.24	[a].1008	.1765
	27	11.2	.285	.40678	71.24	[a].2752	.4819
S-IC fuel	28	41.3	1.050	3.3294	[a]583.1	.8584	1.5033
S-IC LOX	29	115.7	2.938	7.6627	[a]1342.	1.2056	[a]2.1113
	30					.0778	[a]1.362
	31					[a].4902	[a].8585
	32					3.1748	5.5599

[a]The values shown apply to the 100-percent condition. In the 50-percent condition: $m_{28} = 1.6647$ (291.6); $m_{29} = 3.8313$ (671.0); $k_{25} = 0.6351 \times 10^6$ (1.1122×10^8); $k_{26} = 0.0604 \times 10^6$ (0.1058×10^8); $k_{27} = 0.6000 \times 10^6$ (1.0508×10^8); $k_{29} = 1.2622 \times 10^6$ (2.2105×10^8); $k_{30} = 0.0108 \times 10^6$ (0.0189×10^8); and $k_{31} = 0.5568 \times 10^6$ (0.9751×10^8). In the burnout condition: $m_{28} = m_{29} = 0$; $k_{25} = 0.6900 \times 10^6$ (1.2084×10^8); $k_{29} = 1.2727 \times 10^6$ (2.2288×10^8); and $k_{26} = k_{27} = k_{30} = k_{31} = 0$.

TABLE III.- SUMMARY OF LONGITUDINAL FREQUENCIES AND DAMPING OF 1/10-SCALE APOLLO/SATURN V MODEL

S-IC, percent full	Rigid body frequency, cps	Mode 1			Mode 2			Mode 3			Mode 4			Mode 5		
		f_e, cps	2ζ	f_o, cps	f_e, cps	2ζ	f_o, cps	f_e, cps	2ζ	f_o, cps	f_e, cps	2ζ	f_o, cps	f_e, cps	2ζ	f_o, cps
100	3.5	30.9	----	38.0	40.2	0.062	40.3	56.4	0.025	55.3	71.3	--	70.8	136.2	0.030	--
75	3.8	41.2	0.054	---	55.2	.036	---	---	-----	---	---	--	---	----	----	--
50	4.2	42.0	.068	43.1	57.1	.026	55.0 58.2	71.2	.016	70.8	---	--	---	136.2	----	--
25	4.8	45.8	.045	---	59.0	.030	---	86.6	-----	---	94.2	--	---	139.5	----	--
0	5.7	51.1	.023	53.3	69.6	.027	70.8 74.7	86.0	.048	78.0	---	--	---	135.1	.055	--

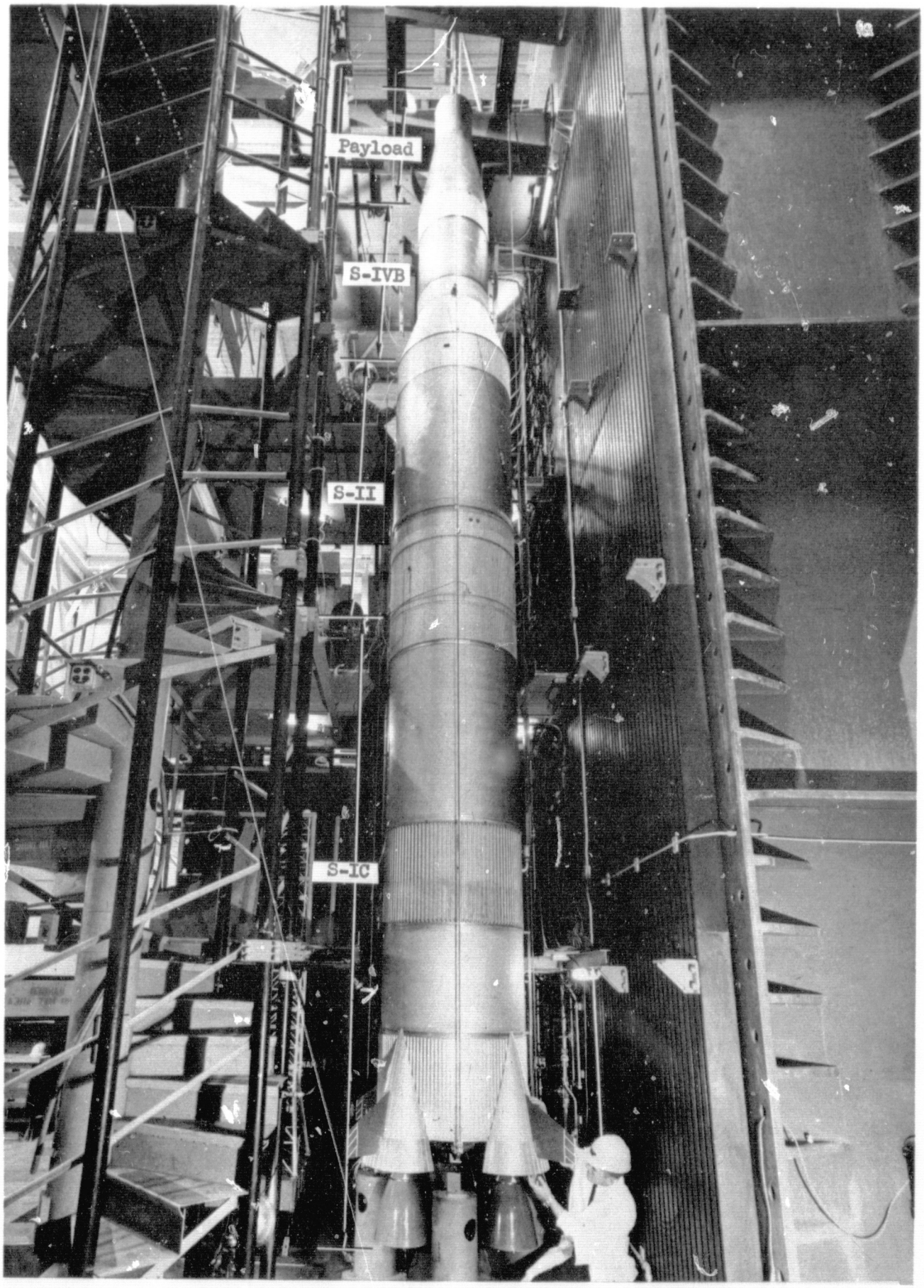

Figure 1.- 1/10-scale model of Apollo/Saturn V launch vehicle. L-69-1221

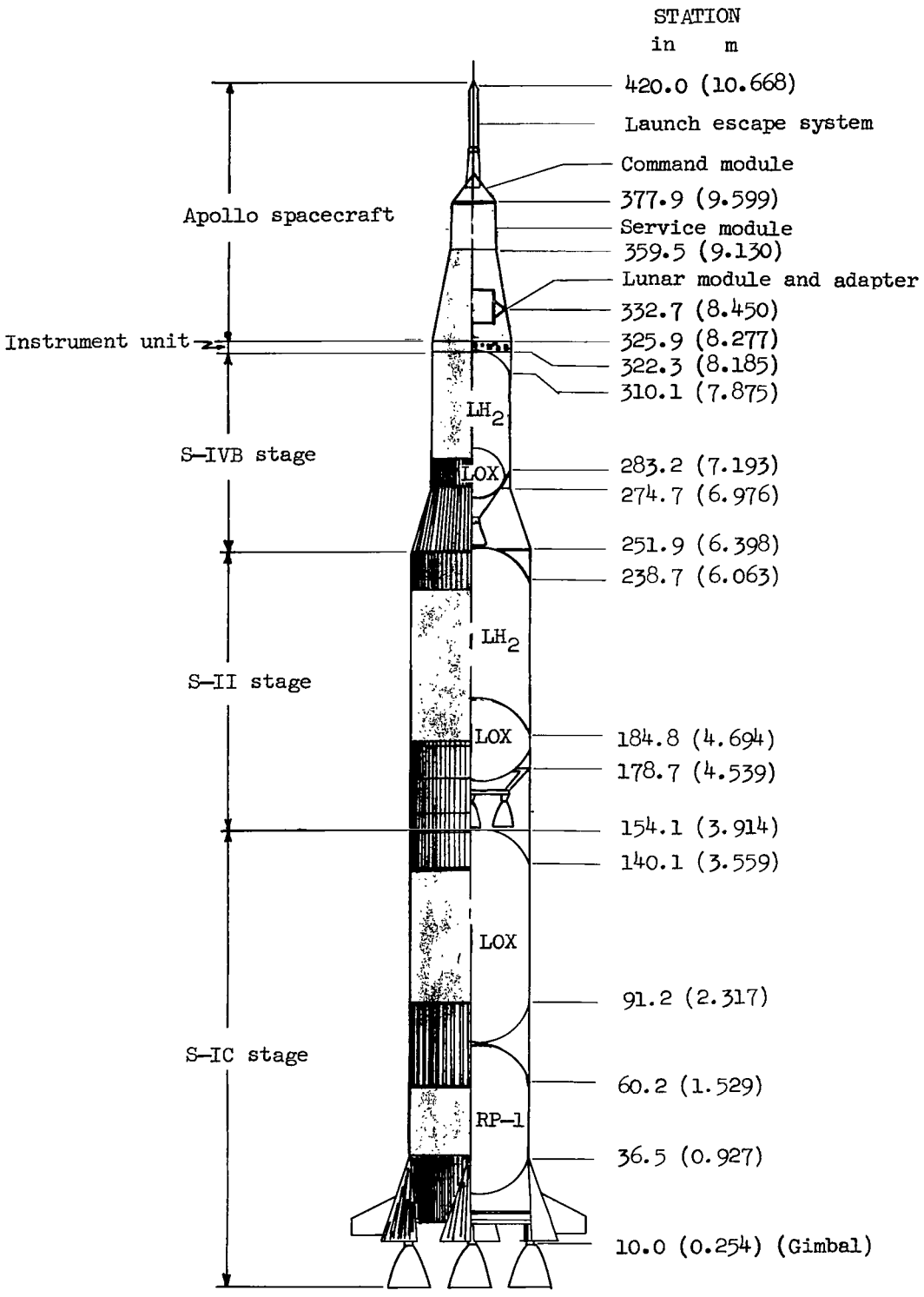

Figure 2.- Schematic of 1/10-scale Saturn V model.

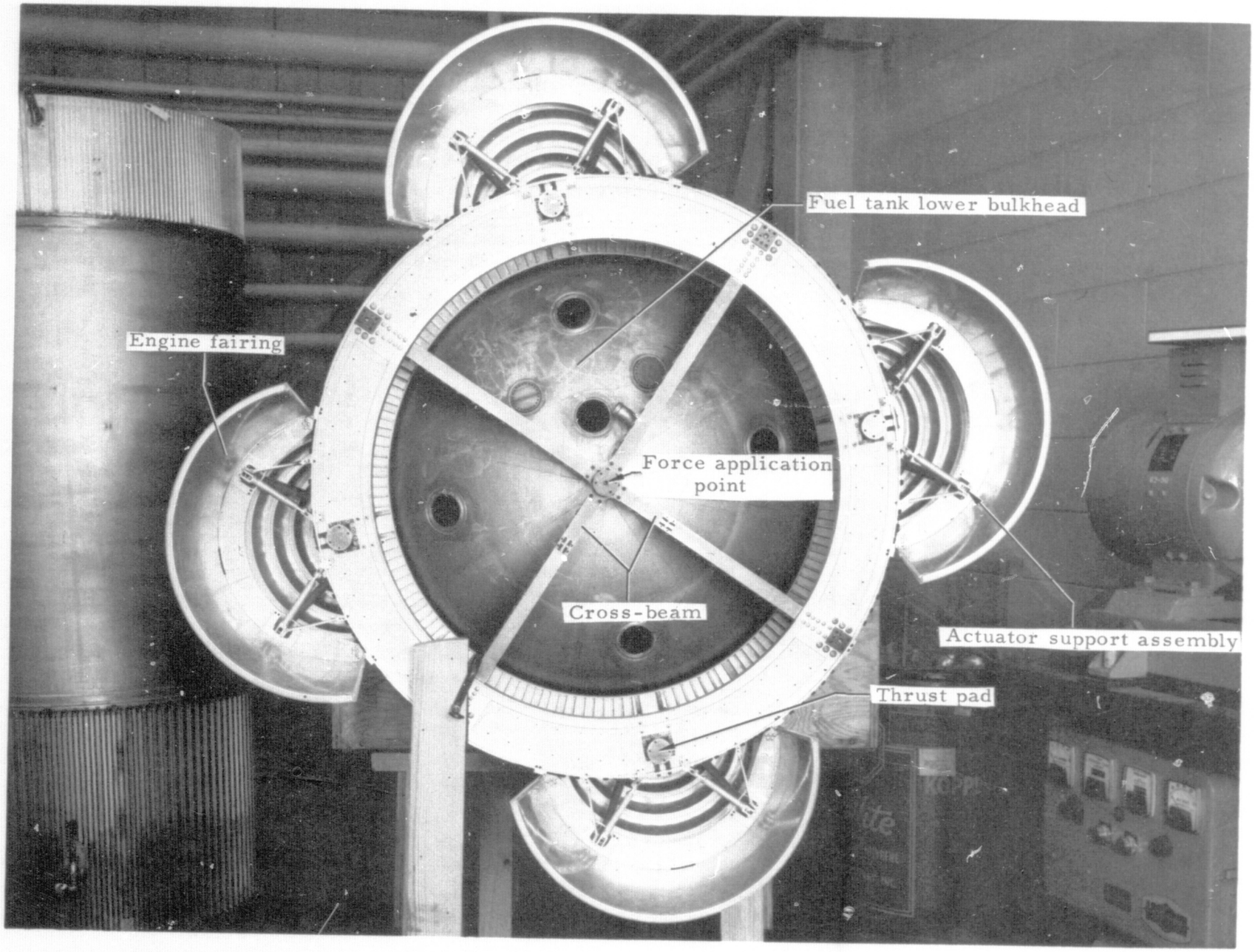

Figure 3.- 1/10-scale model. Aft view of S-IC stage.

L-64-9170.1

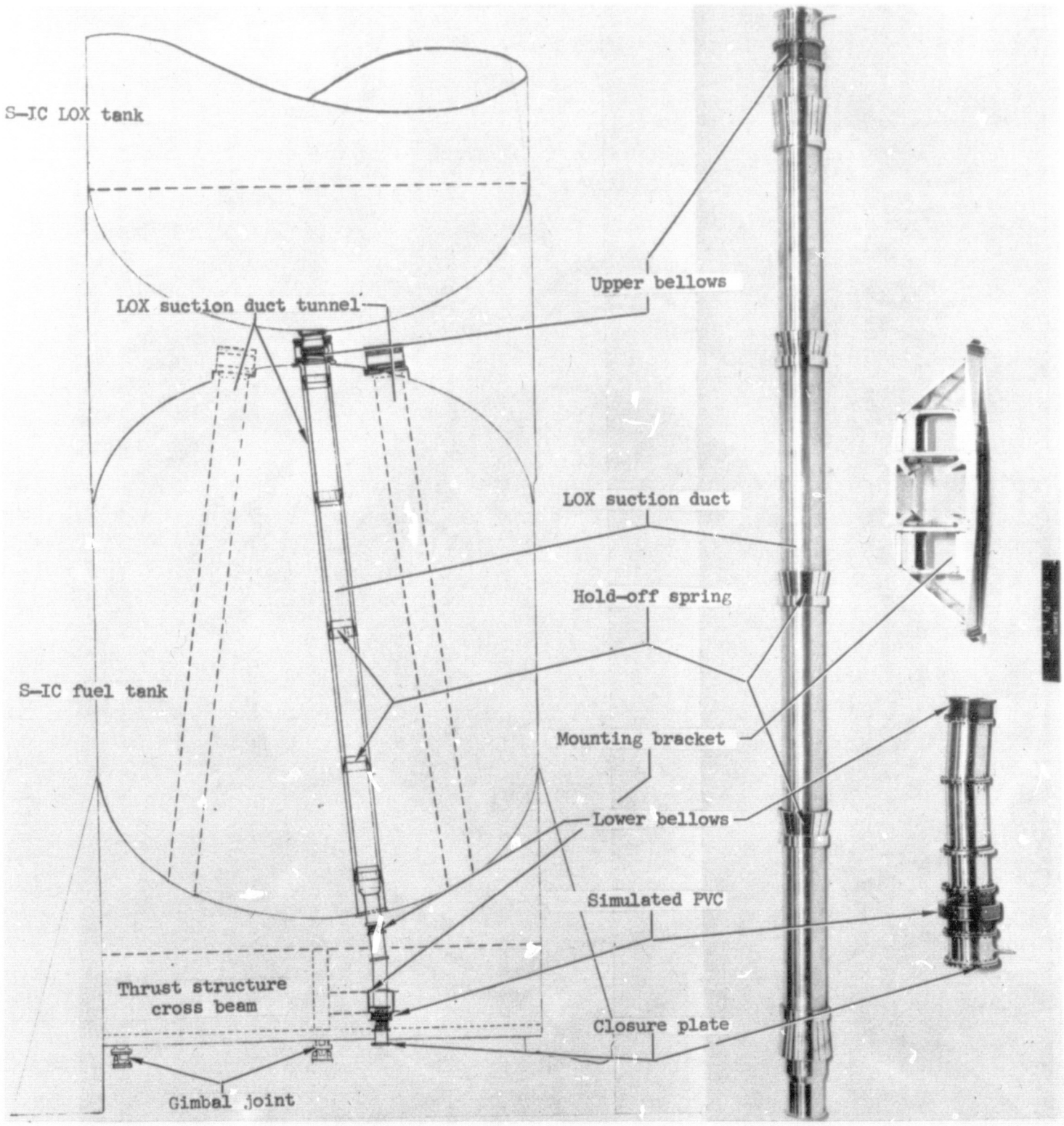

Figure 4.- 1/10-scale model. S-IC stage; simulated LOX suction duct; and sketch of installation. L-69-1222

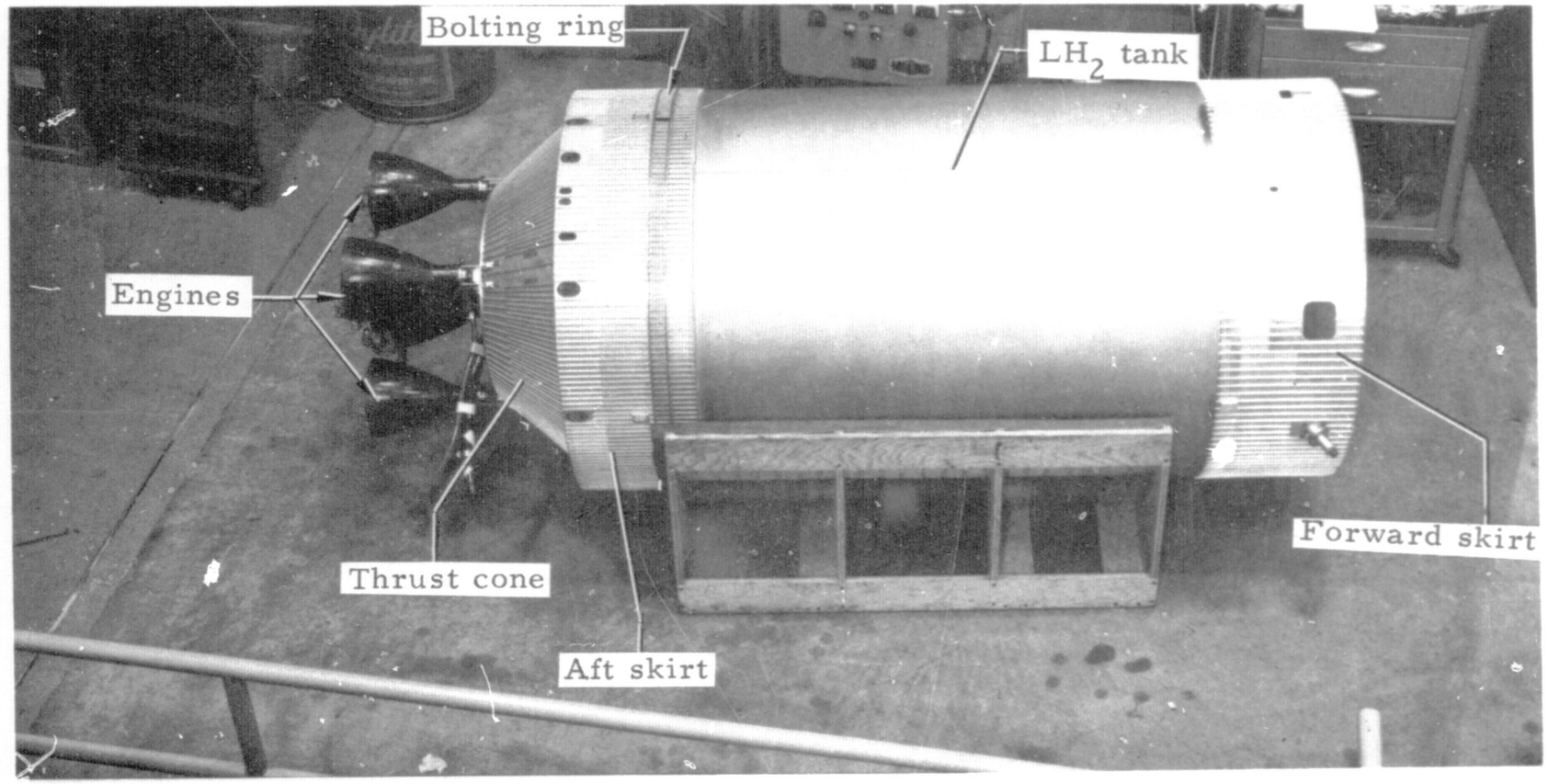

Figure 5.- 1/10-scale model. S-II stage fully assembled.

L-64-9368.1

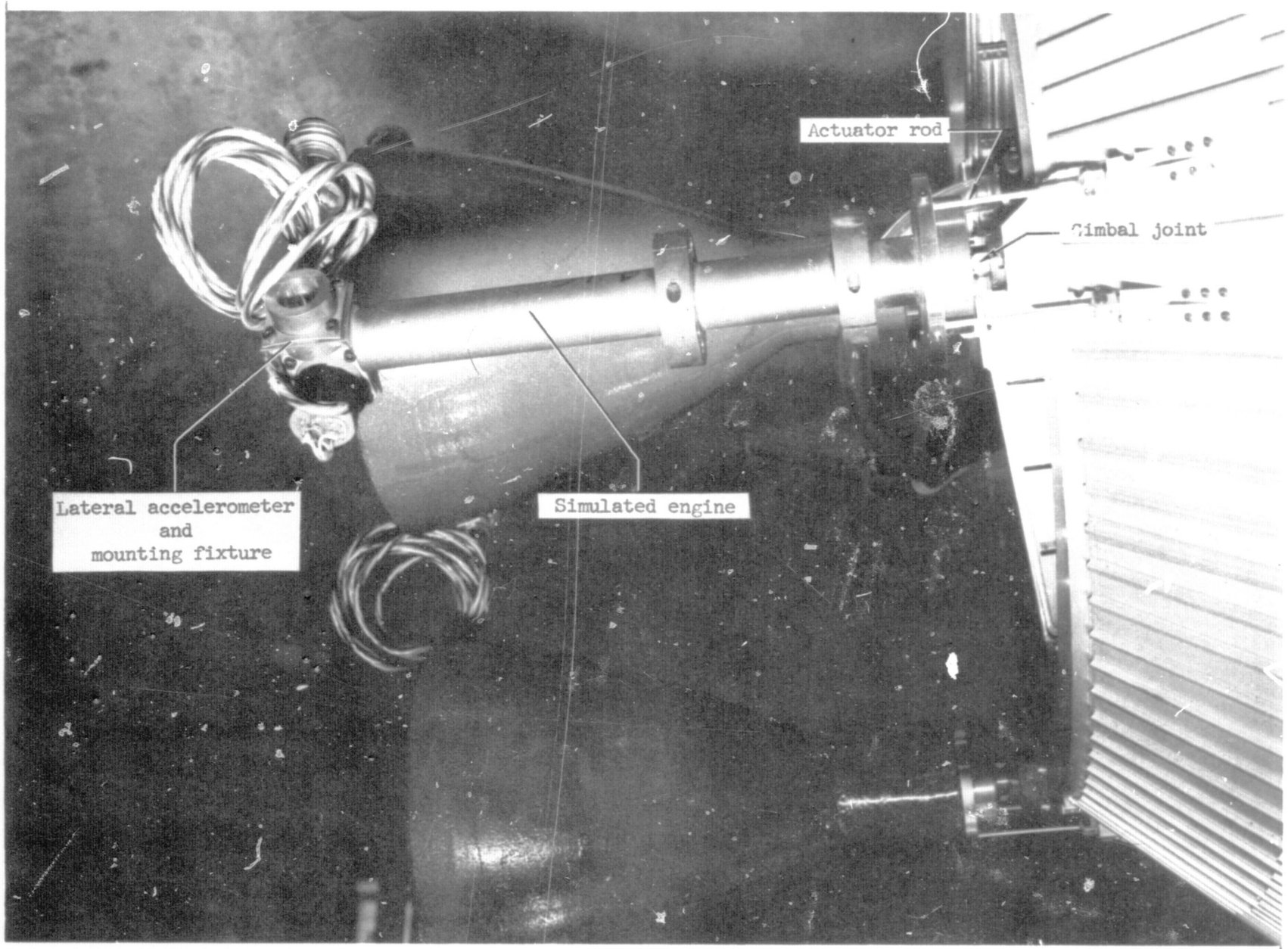

Figure 6.- 1/10-scale model. S-II simulated engines.

L-64-9366.1

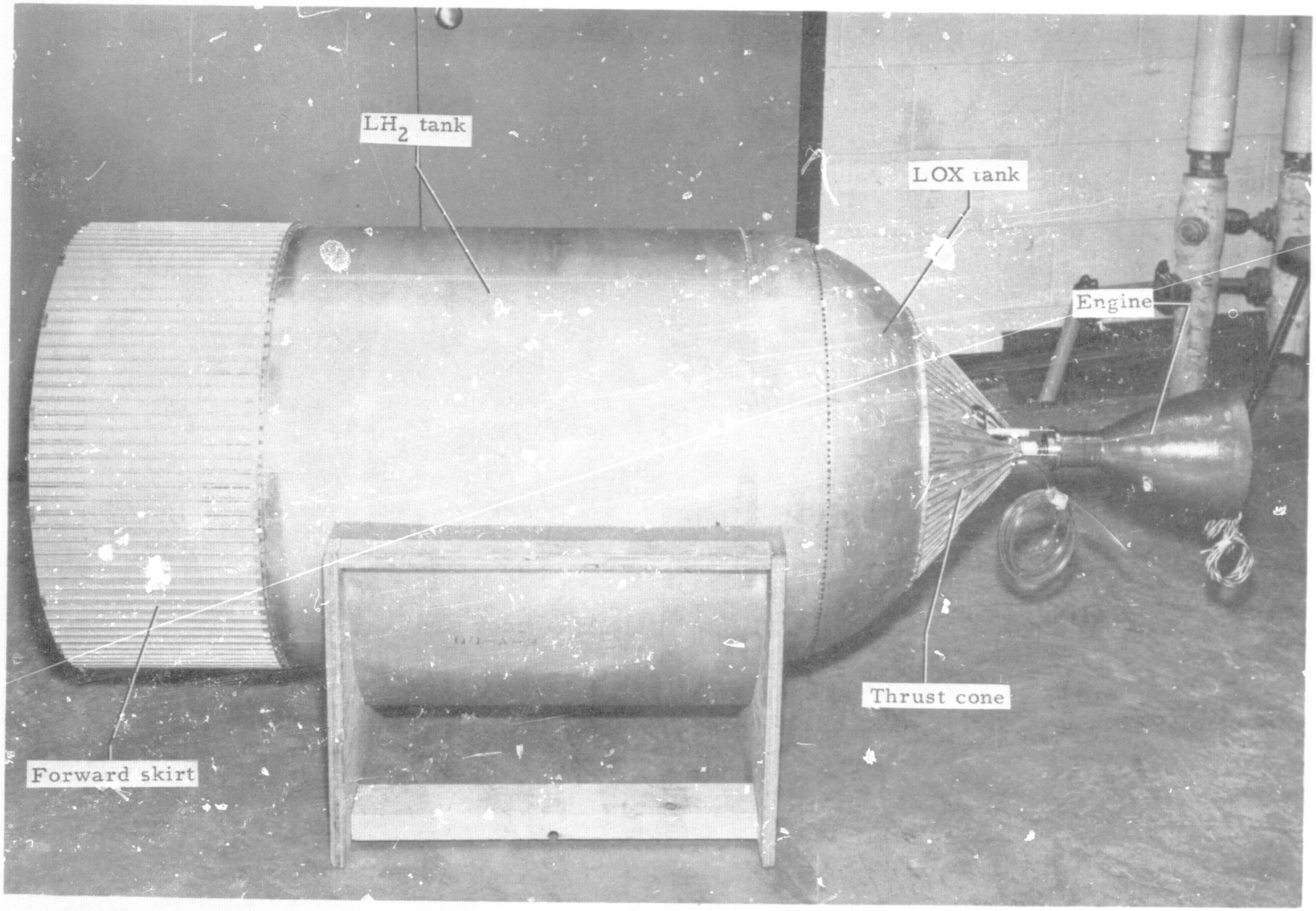

Figure 7.- 1/10-scale model. S-IVB stage final assembly.

L-64-9524.1

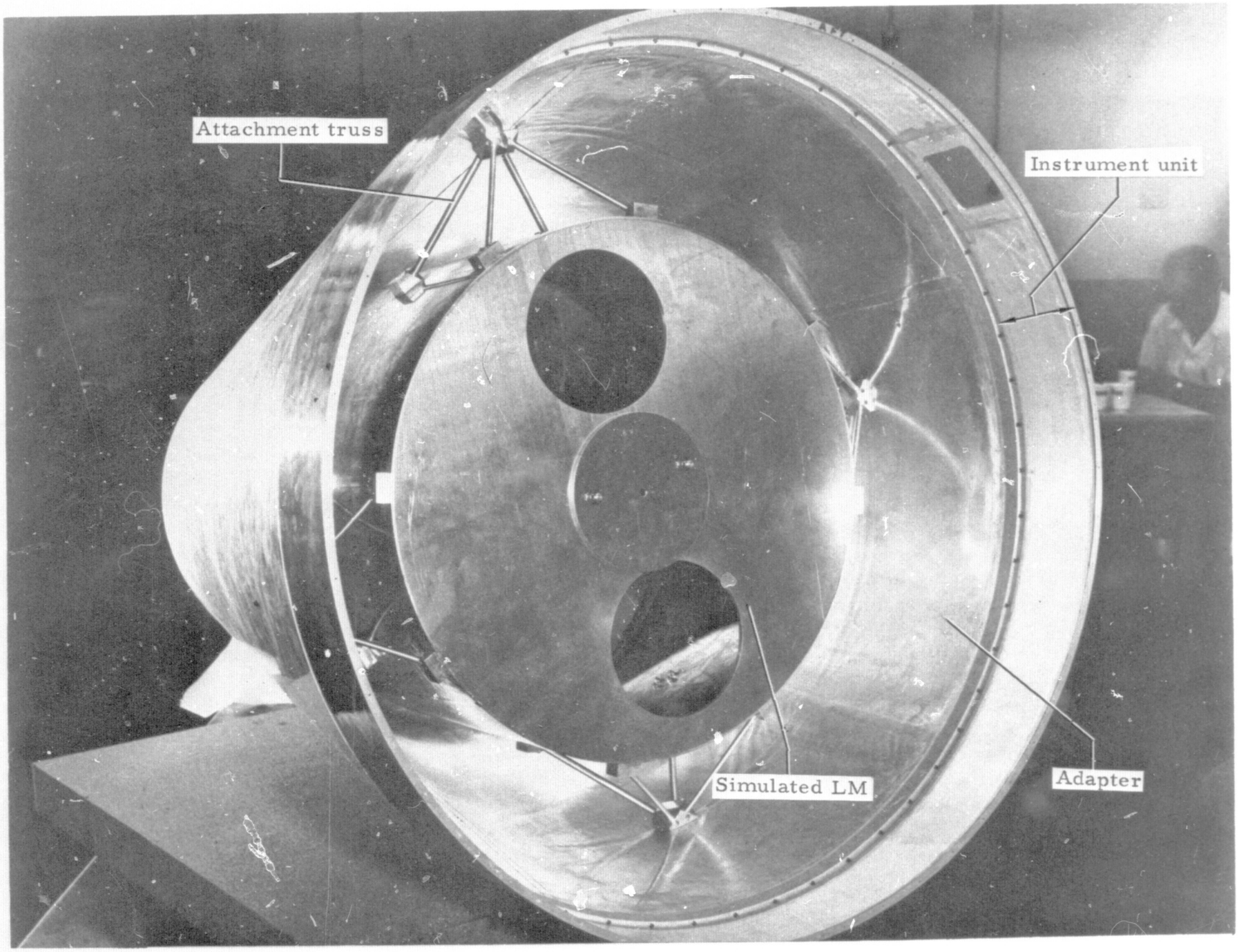

Figure 8.- 1/10-scale model. Simulated LM mounted in adapter structure.

L-67-1035.1

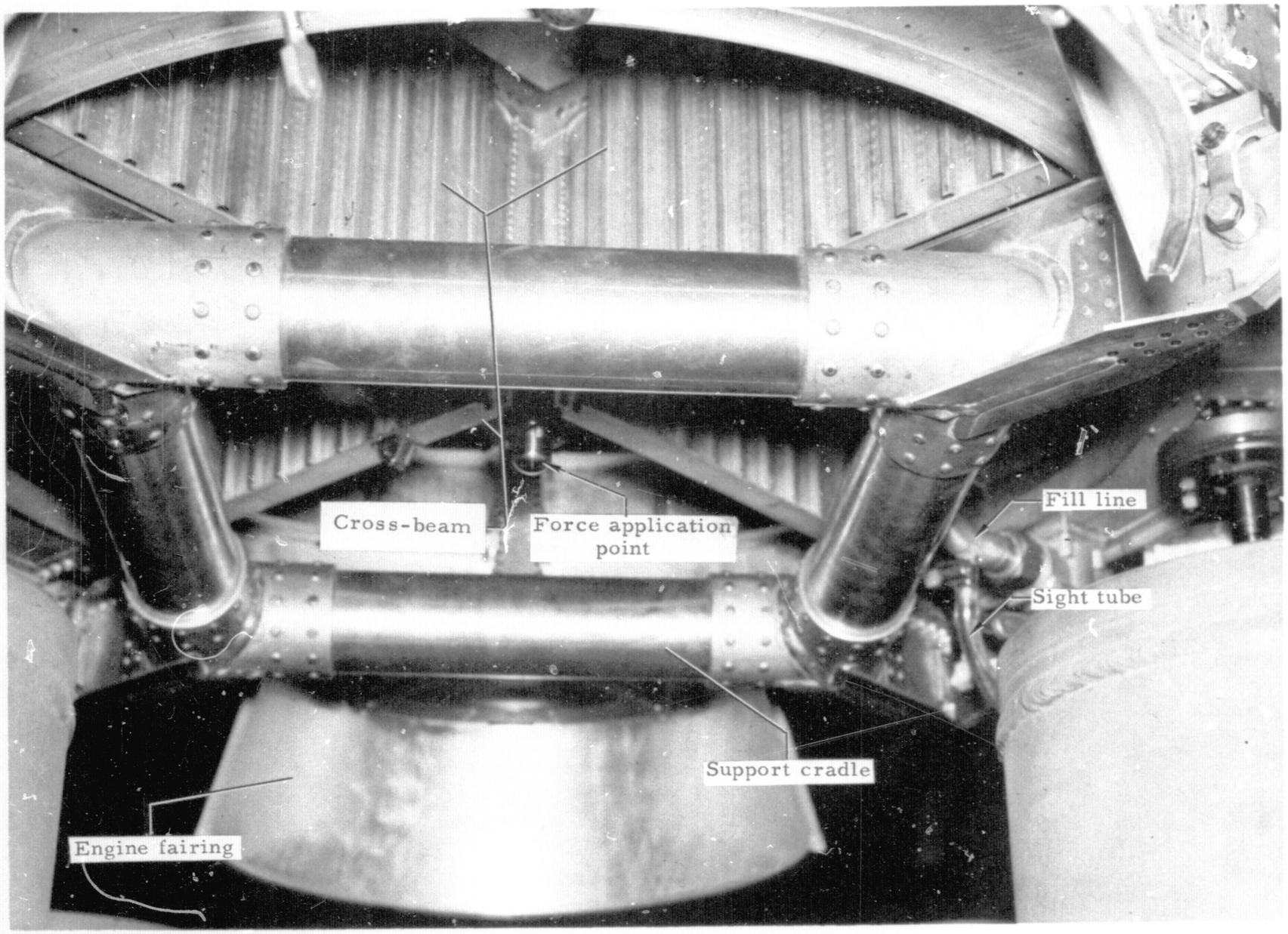

Figure 9.- 1/10-scale model. Support cradle and cross beam.

L-64-10,072.1

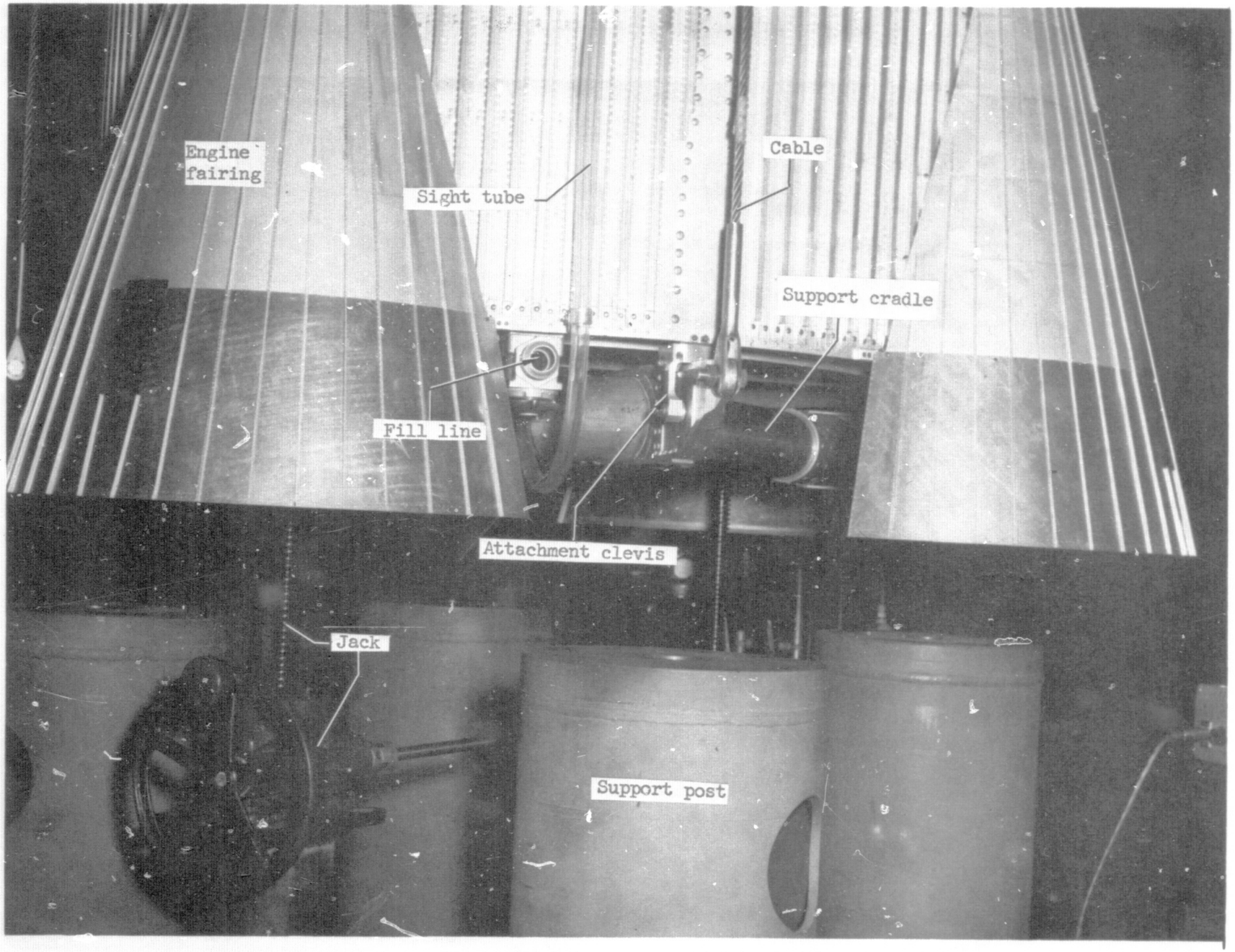

Figure 10.- 1/10-scale model. Support cradle attachment.

L-64-10,075.1

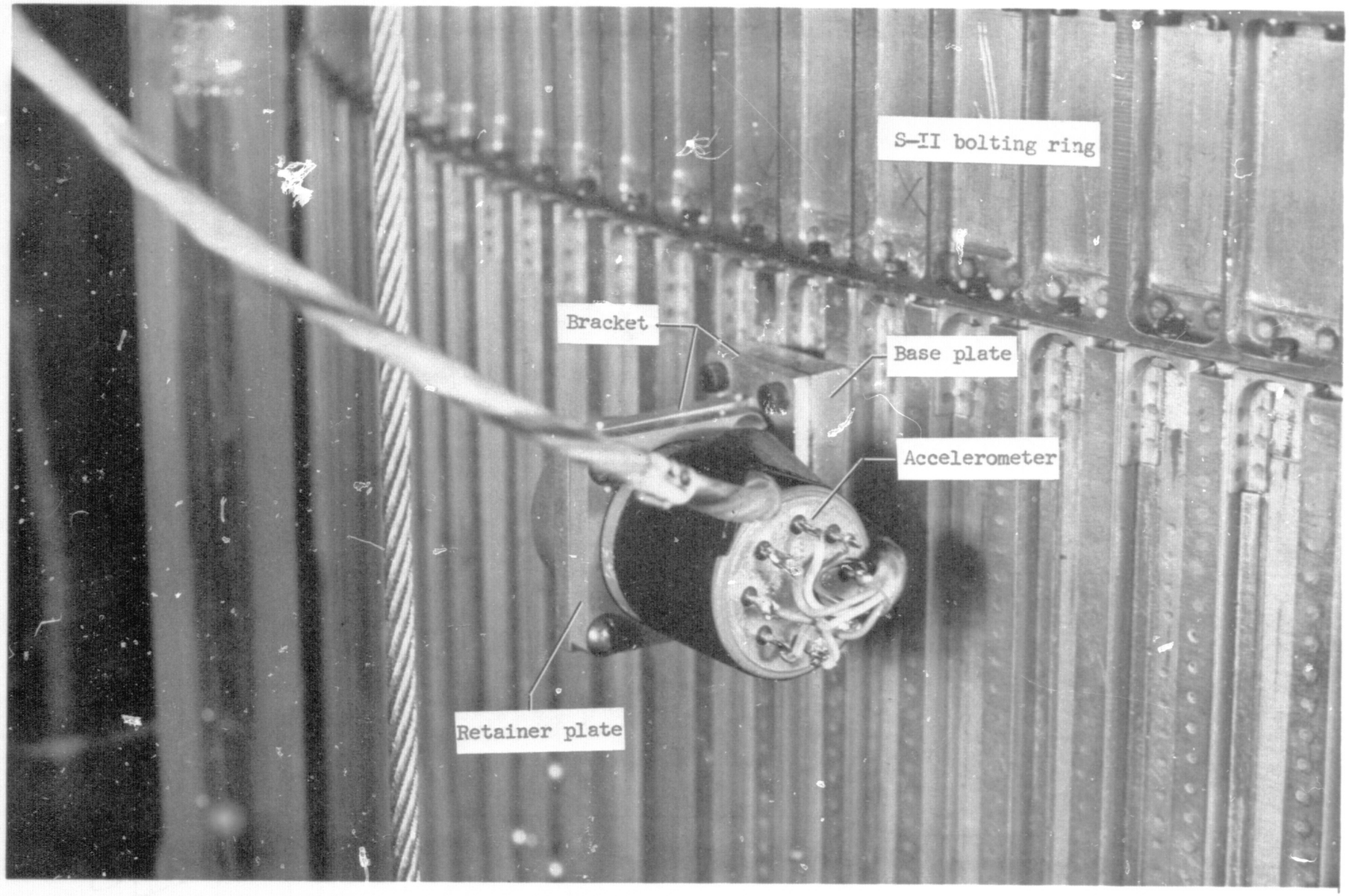

Figure 11.- 1/10-scale model. Typical accelerometer attachment.

L-65-1860.1

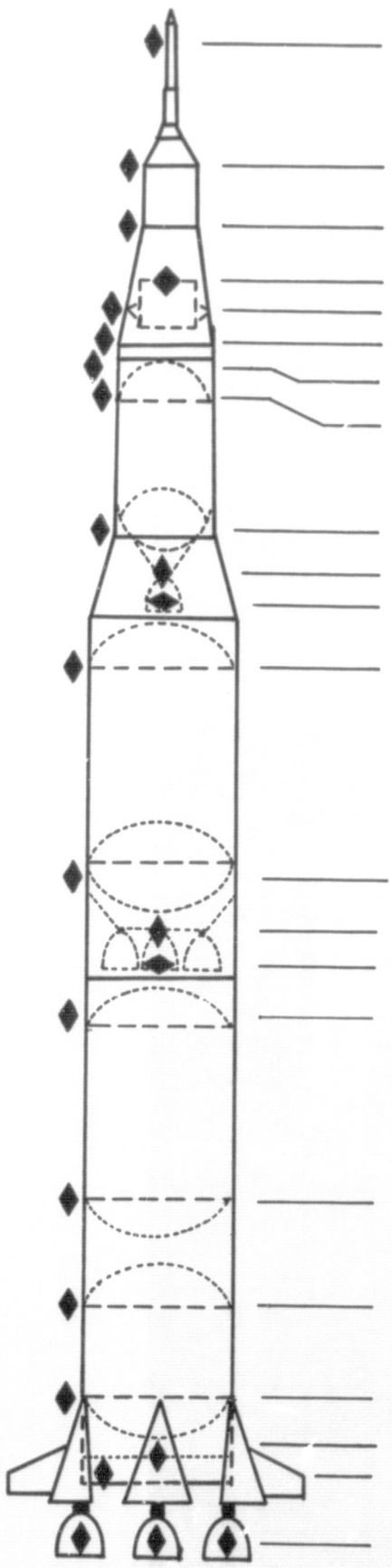

Model station in.	Model station m	Orientation
416.0	10.566	Longitudinal
377.1	9.578	Longitudinal
360.3	9.151	Longitudinal
342.0	8.687	LM Tri-axial
332.6	8.448	Longitudinal
327.4	8.316	Longitudinal
321.1		
312.2	7.930	Longitudinal
275.6	7.000	Longitudinal
266.0	6.756	Longitudinal
254.5	6.464	Pitch and yaw – engine center line
239.5	6.083	Longitudinal
183.4	4.658	Longitudinal
167.1	4.244	Longitudinal–thrust structure center line
156.4	3.972	Pitch and yaw – engine center line
146.9	3.731	Longitudinal
84.7	2.151	Longitudinal
64.2	1.631	Longitudinal
33.0	0.838	Longitudinal
20.5	0.521	Longitudinal–thrust structure center line
12.4	0.315	Longitudinal
–2.0	–0.051	Longitudinal – center line all engines

Figure 12.- Schematic of transducer locations and orientations.

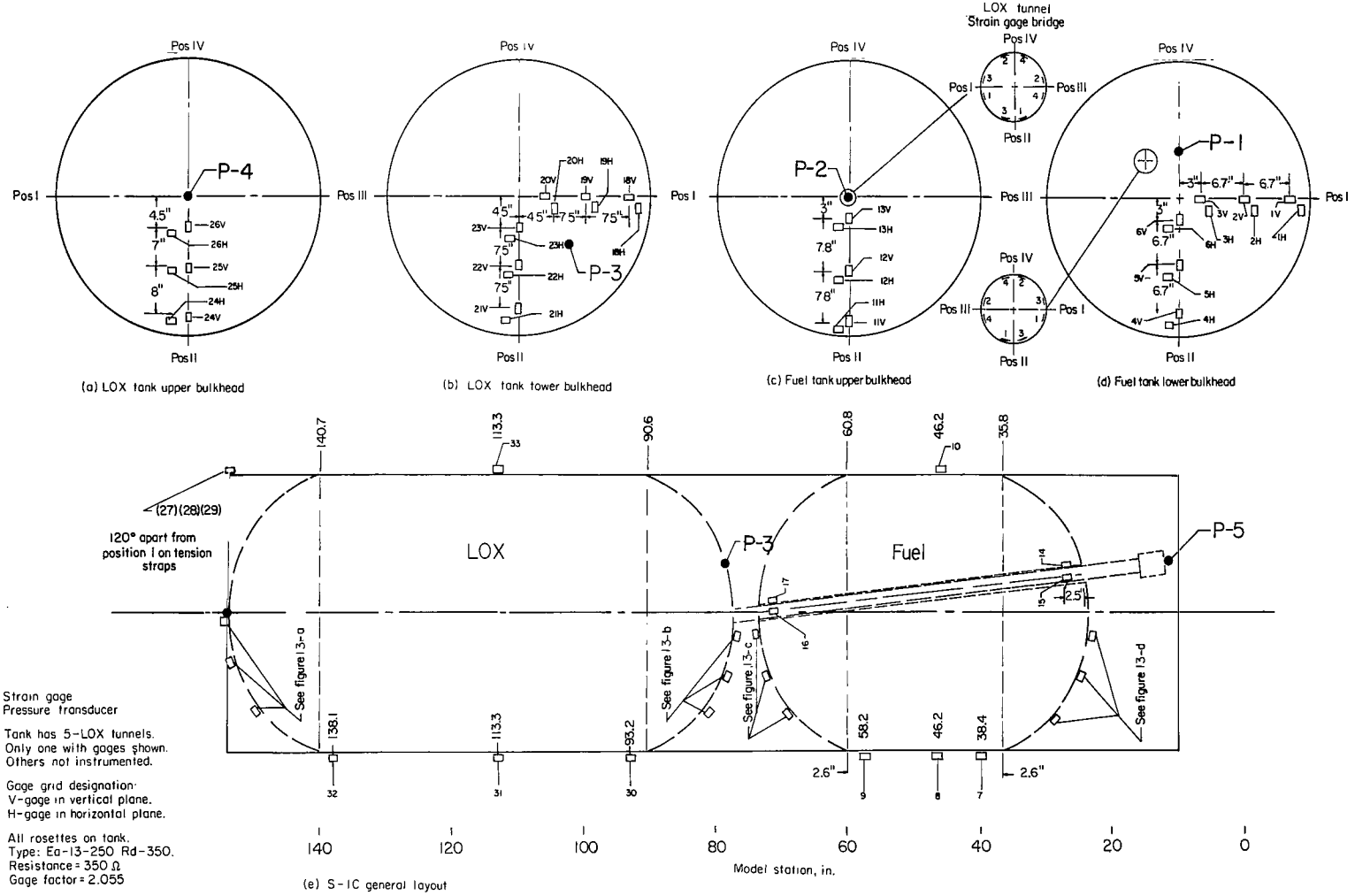

Figure 13.- Schematic of strain and pressure transducer locations and orientations in model S-IC stage.

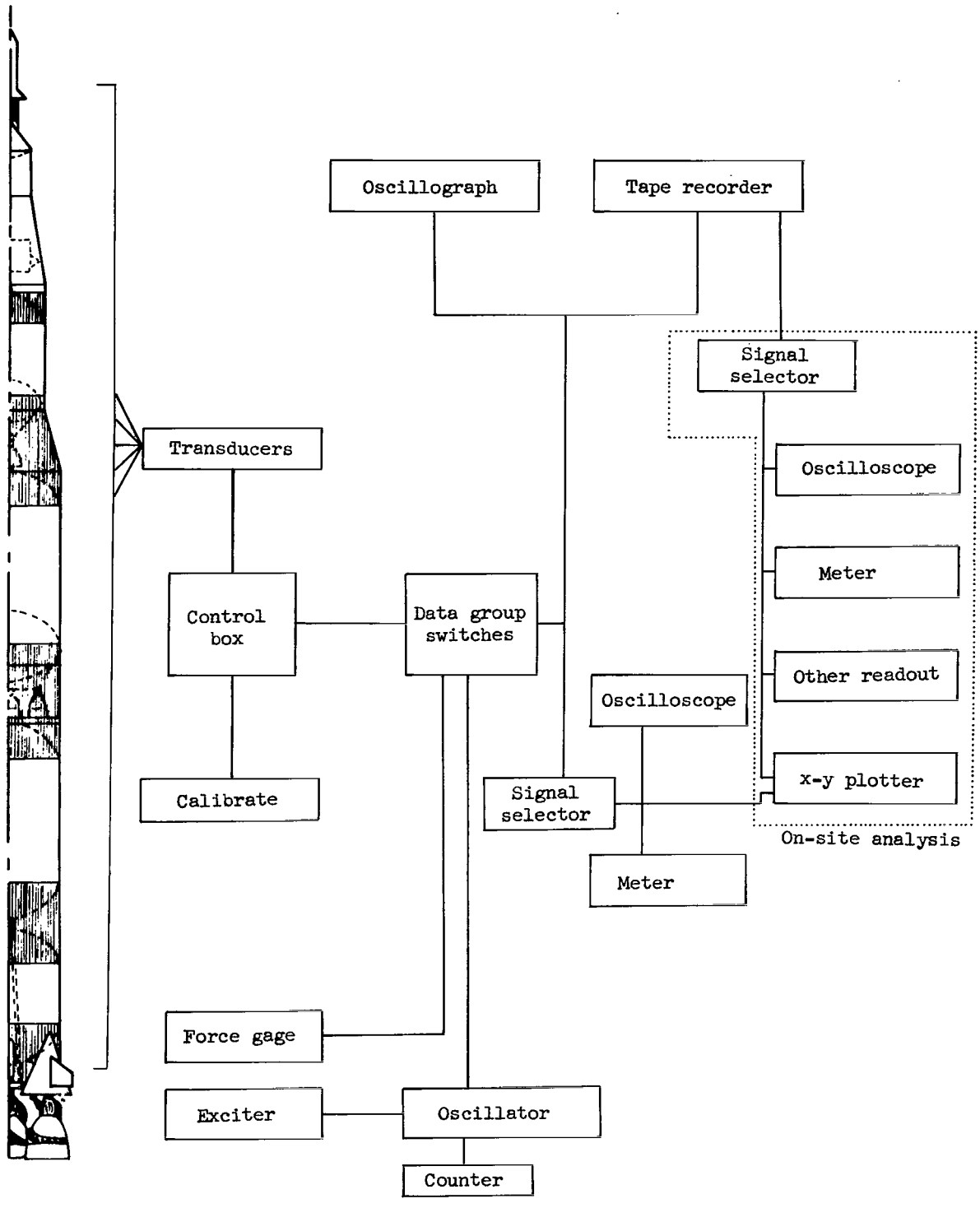

Figure 14.- Schematic of instrumentation.

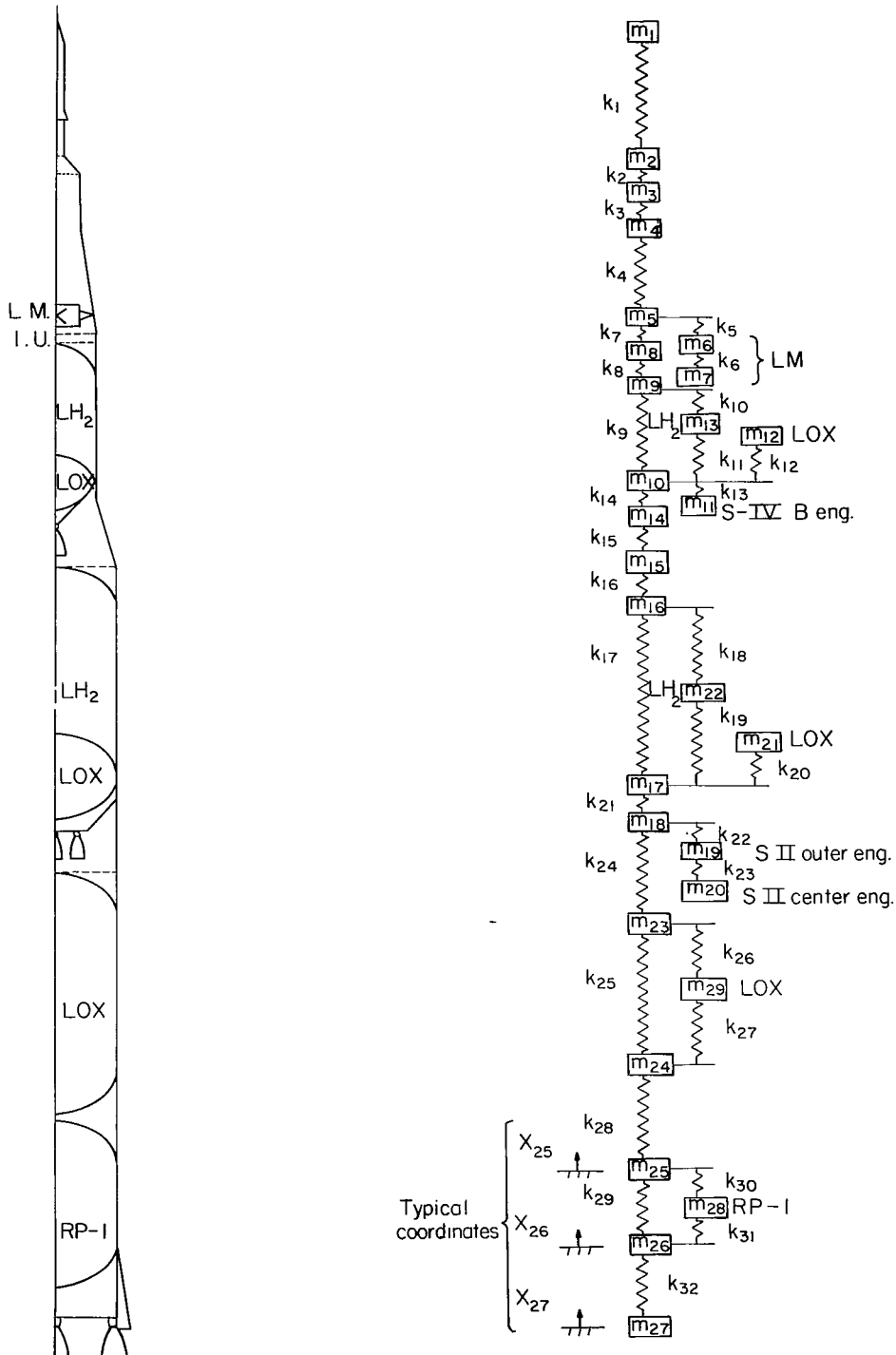

Figure 15.- Lumped-parameter analytical model.

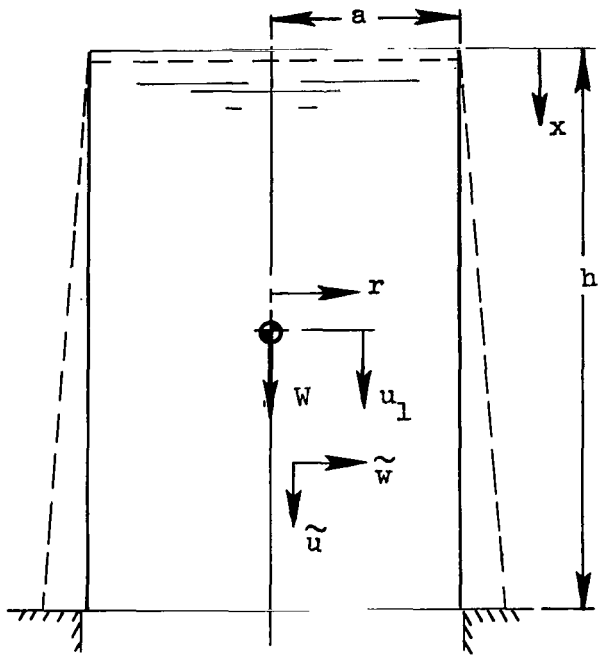

Figure 16.- Idealized propellant tank.

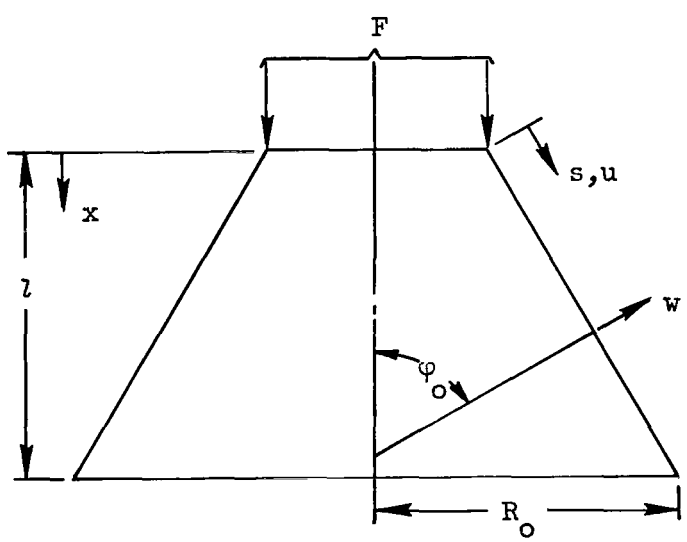

Figure 17.- Typical conical shell.

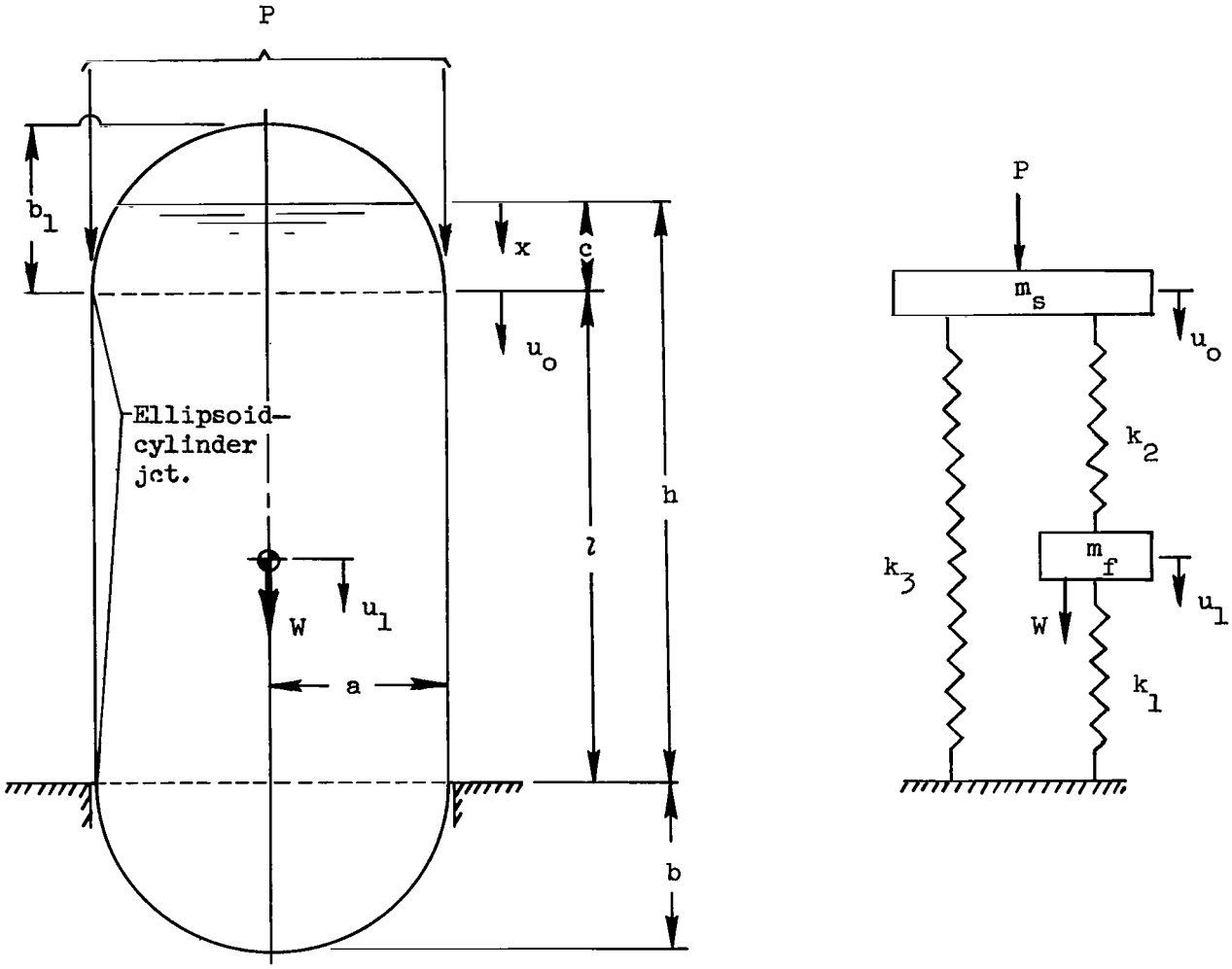

Figure 18.- Typical propellant tank and equivalent lumped parameter model.

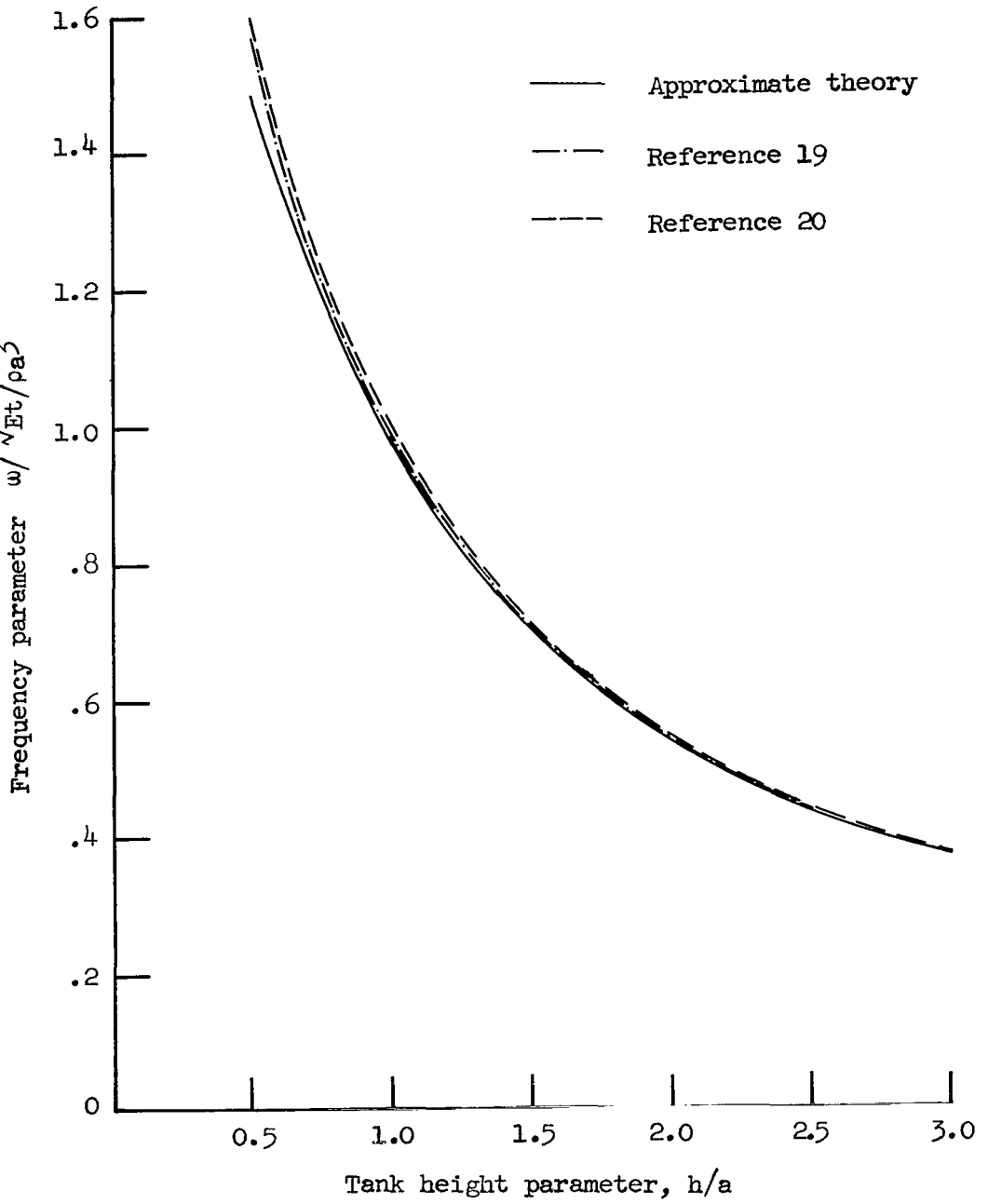

Figure 19.- Comparison of frequencies from approximate and rigorous theories for simplified tank-propellant bulging mode.

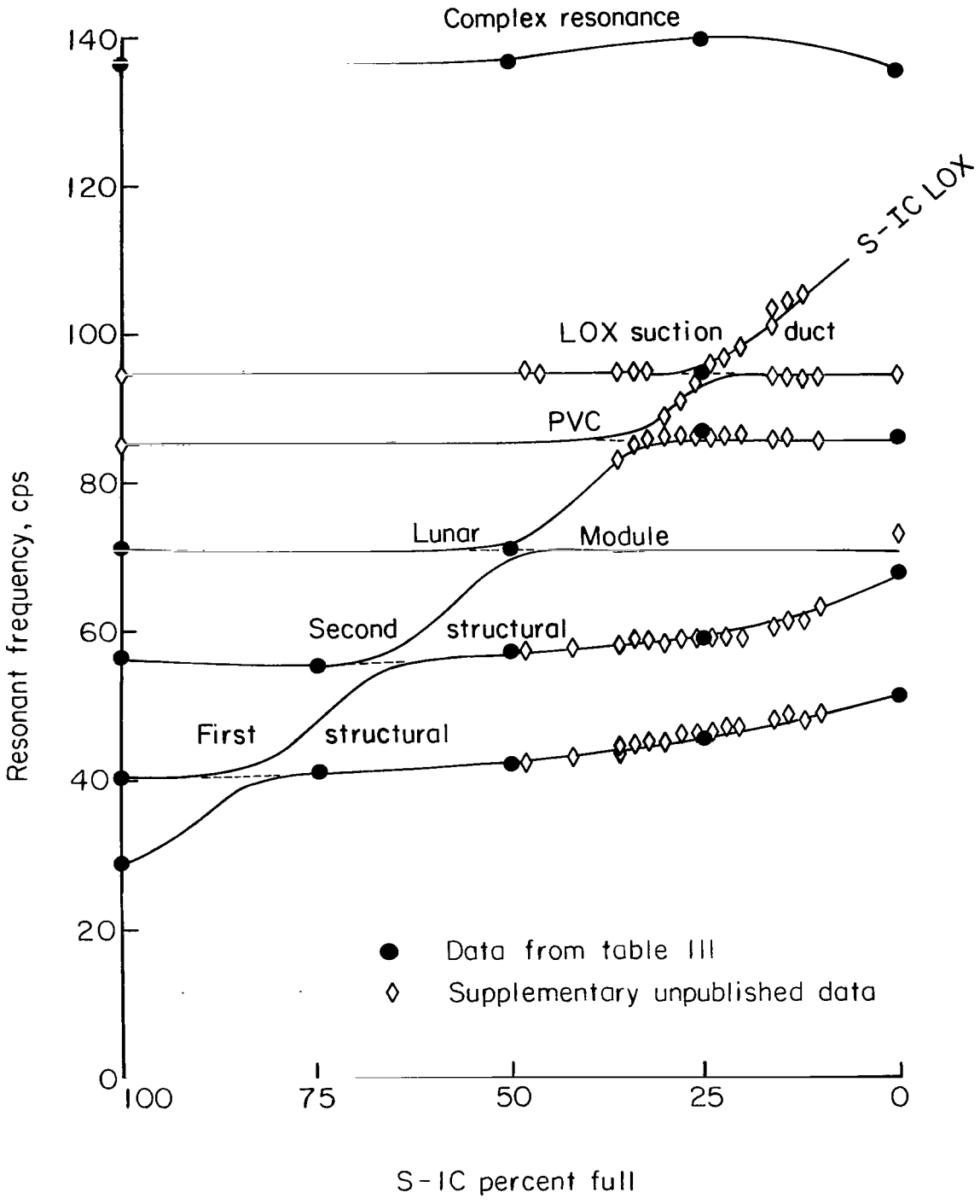

Figure 20.- Summary plot of experimental resonant frequencies as a function of S-IC propellant loading.

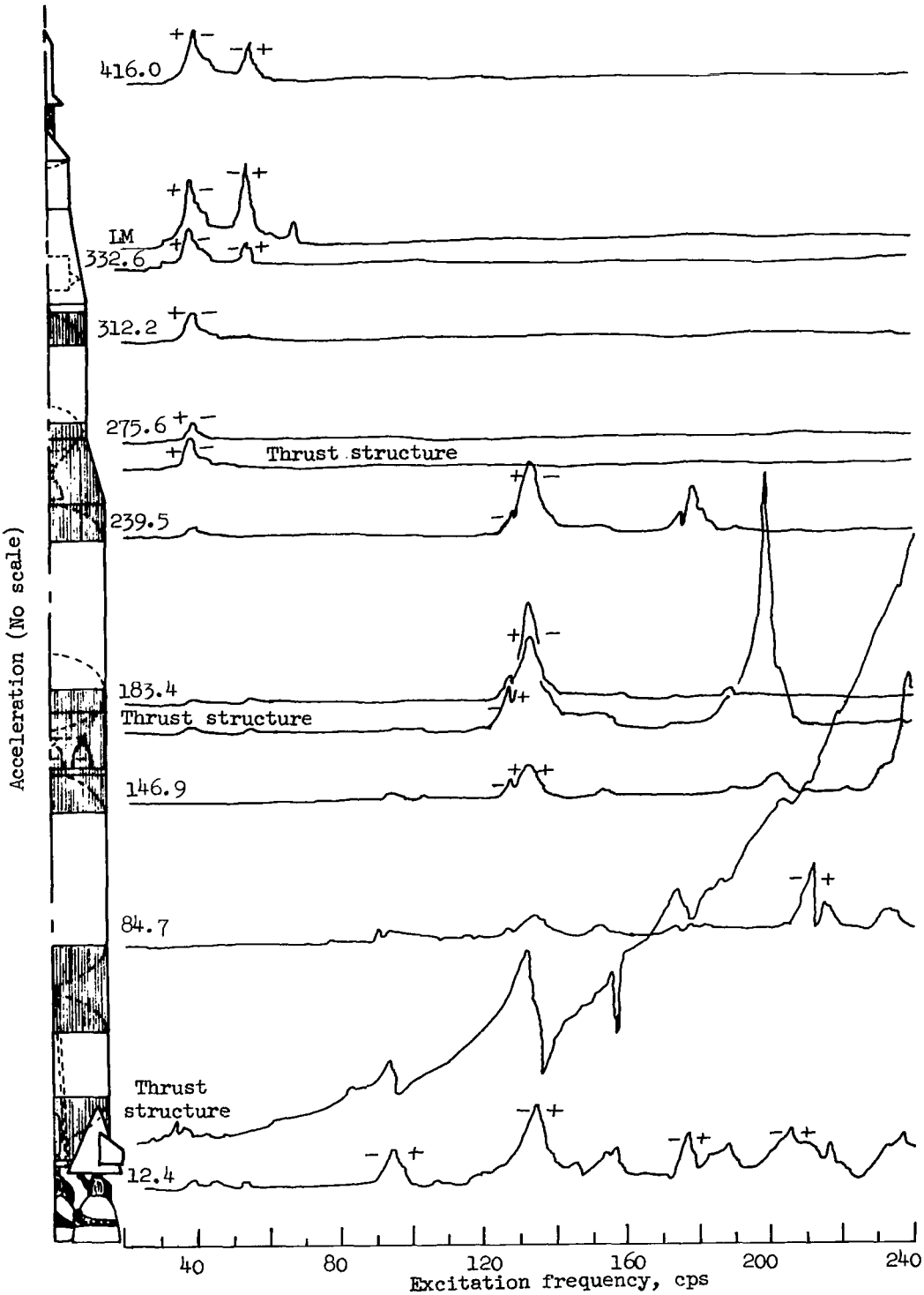

Figure 21.- Acceleration as a function of frequency for S-IC 100 percent full. Force, 6 lb (27 N).

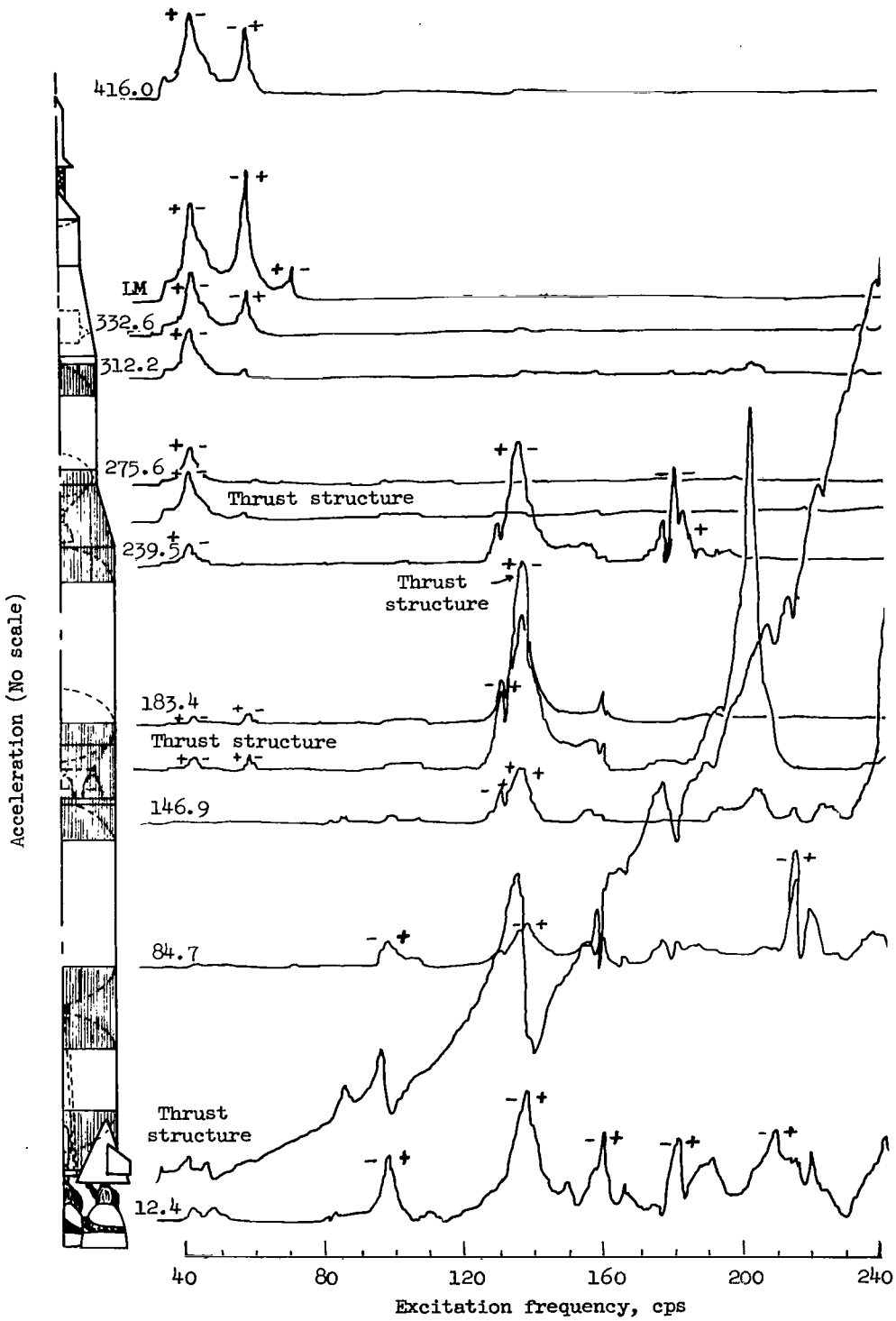

Figure 22.- Acceleration as a function of frequency for S-IC 100 percent full. Force, 12 lb (53 N).

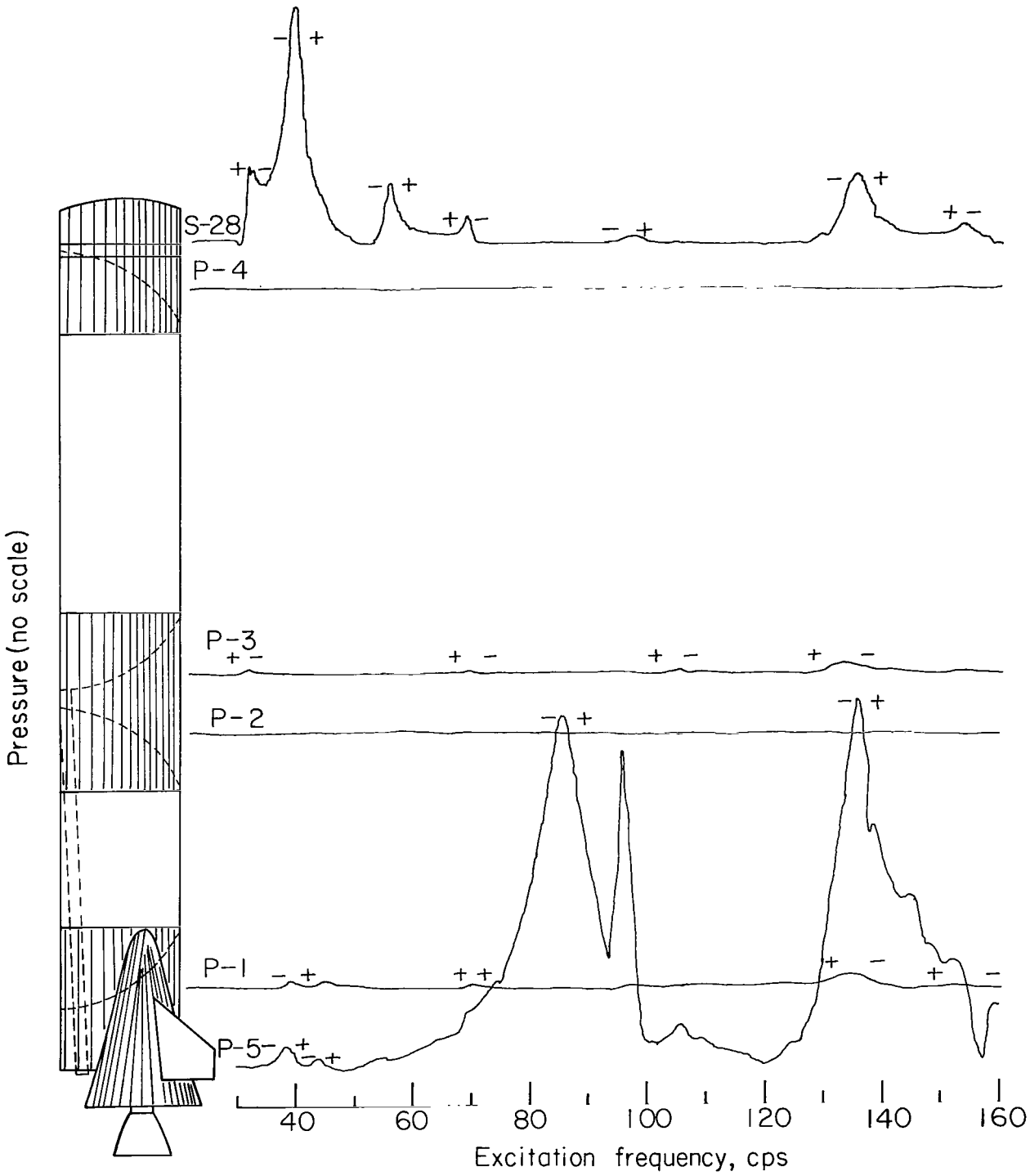

Figure 23.- Variation of pressure with frequency. S-IC 100 percent full.

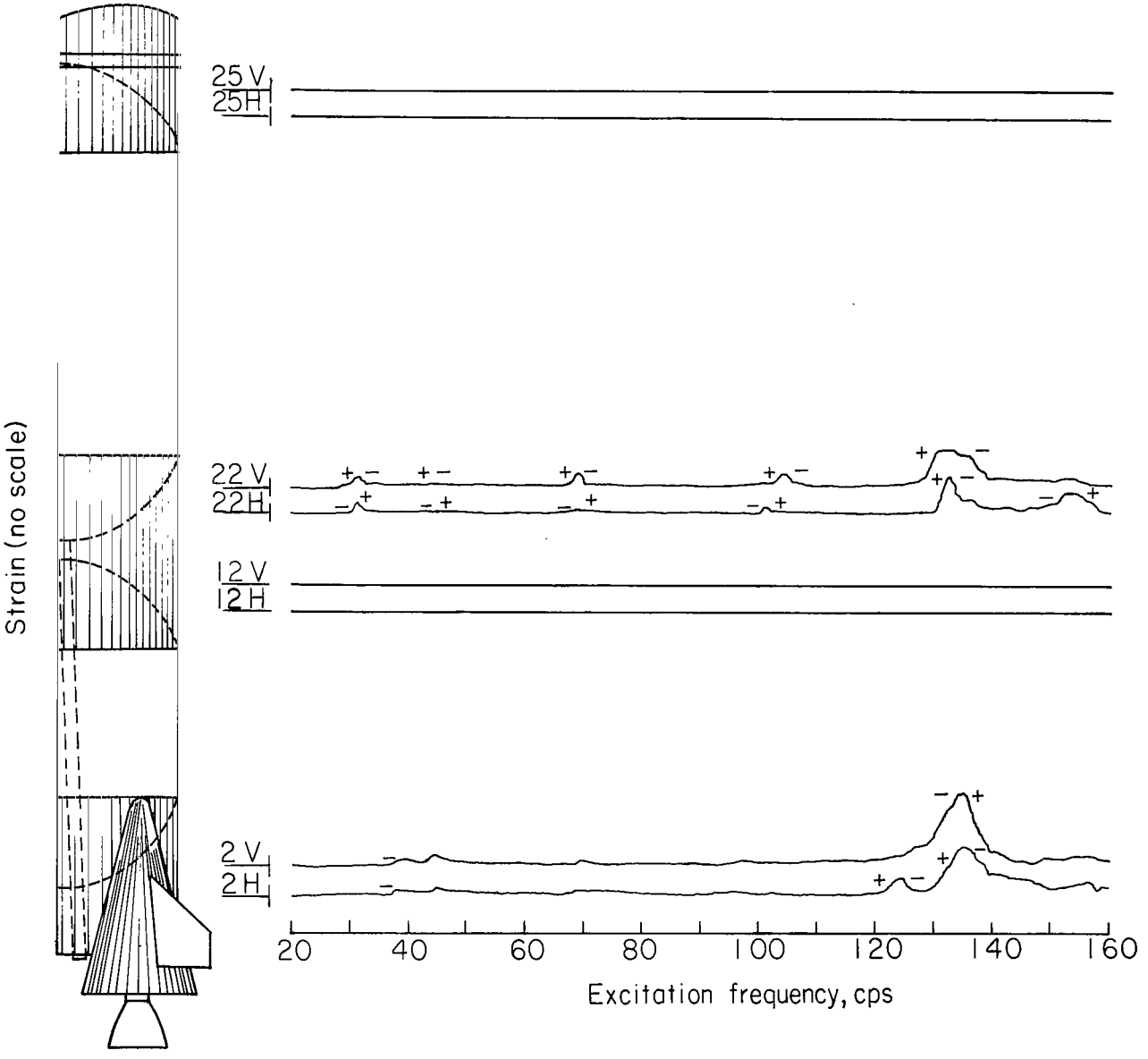

Figure 24.- Variation of bulkhead strain with frequency. S-IC 100 percent full.

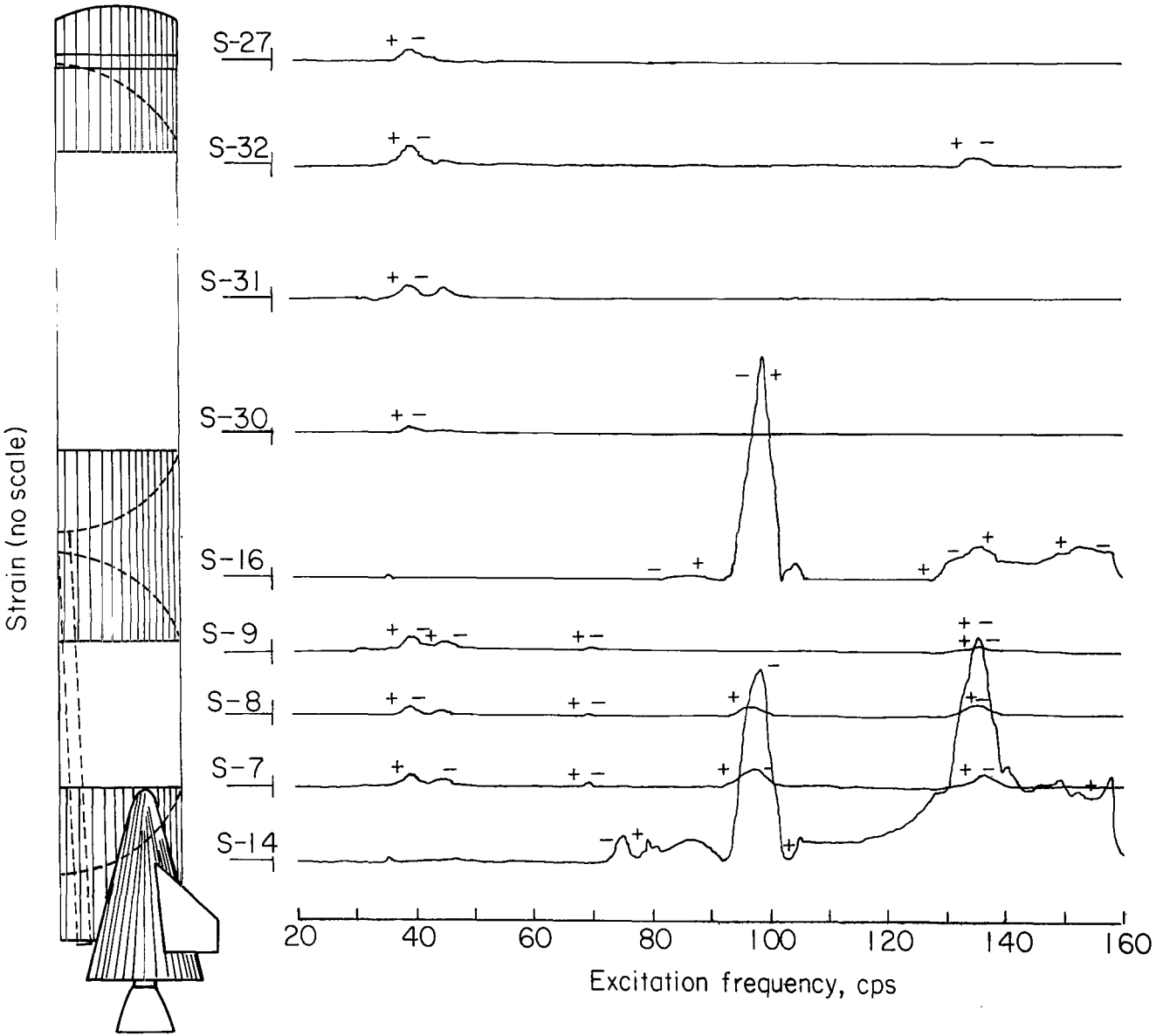

Figure 25.- Variation of surface strain with frequency. S-IC 100 percent full.

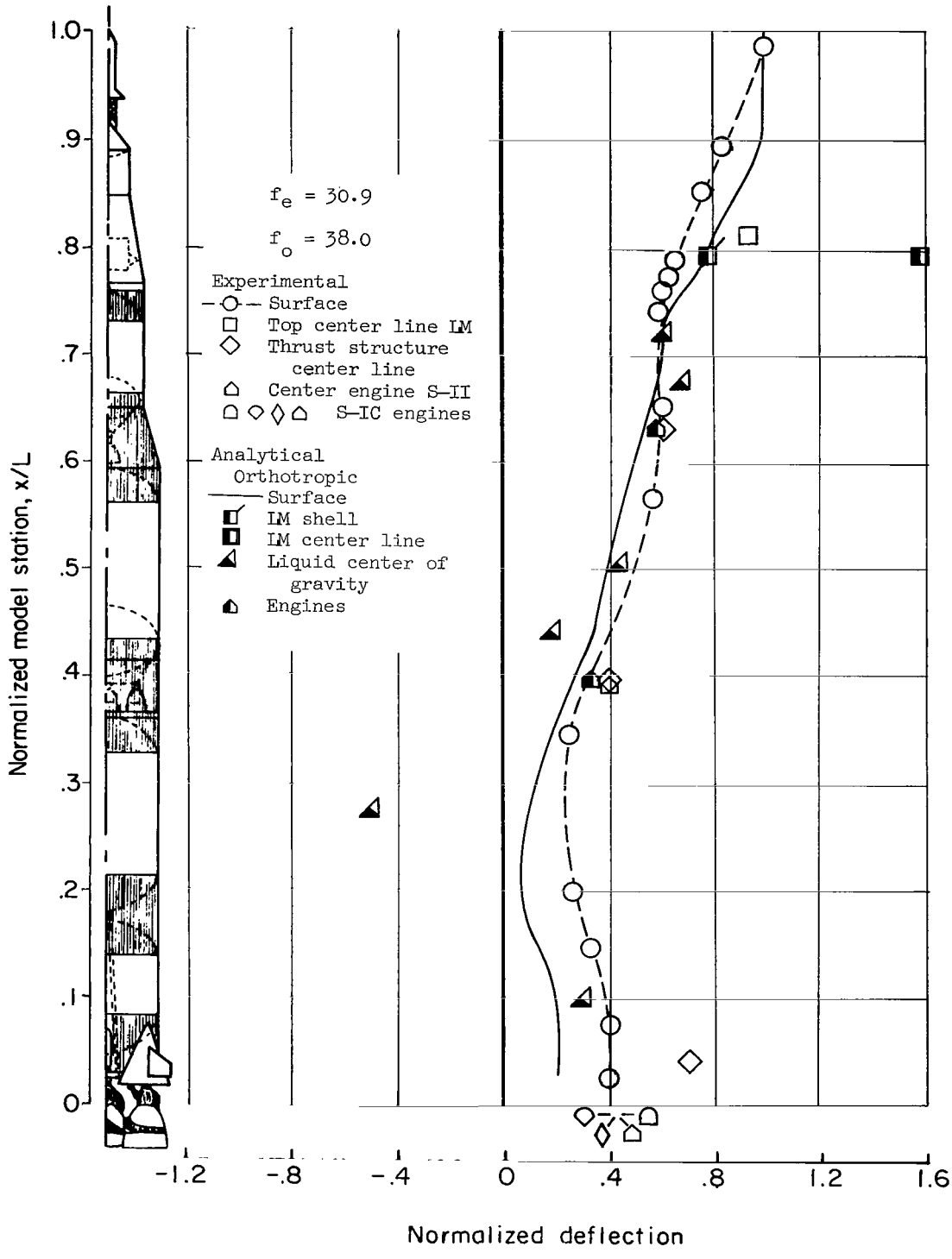

Figure 26.- Experimental and analytical deflection shapes for first resonance of 100-percent full condition.

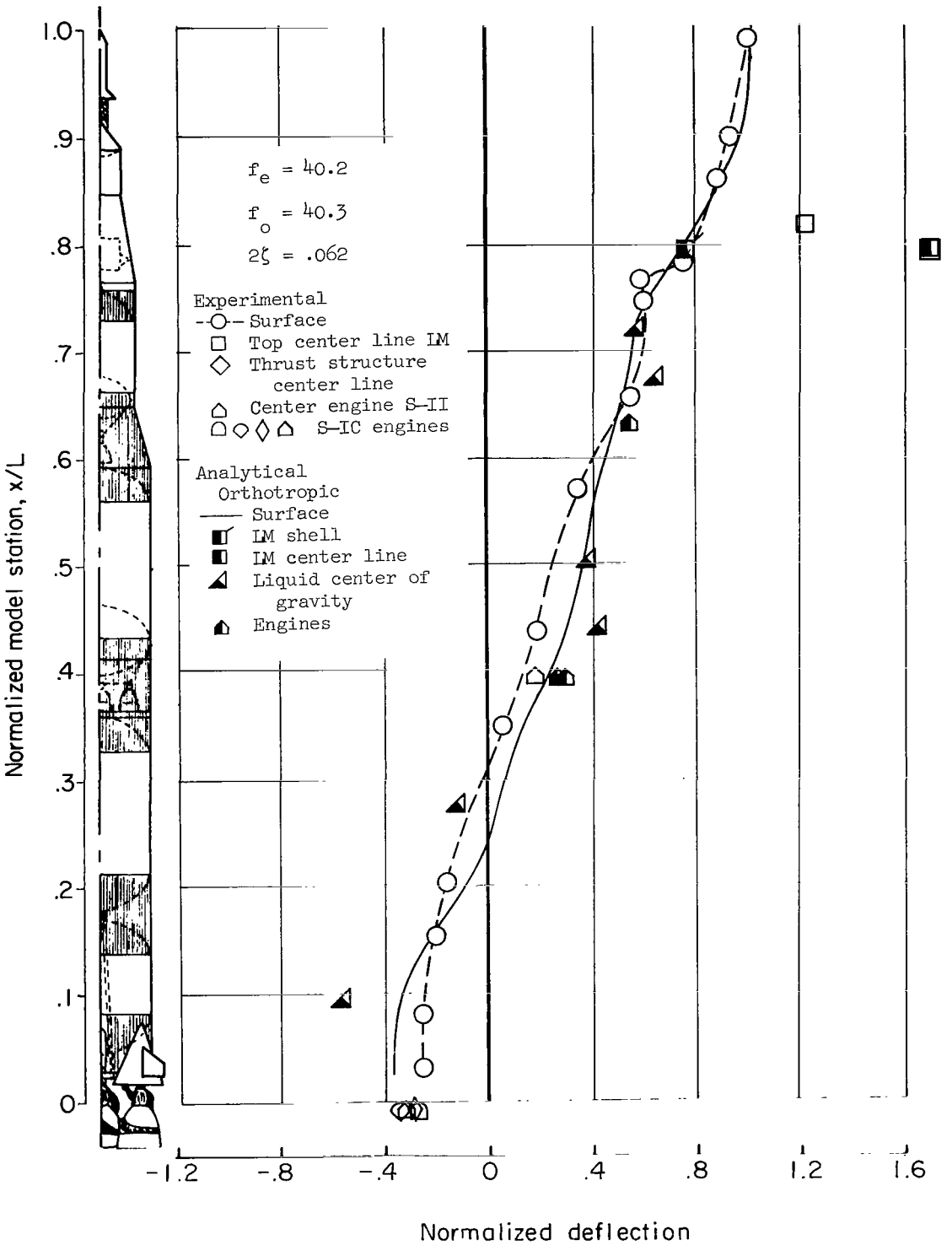

Figure 27.- Experimental and analytical deflection shapes for second resonance of 100-percent full condition.

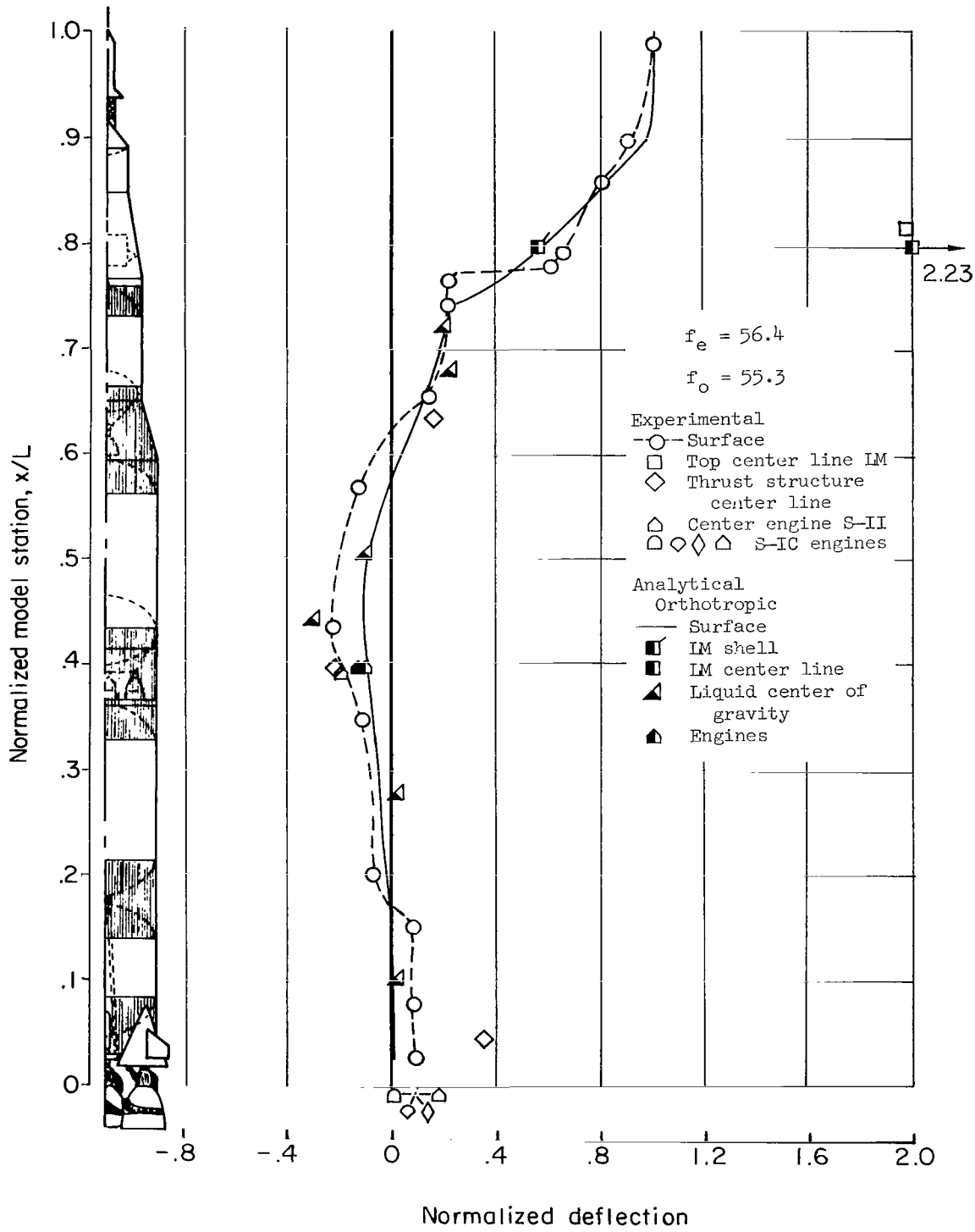

Figure 28.- Experimental and analytical deflection shapes for third resonance of 100-percent full condition.

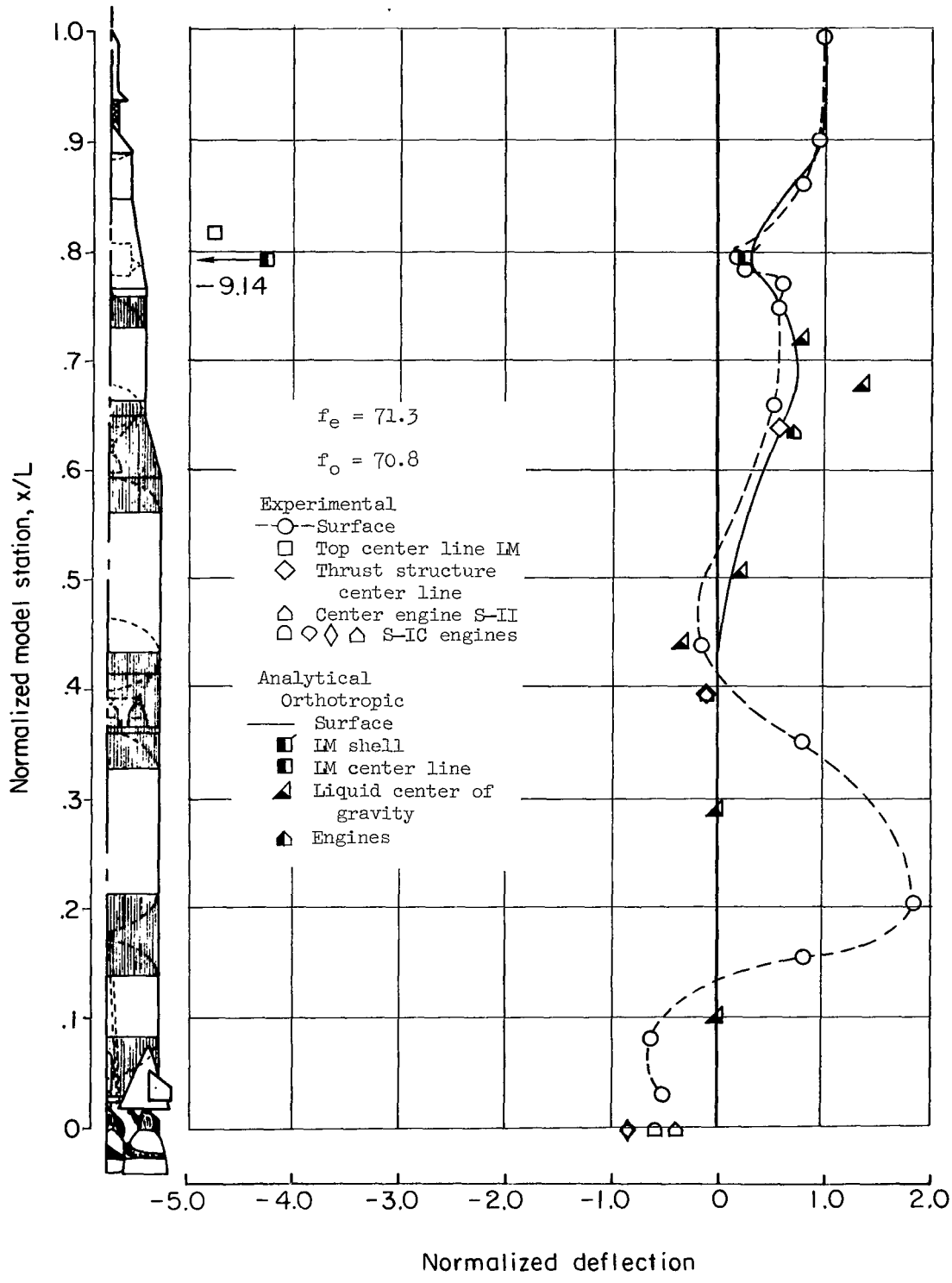

Figure 29.- Experimental and analytical deflection shapes for fourth resonance of 100-percent full condition.

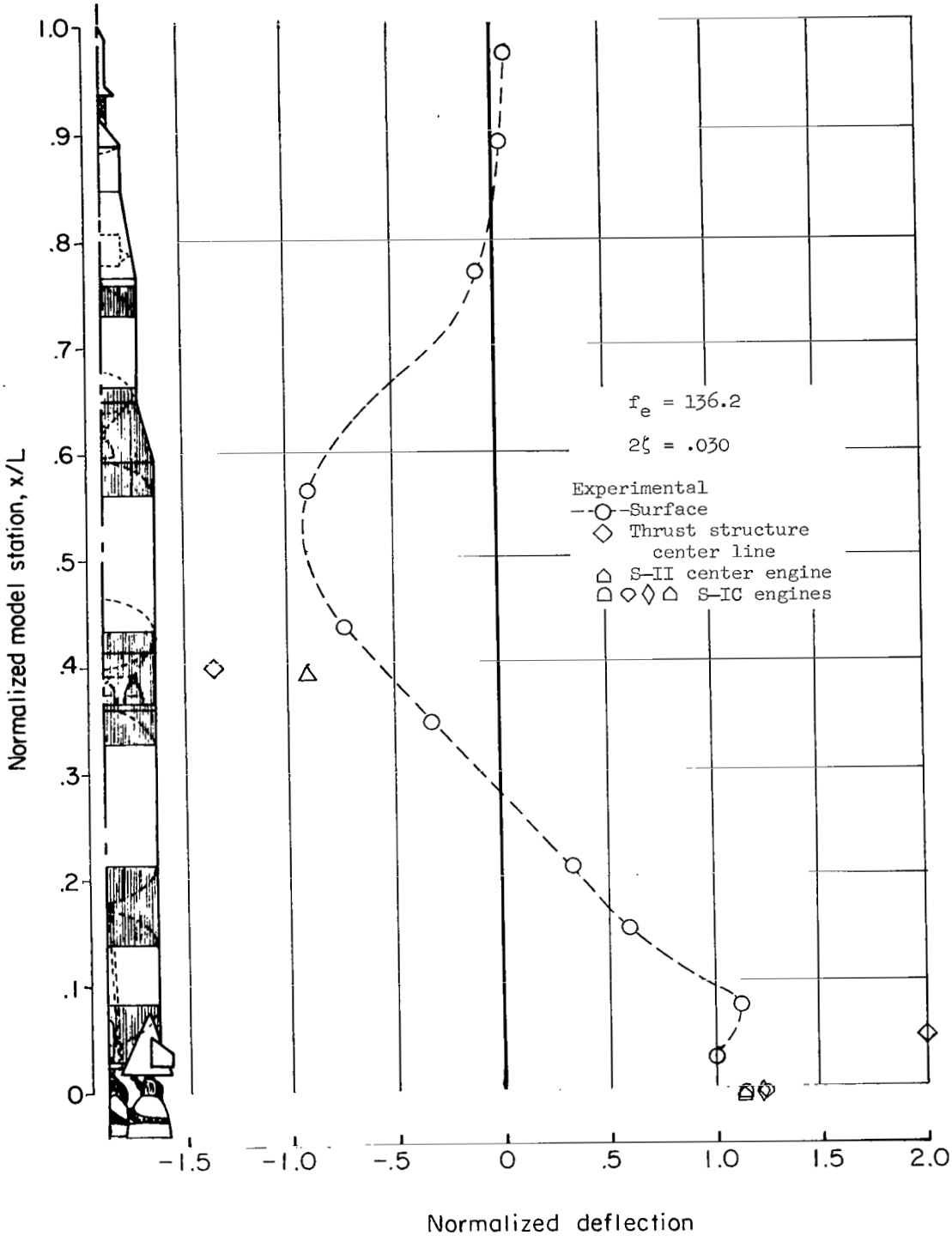

Figure 30.- Experimental deflection shape for fifth resonance of 100-percent full condition.

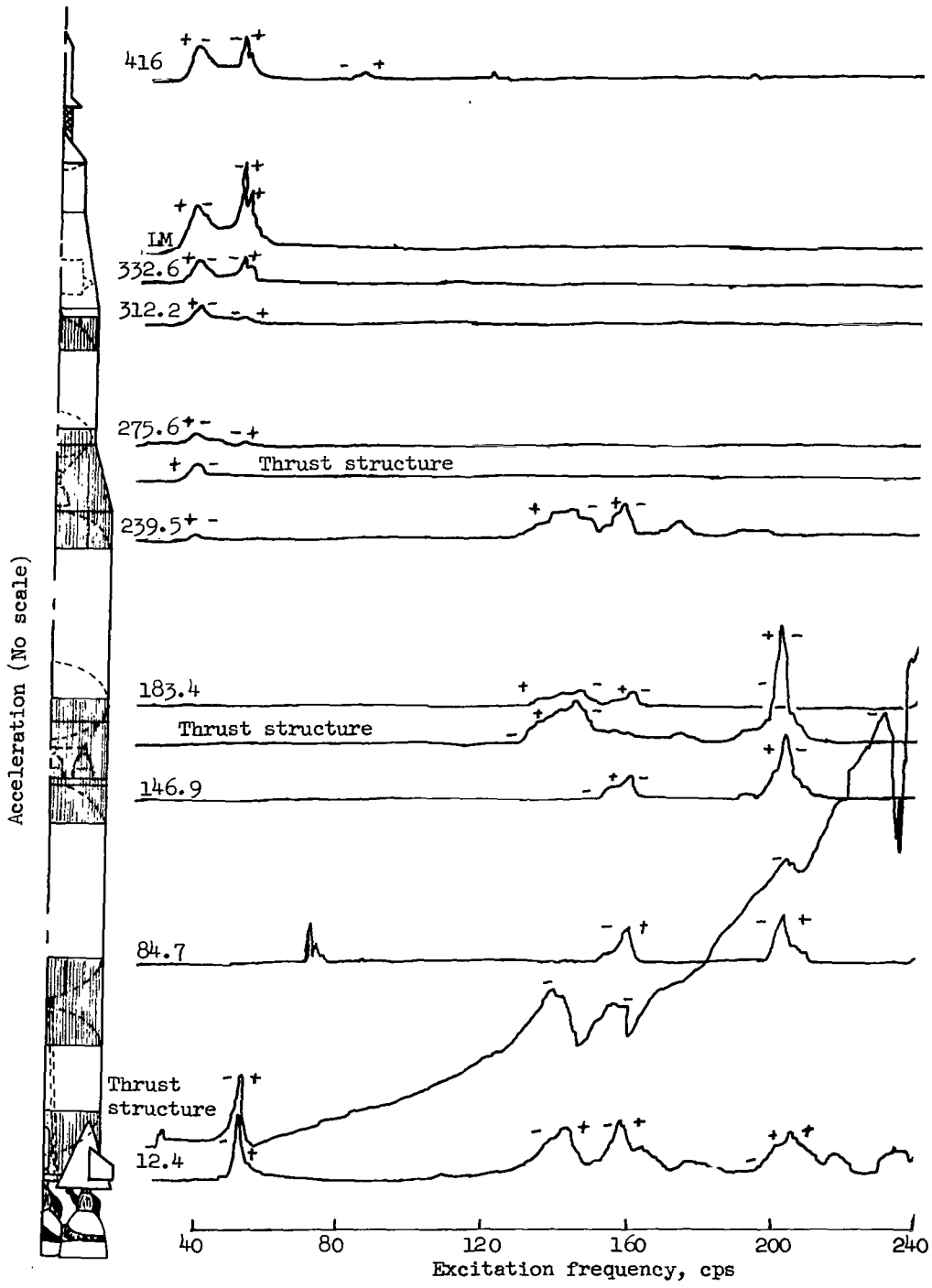

Figure 31.- Variation of acceleration with frequency. S-IC 75 percent full; force, 6 lb (27 N).

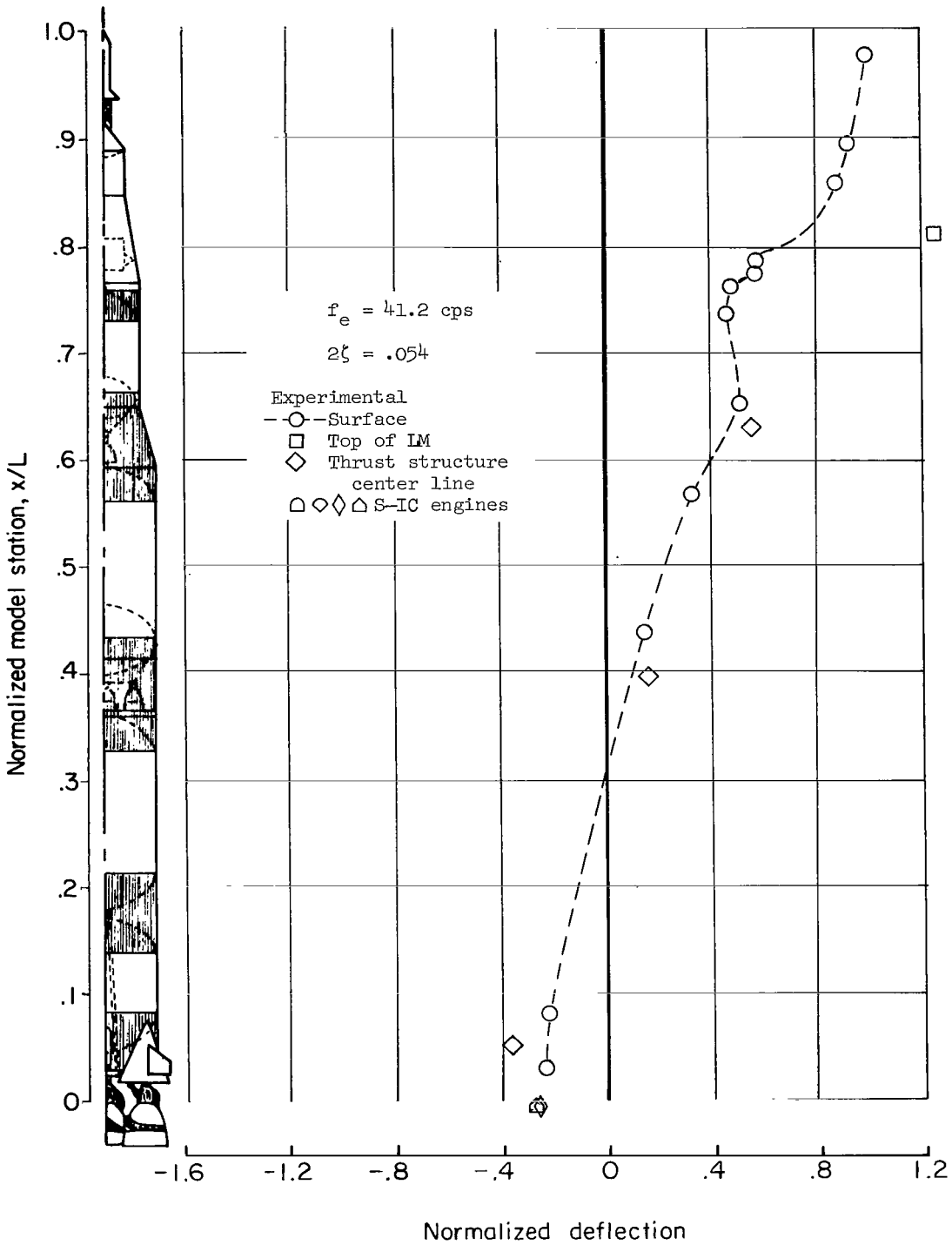

Figure 32.- Experimental deflection shape for first resonance of 75-percent full condition.

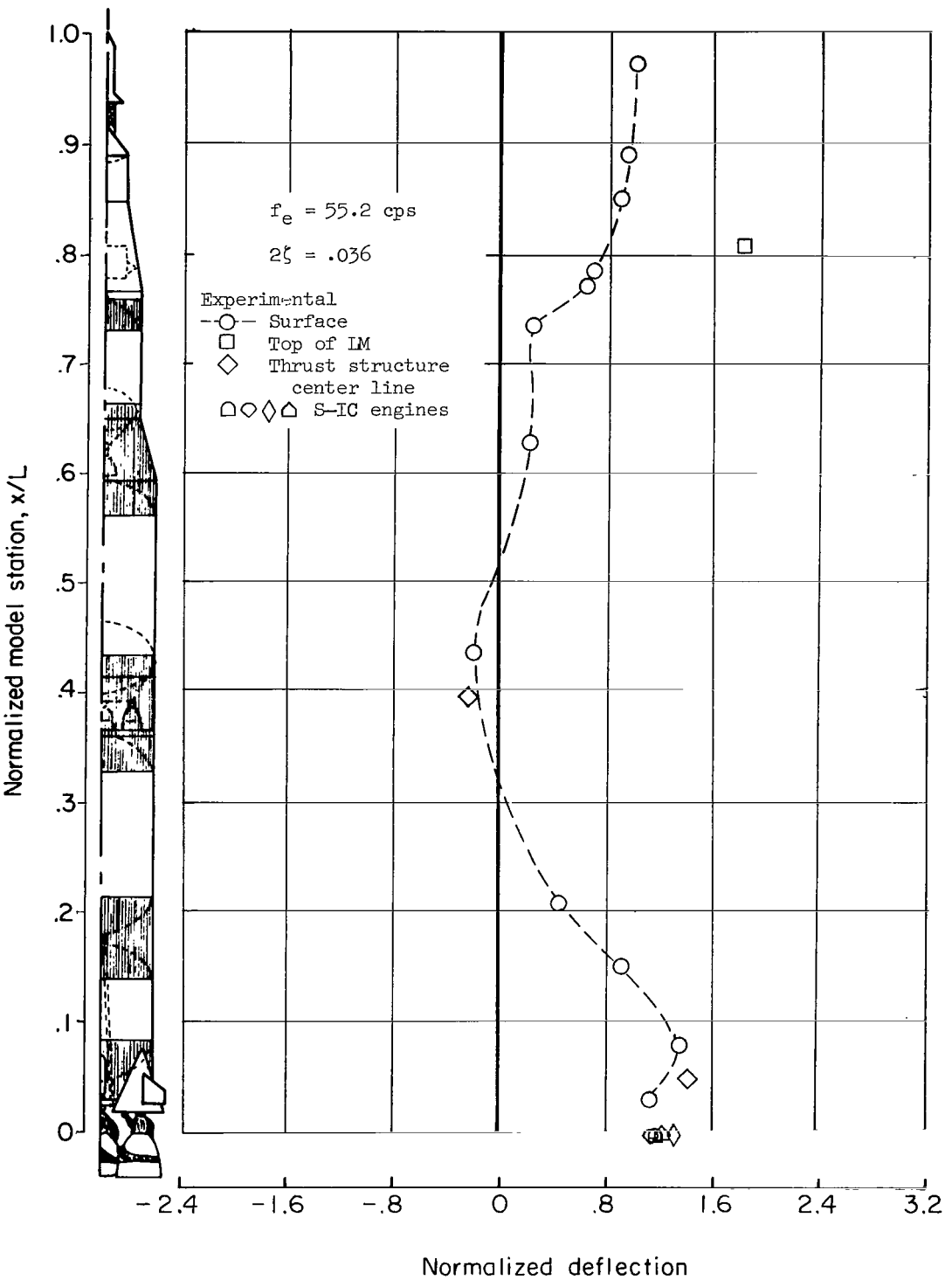

Figure 33.- Experimental deflection shape for second resonance of 75-percent full condition.

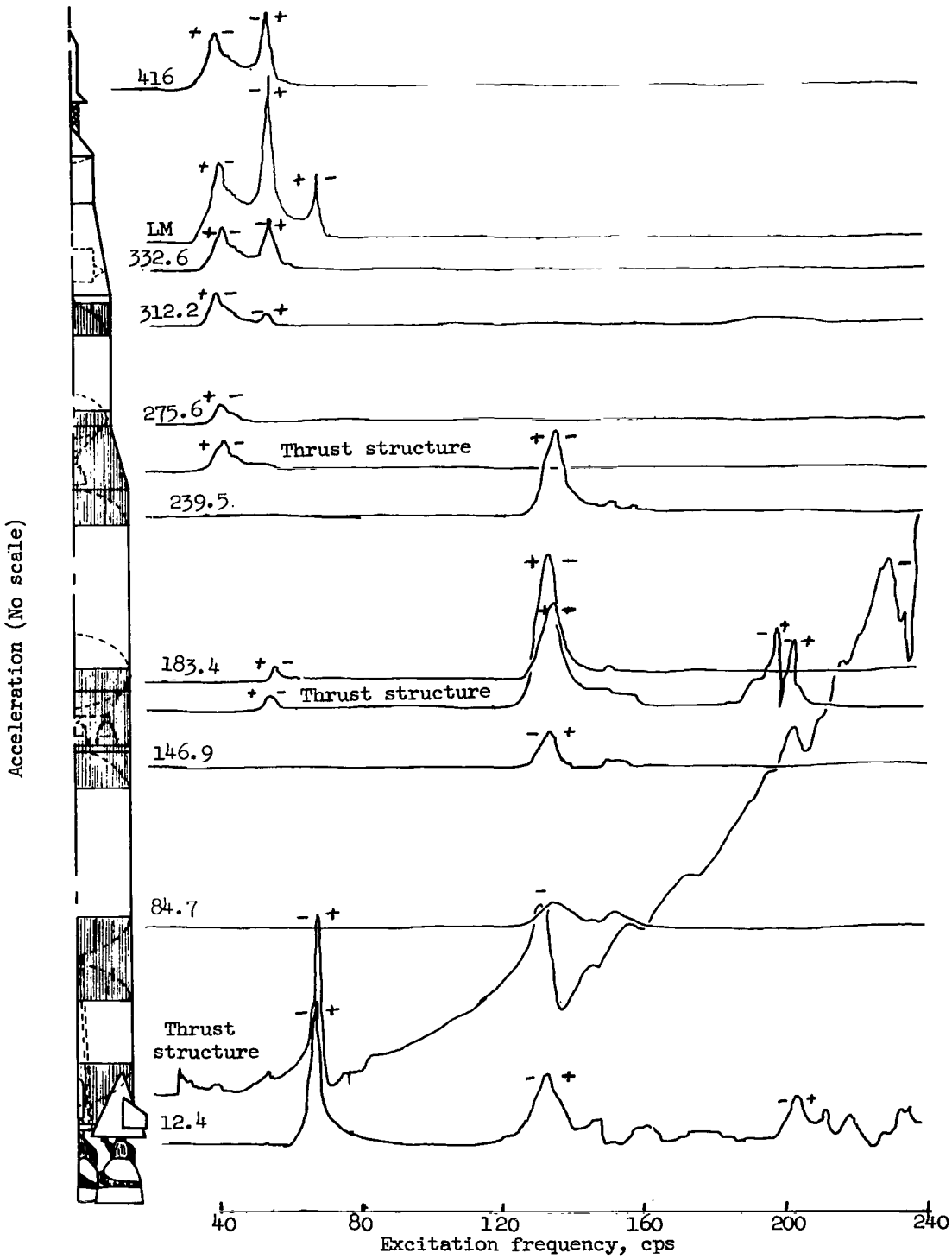

Figure 34.- Variation of full acceleration with frequency. S-IC 50 percent full; force, 6 lb (27 N).

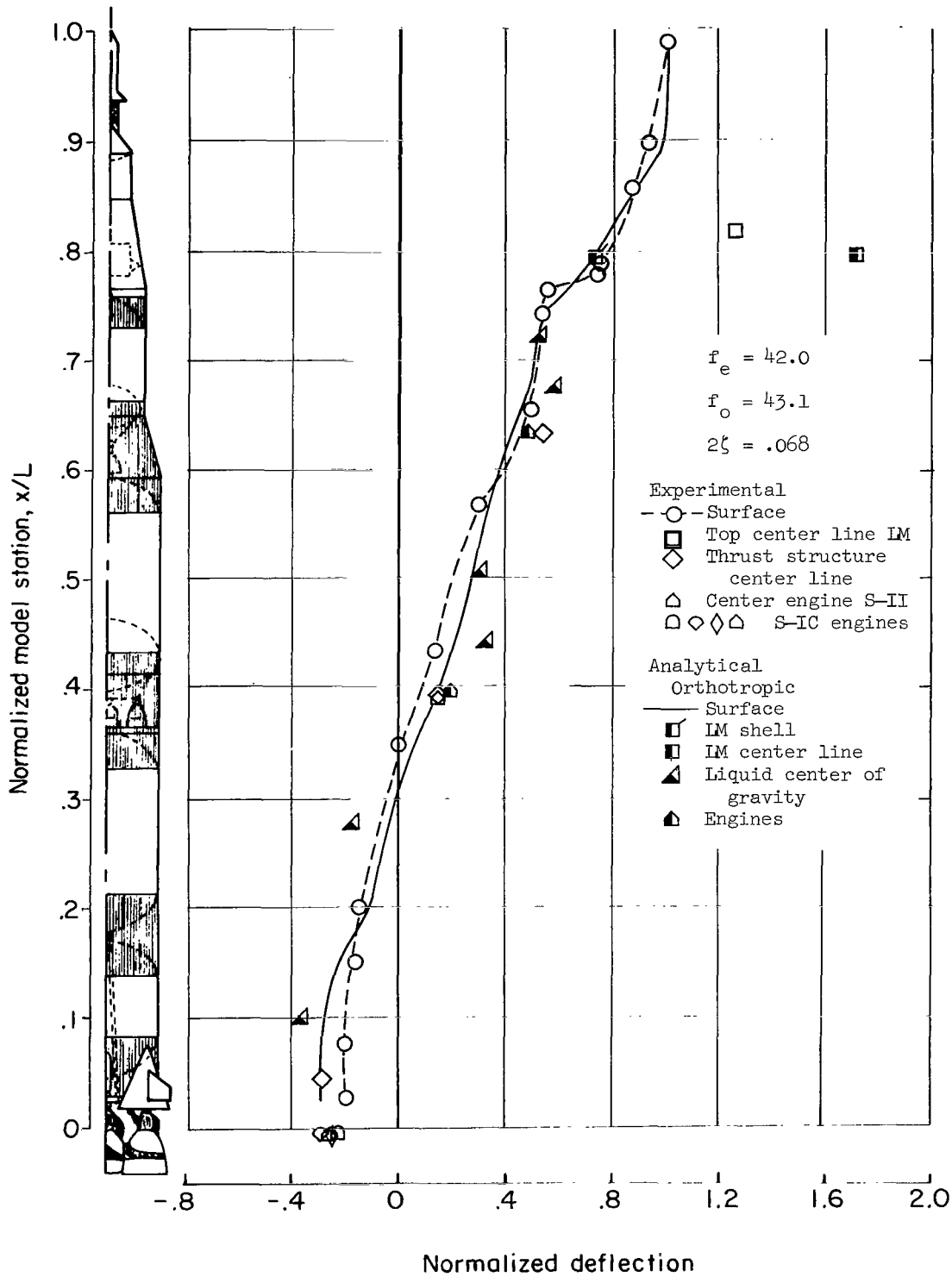

Figure 35.- Experimental and analytical deflection shapes for first resonance of 50-percent full condition.

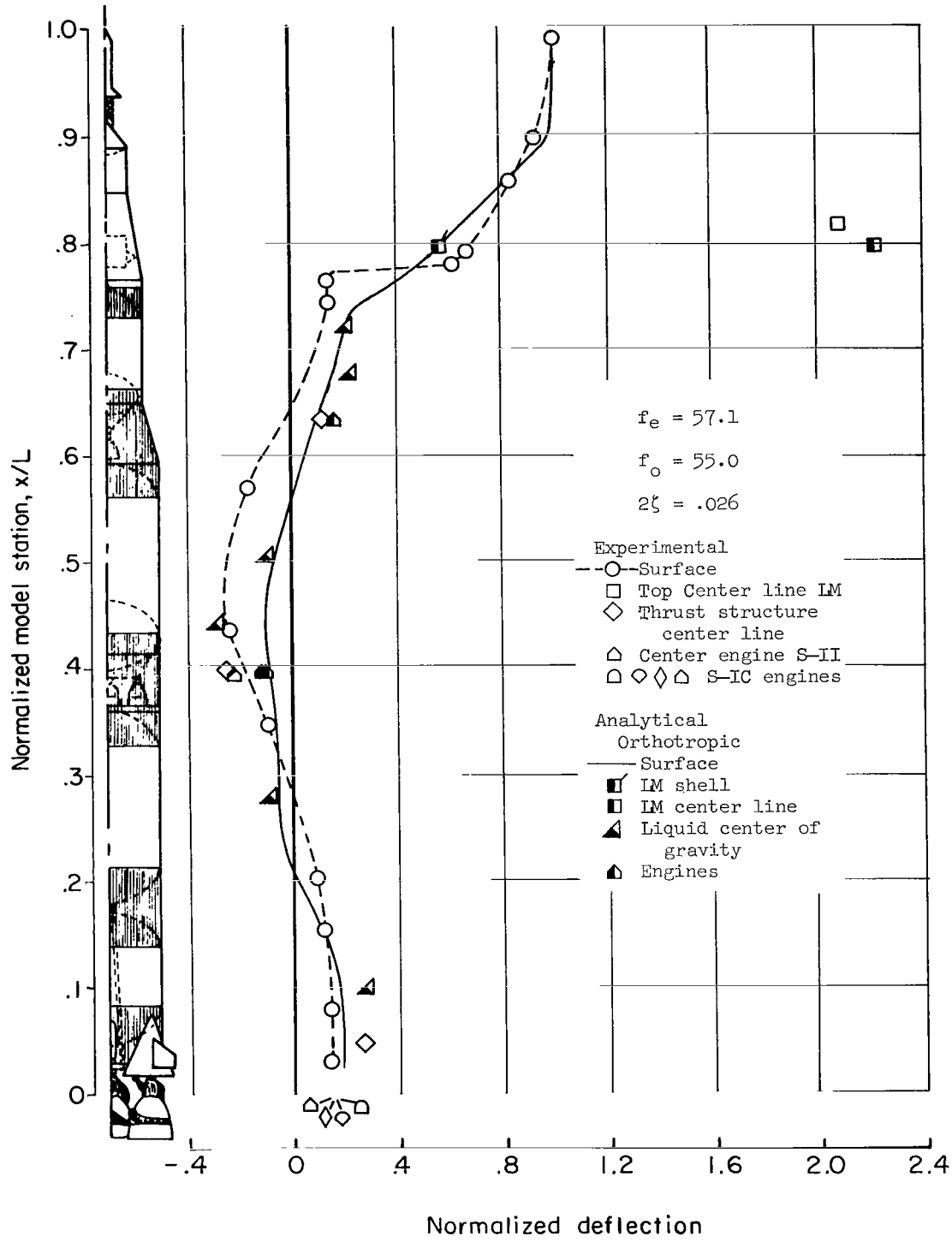

Figure 36.- Experimental and analytical deflection shapes for second resonance of 50-percent full condition.

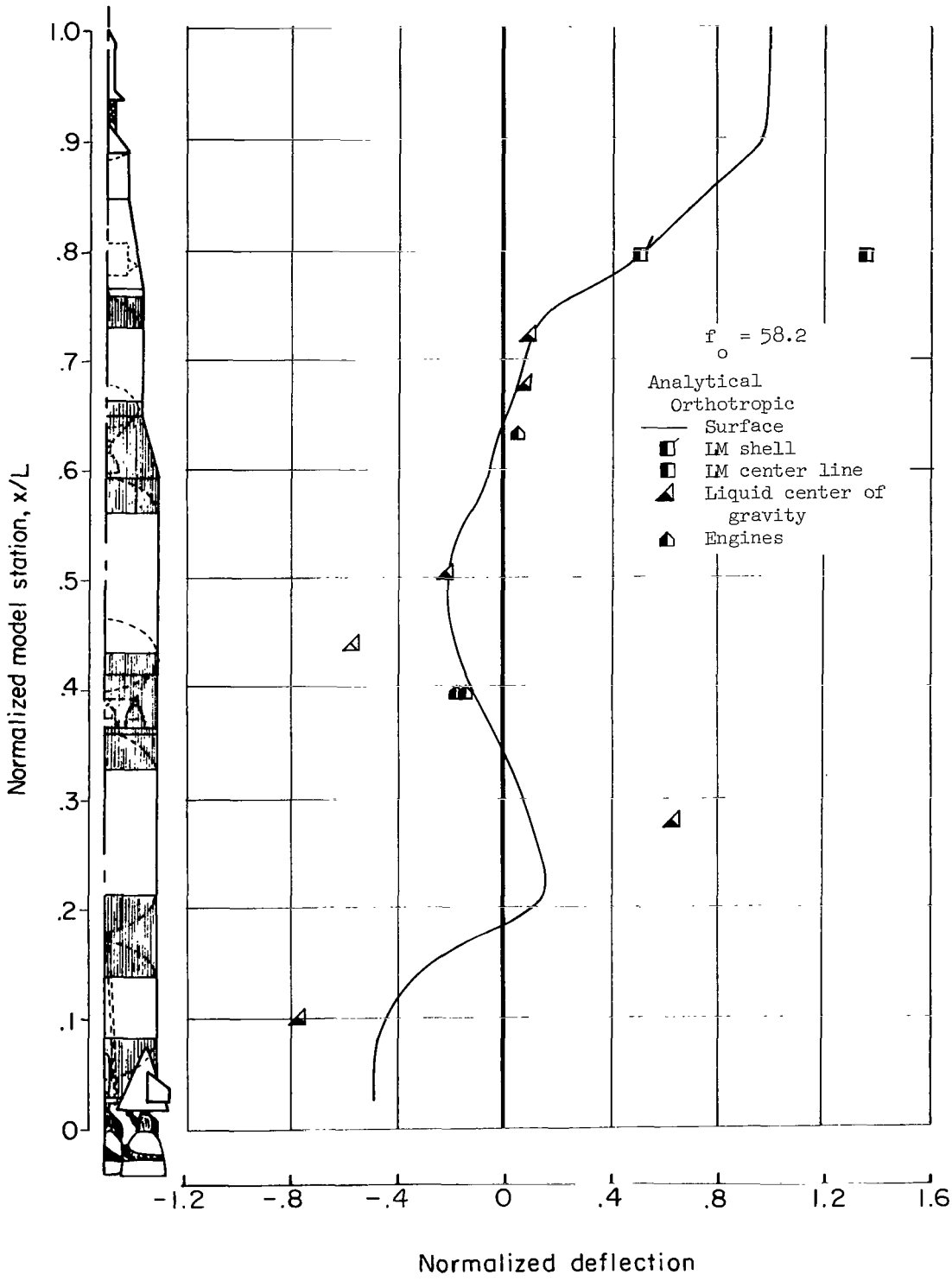

Figure 37.- Deflection shape for third calculated natural frequency of 50-percent full condition.

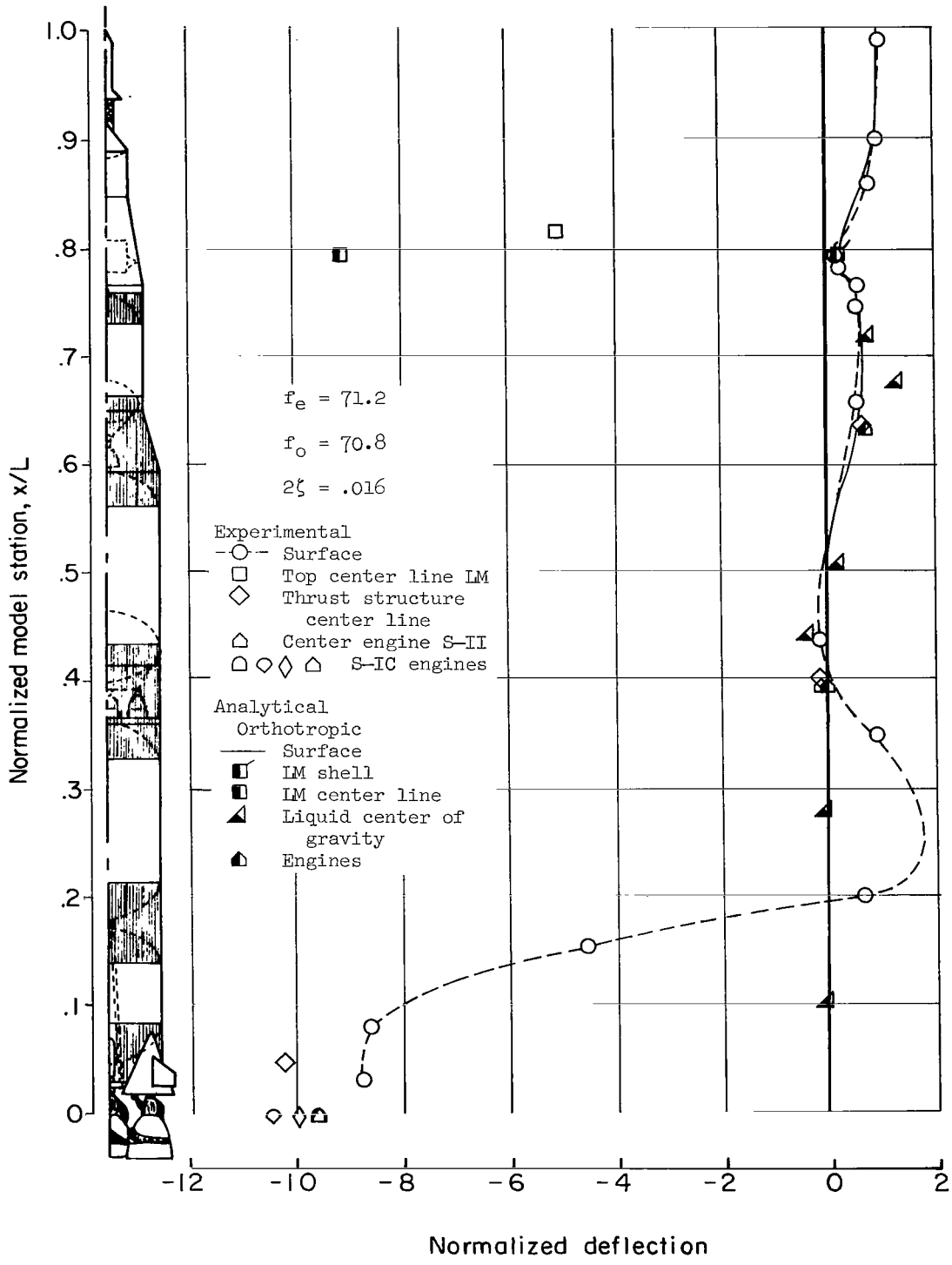

Figure 38.- Experimental and analytical deflection shapes for third experimental resonance of 50-percent full condition.

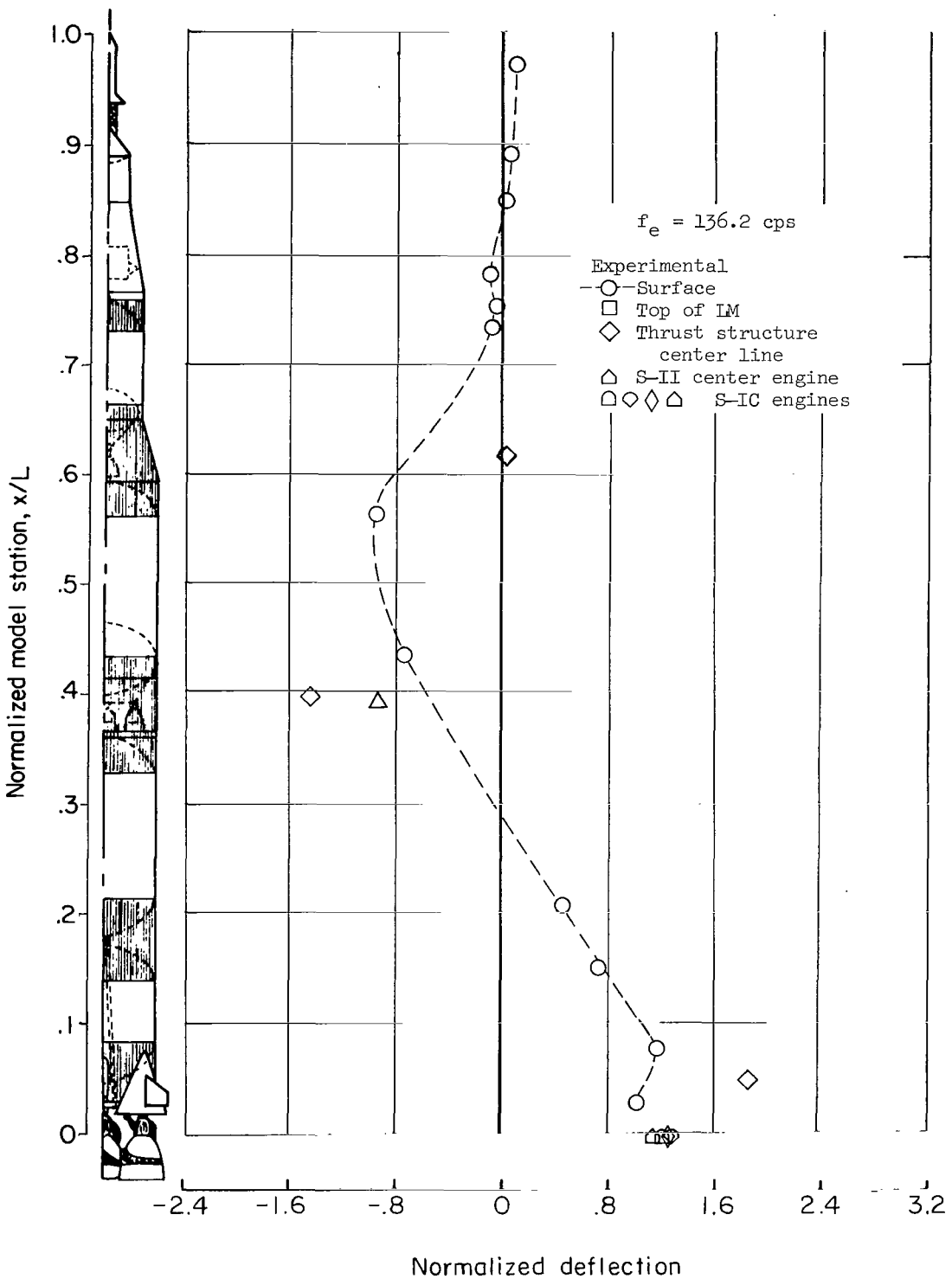

Figure 39.- Experimental deflection shape for fourth resonance of 50-percent full condition.

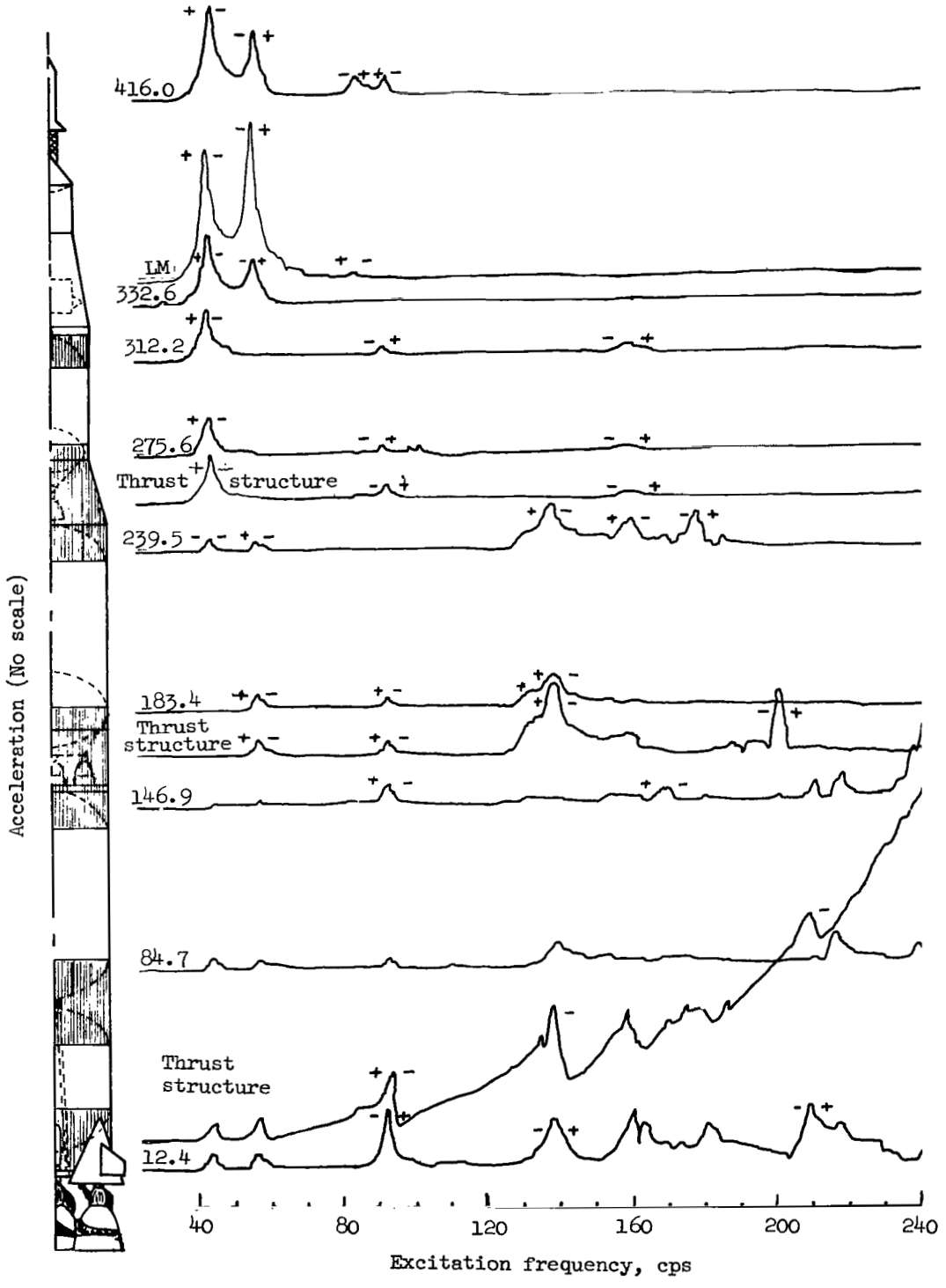

Figure 40.- Variation of acceleration with frequency. S-IC 25 percent full; force, 6 lb (27 N).

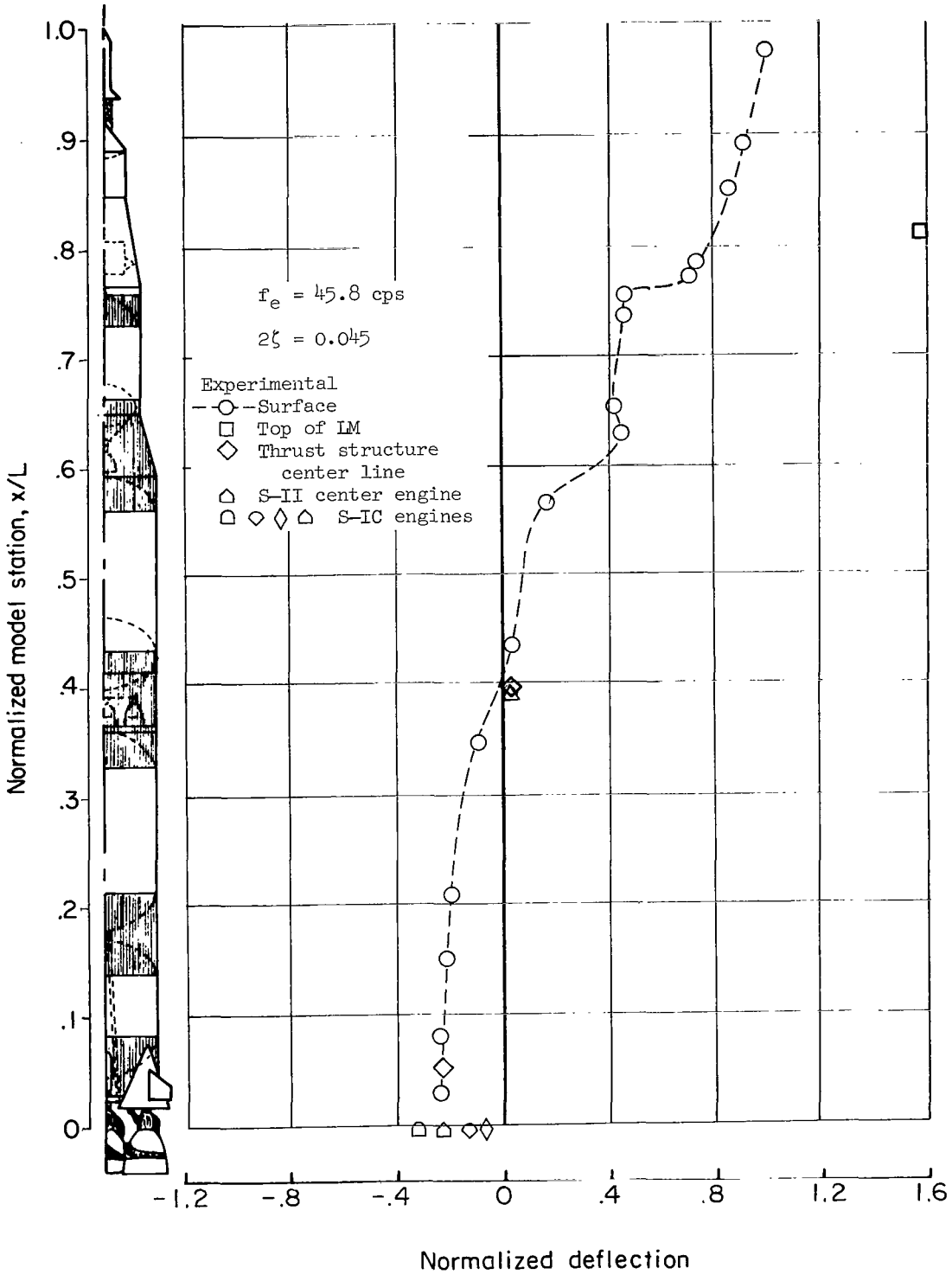

Figure 41.- Experimental deflection shape for first resonance of 25-percent full condition.

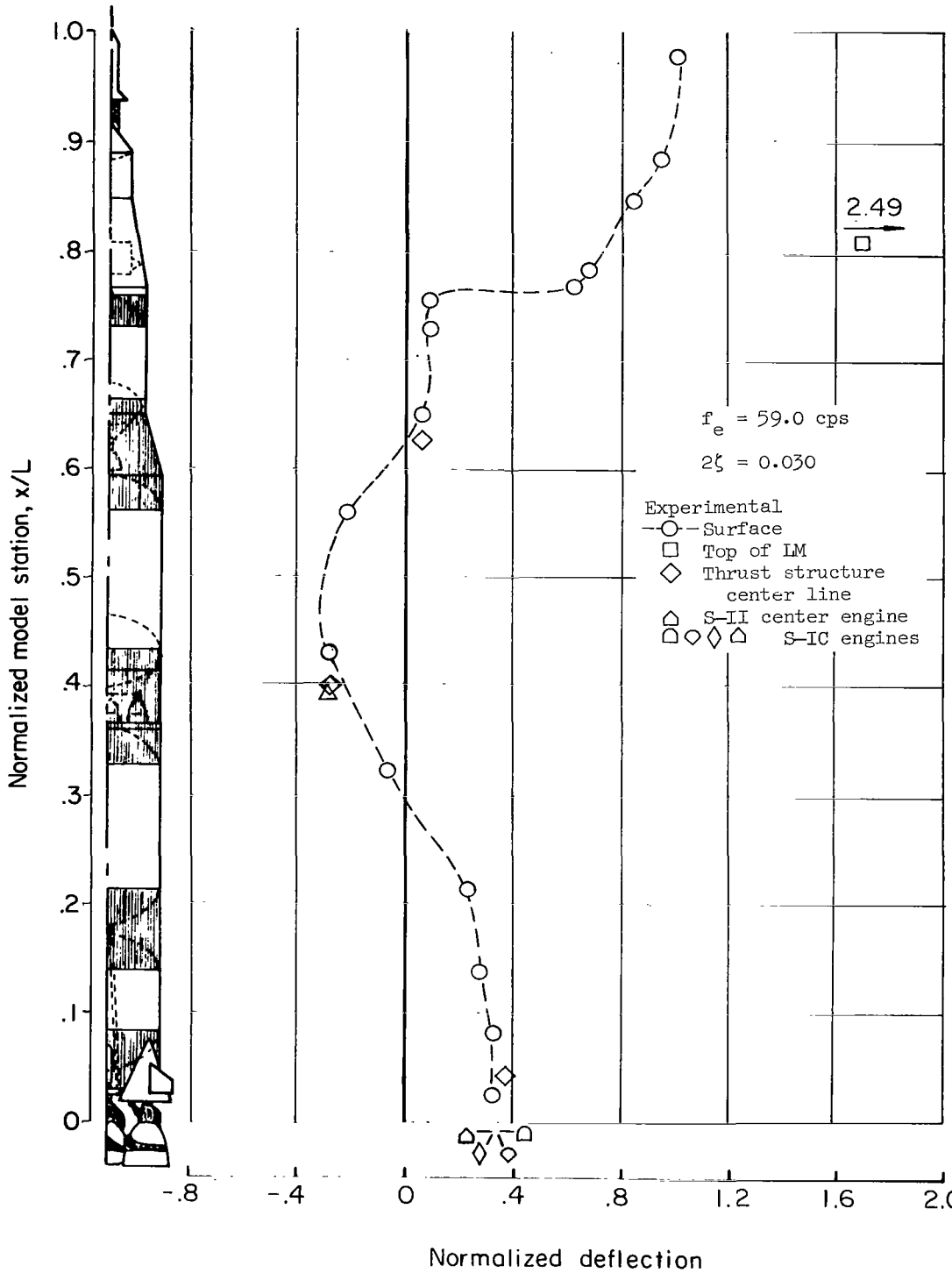

Figure 42.- Experimental deflection shape for second resonance of 25-percent full condition.

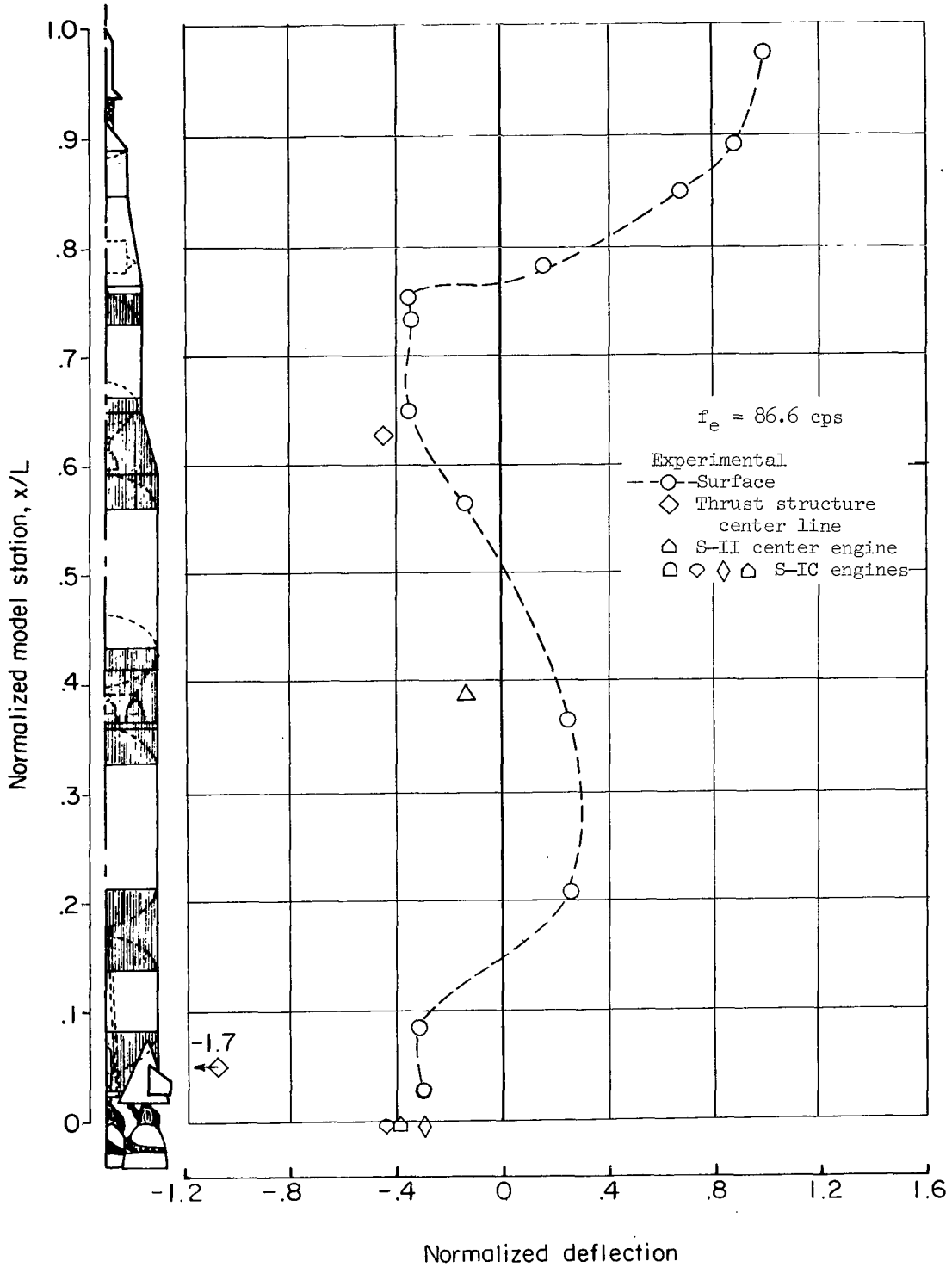

Figure 43.- Experimental deflection shape for third resonance of 25-percent full condition.

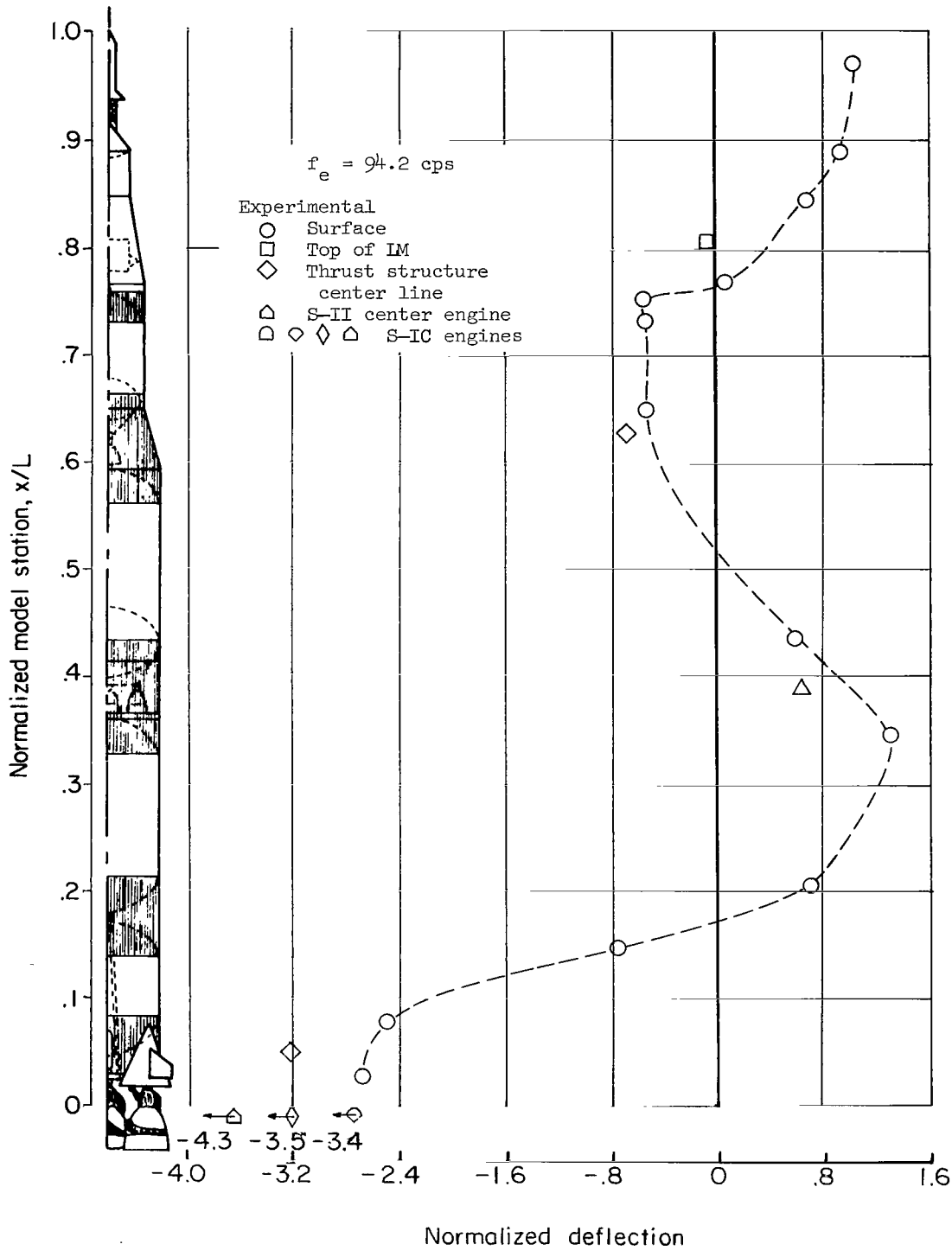

Figure 44.- Experimental deflection shape for fourth resonance of 25-percent full condition.

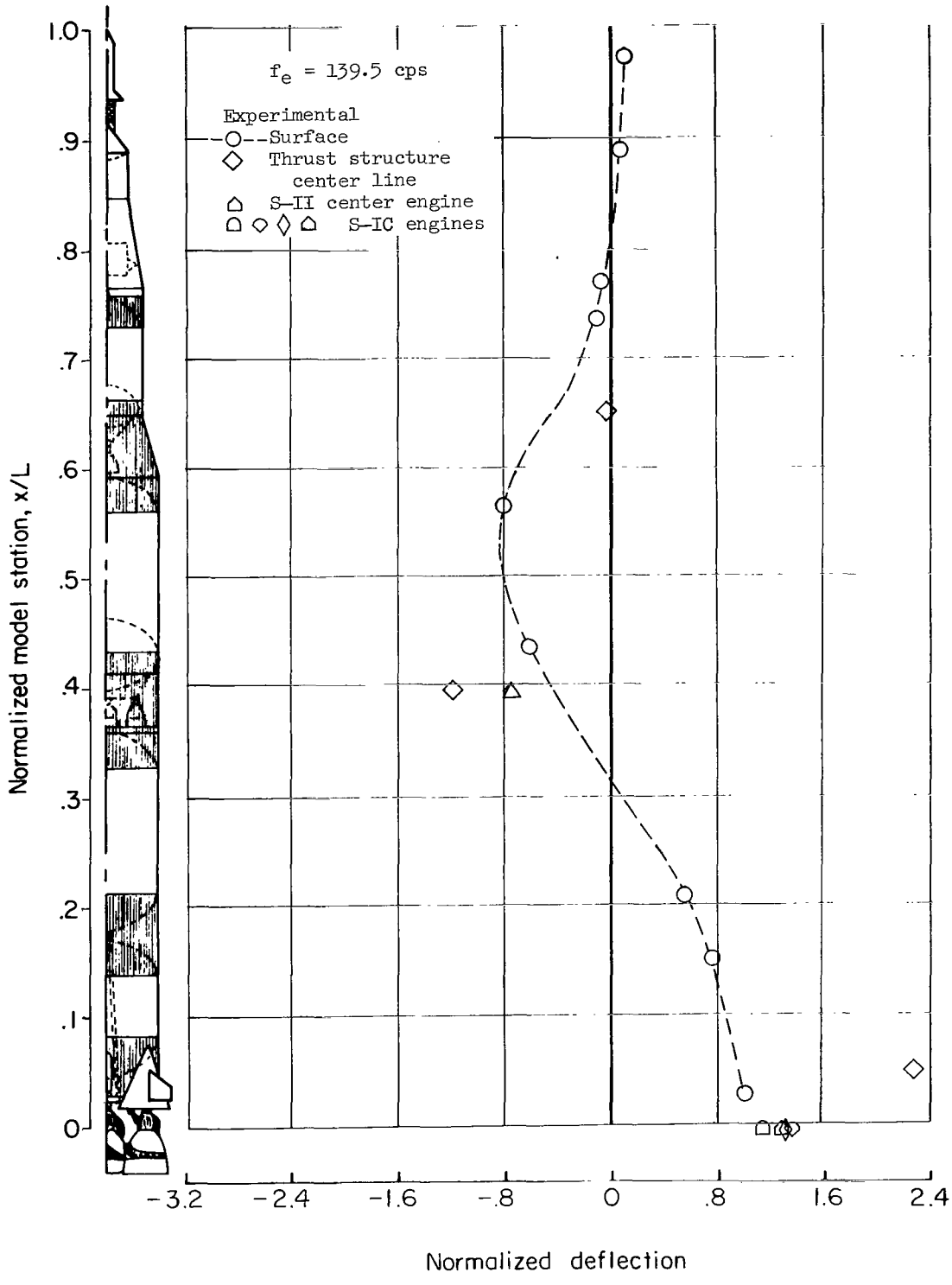

Figure 45 - Experimental deflection shape for fifth resonance of 25-percent full condition.

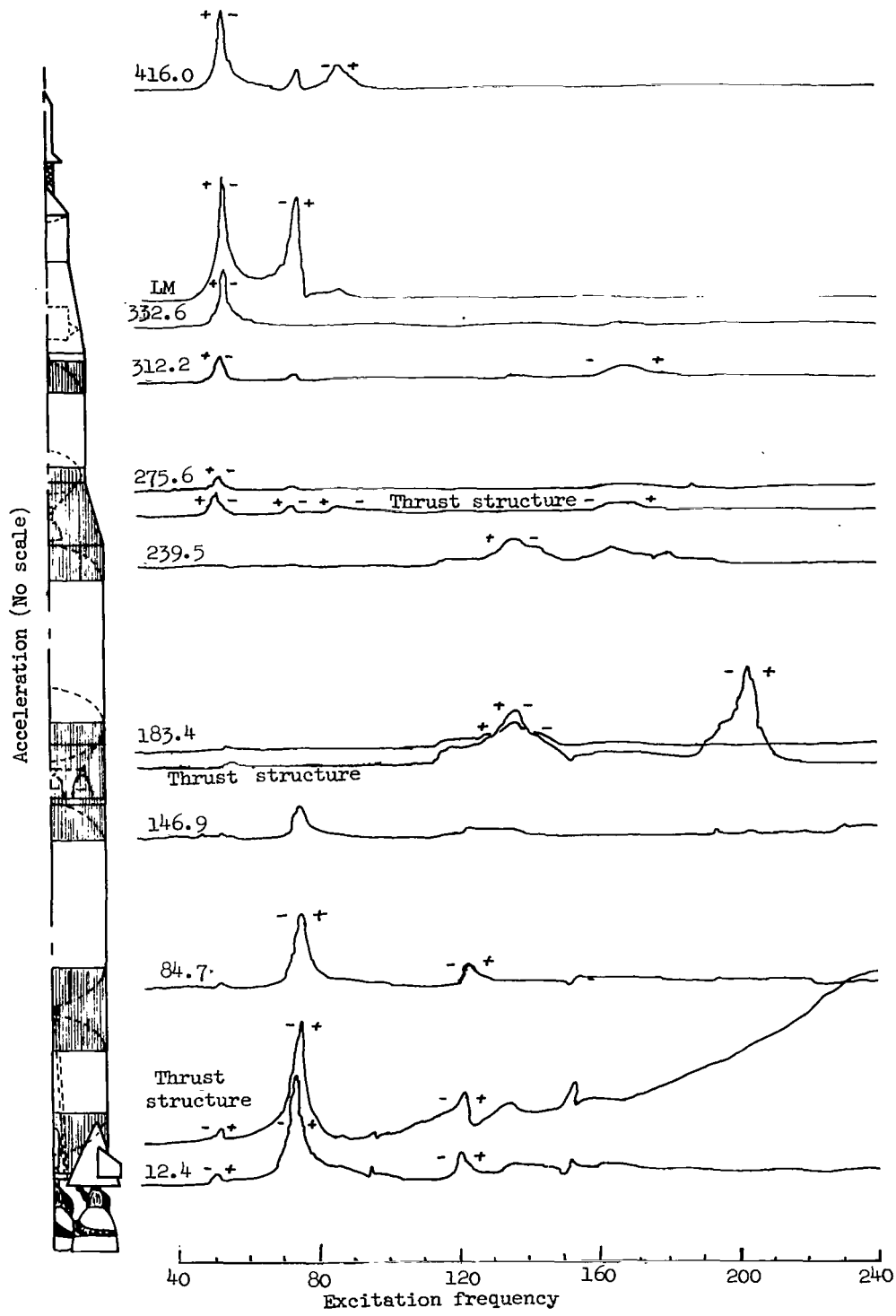

Figure 46.- Variation of acceleration with frequency for burnout condition. Force, 6 lb (27 N).

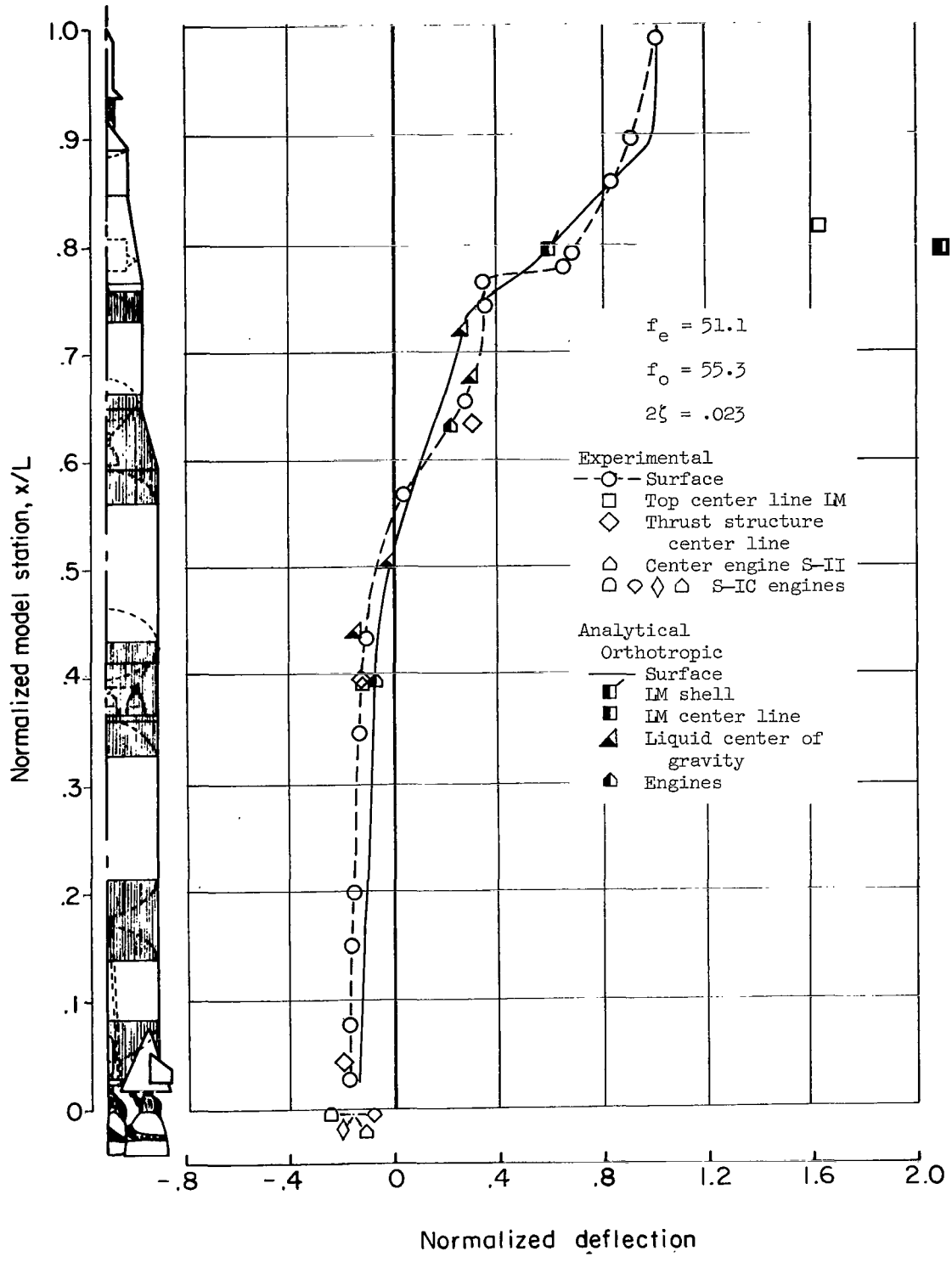

Figure 47 - Experimental and analytical deflection shapes for first resonance of burnout condition.

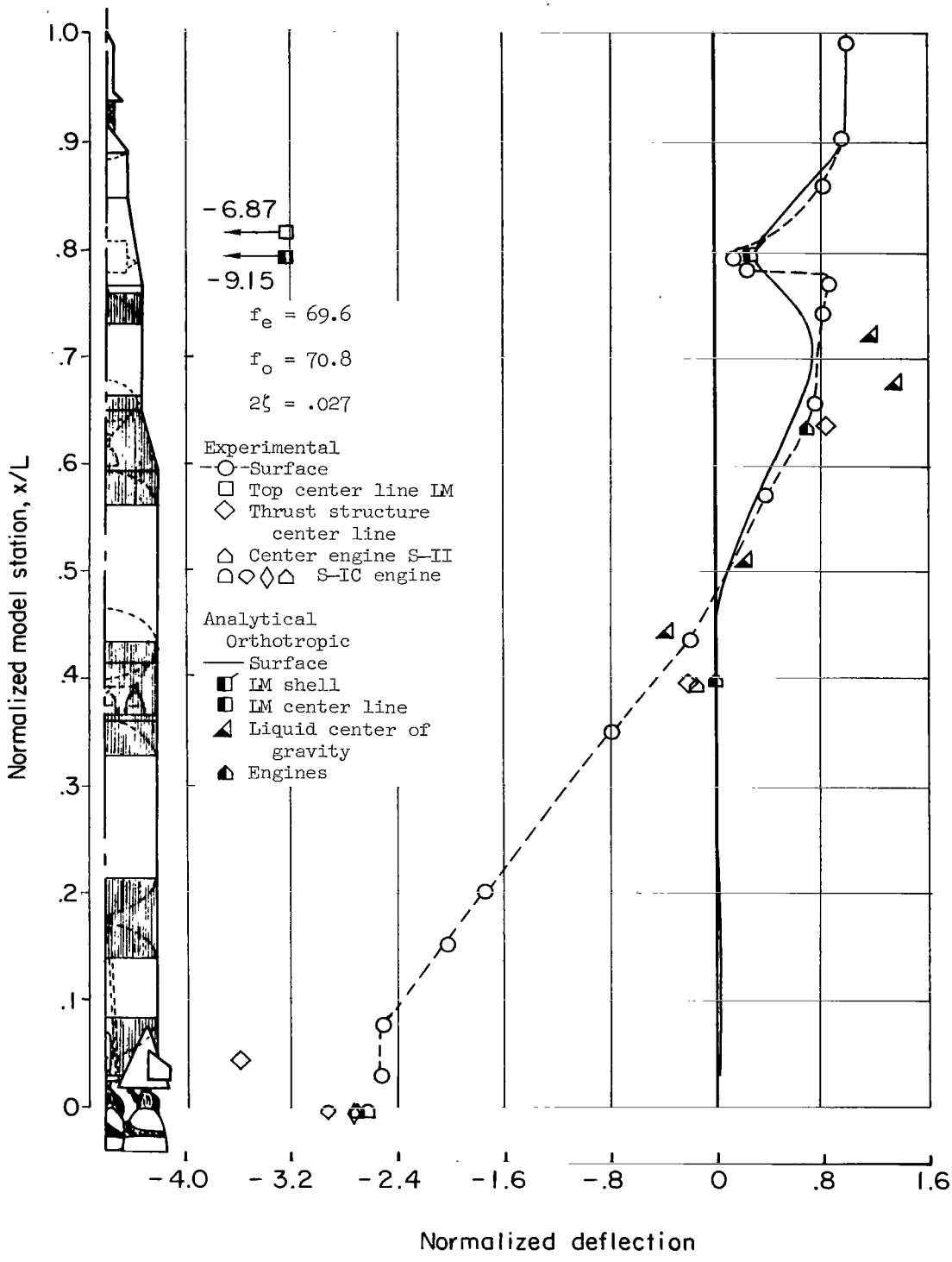

Figure 48.- Experimental and analytical deflection shapes for second resonance of burnout condition.

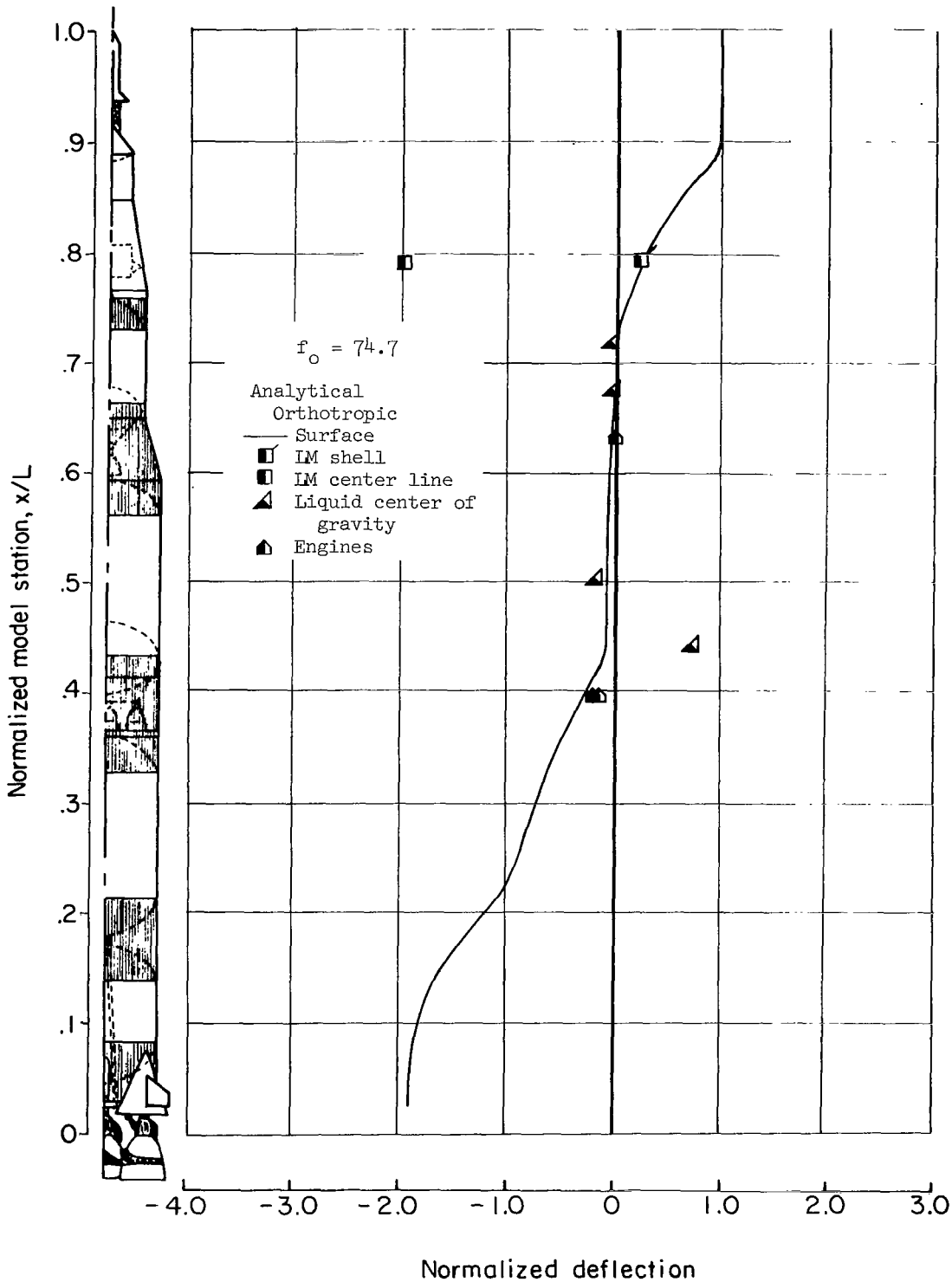

Figure 49.- Deflection shape for third calculated natural frequency of burnout condition.

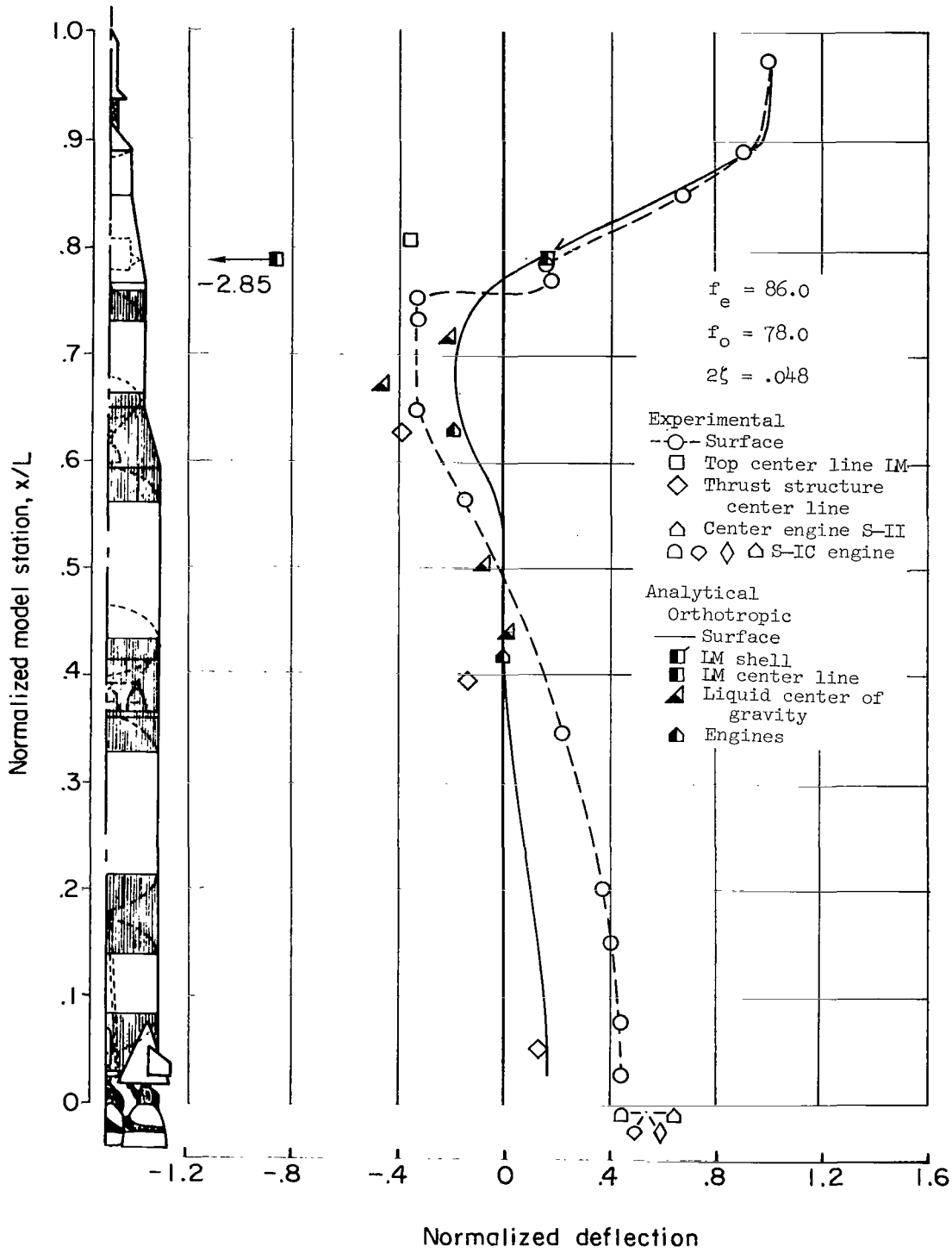

Figure 50.- Experimental and analytical deflection shapes for third resonance of burnout condition.

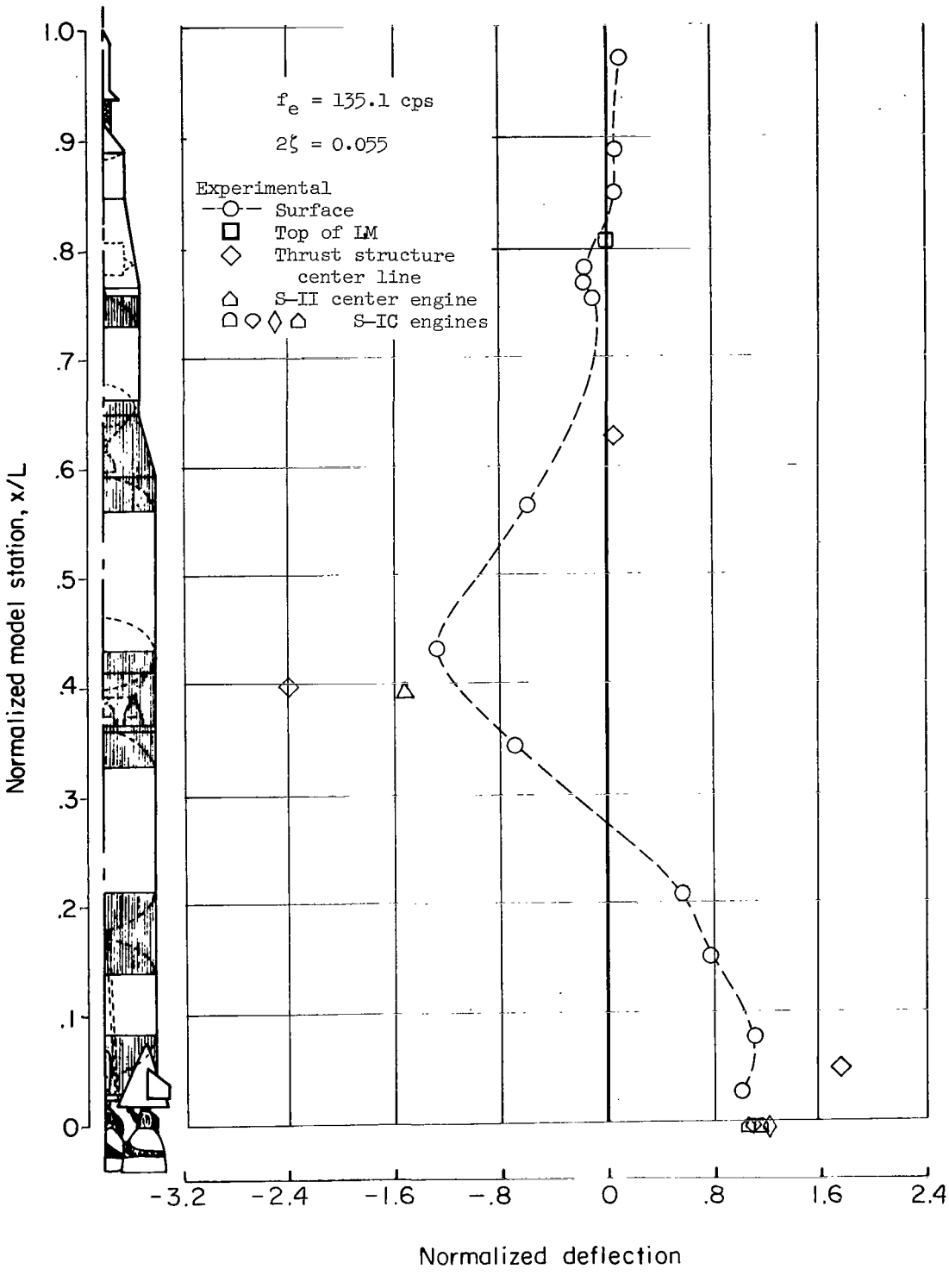

Figure 51.- Experimental deflection shape for fourth resonance of burnout condition.

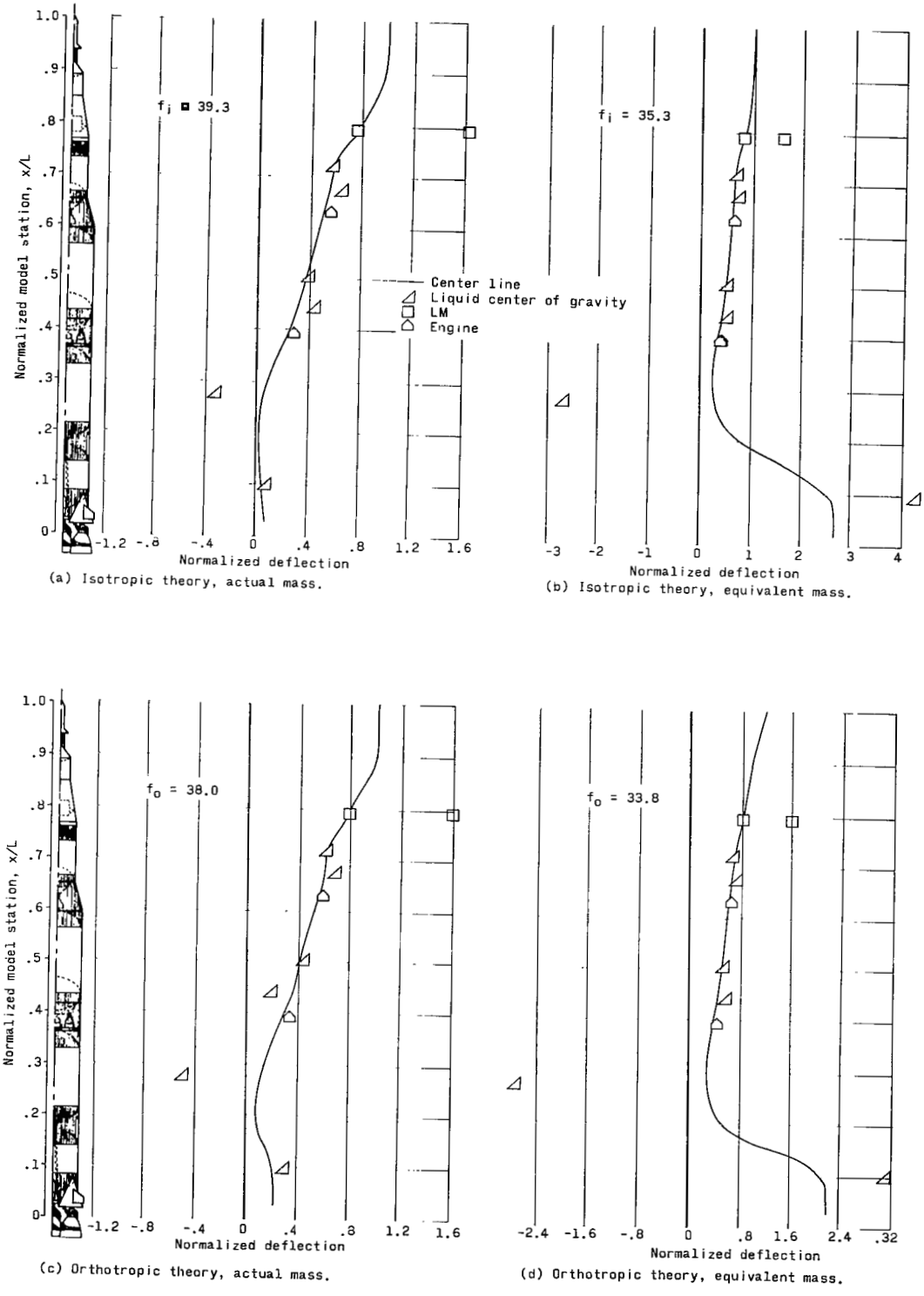

Figure 52.- Calculated natural frequencies and mode shapes for LOX mode.

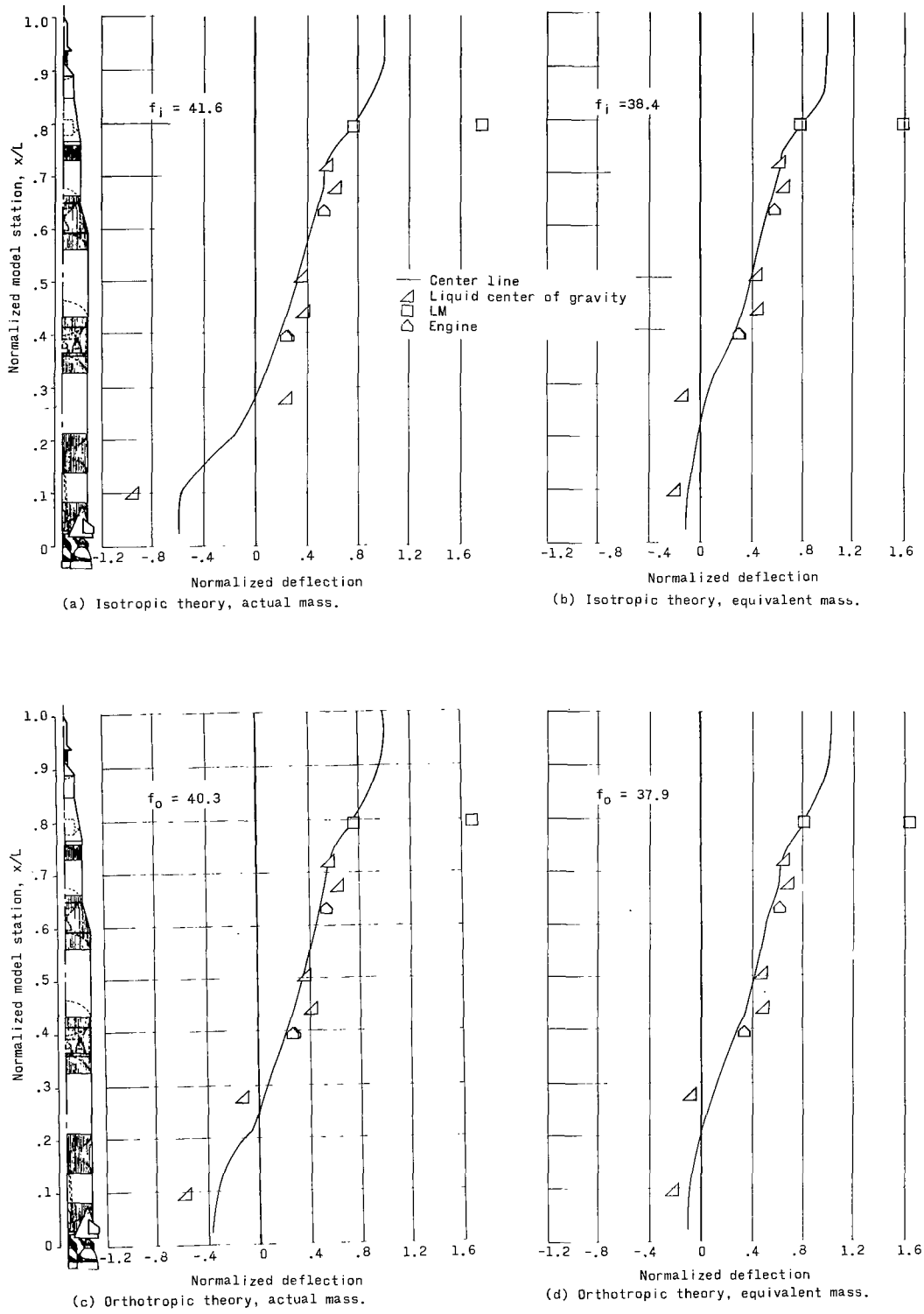

Figure 53.- Calculated natural frequencies and mode shapes for first structural mode.

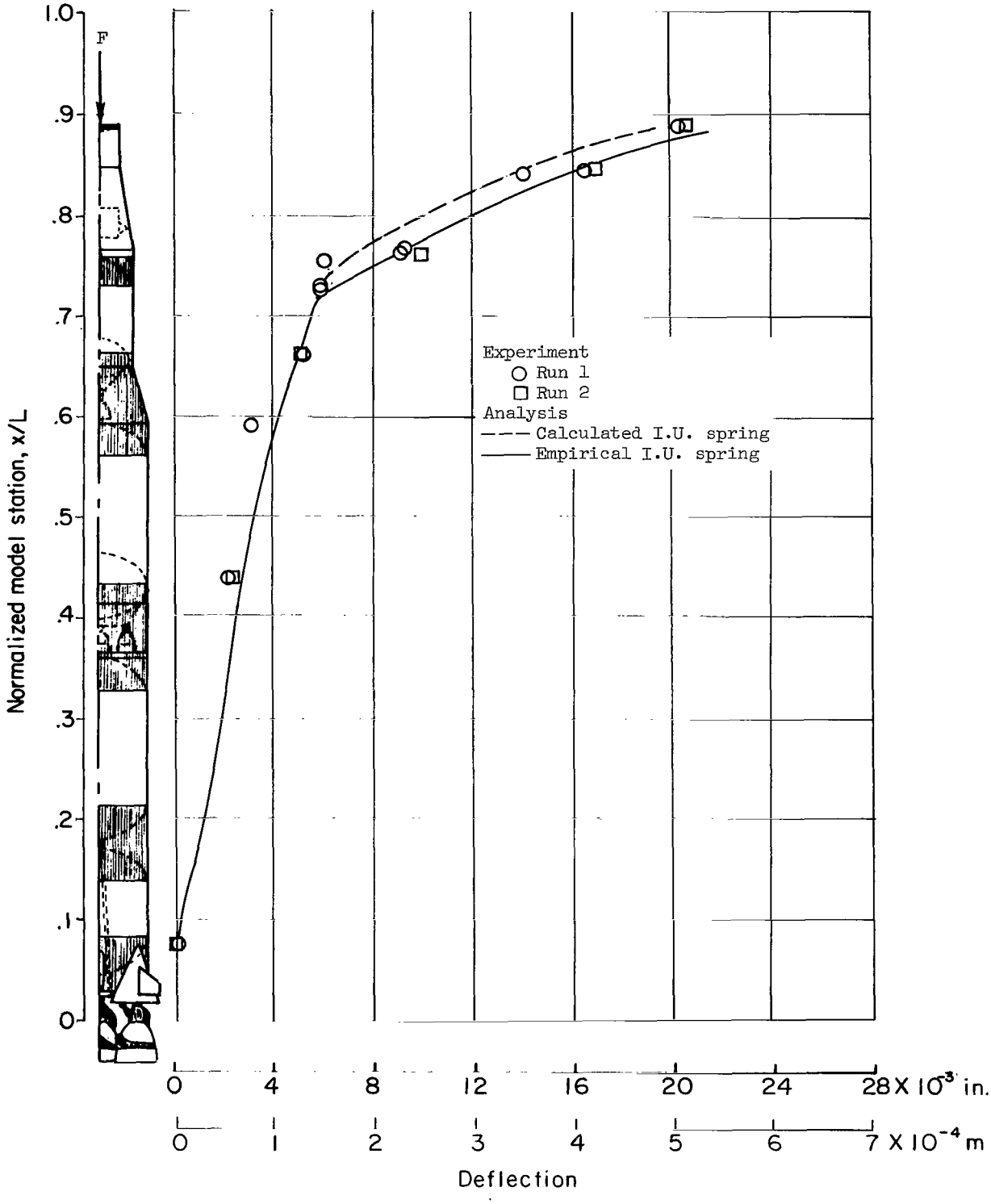

Figure 54.- Static deflection shape for 400 lb (1780 N) longitudinal load at $\frac{x}{L} = 0.88$.

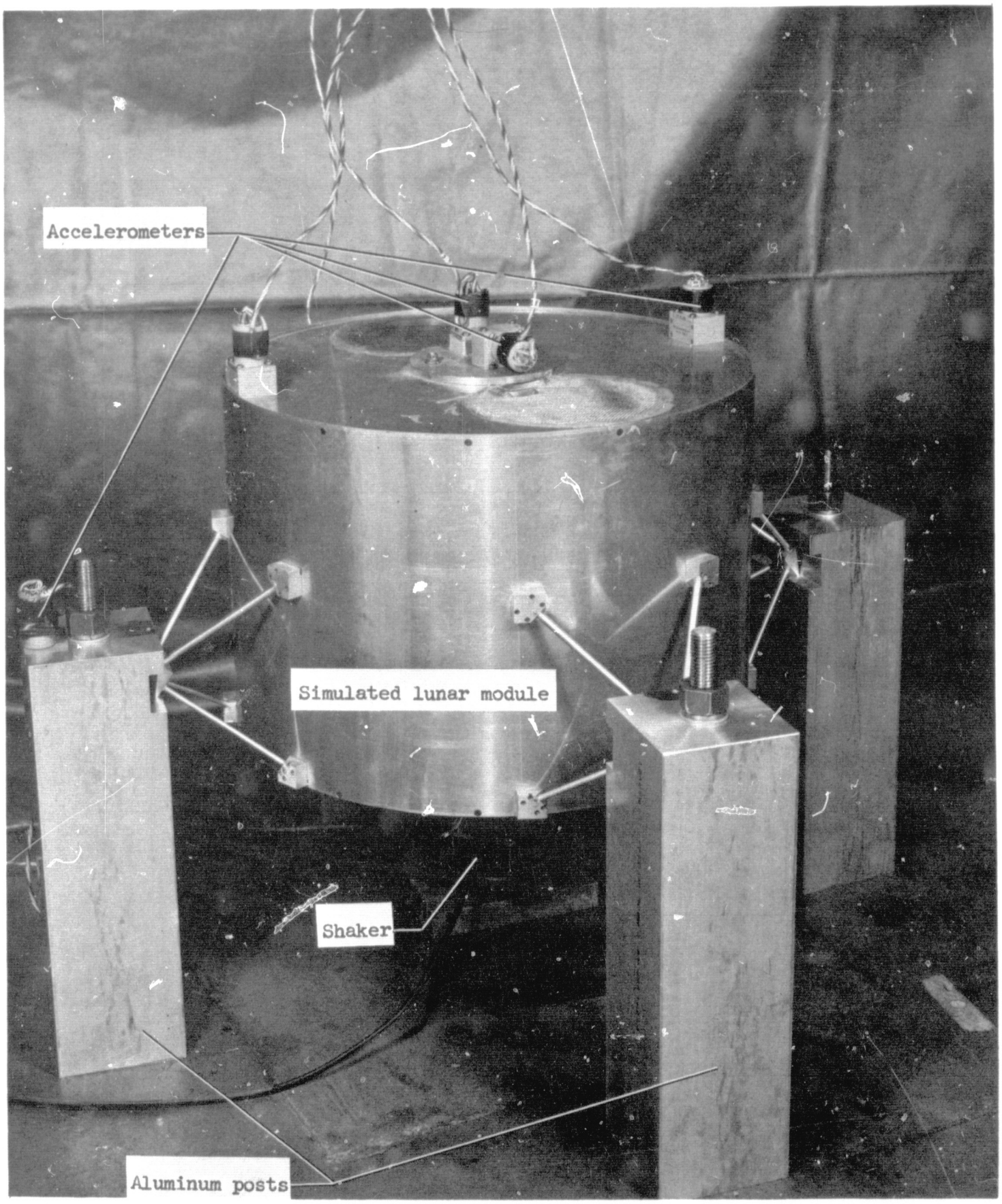

Figure 55.- Test apparatus. LM on rigid posts. L-69-1223

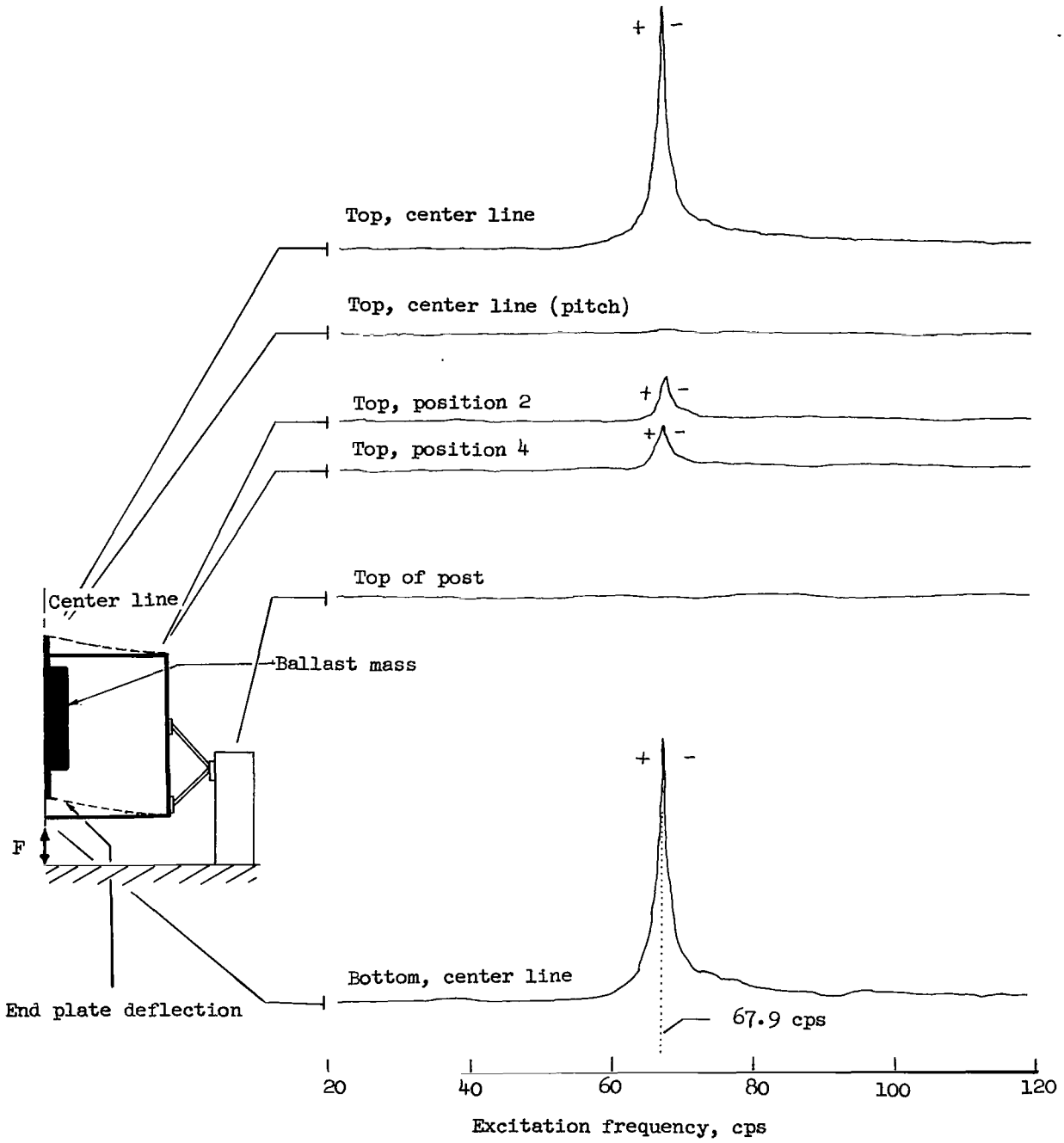

Figure 56.- Variation of acceleration with frequency for longitudinal excitation of simulated LM mounted on rigid posts.

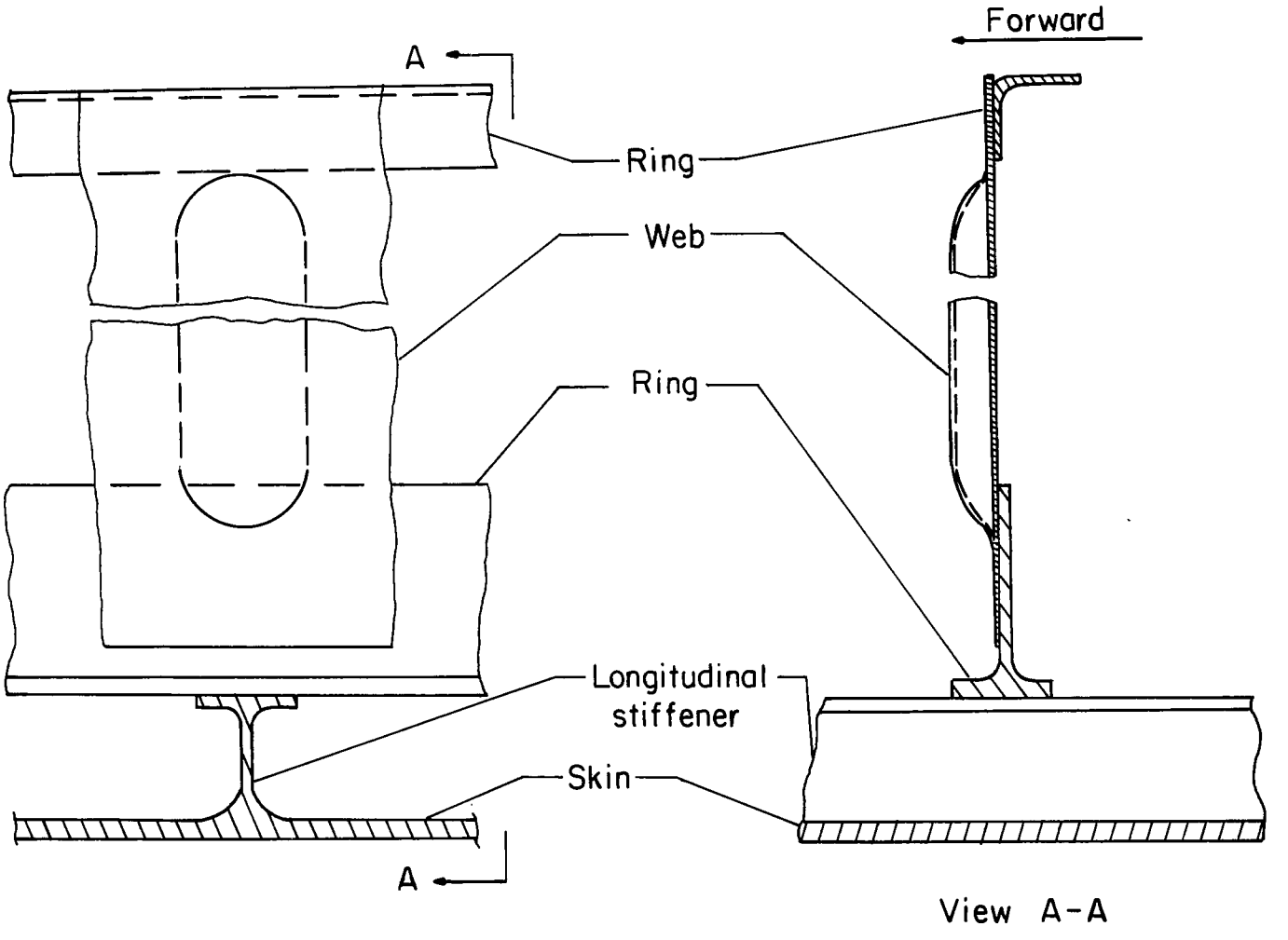

Figure 57.- Repeating elements of S-IC LOX tank.

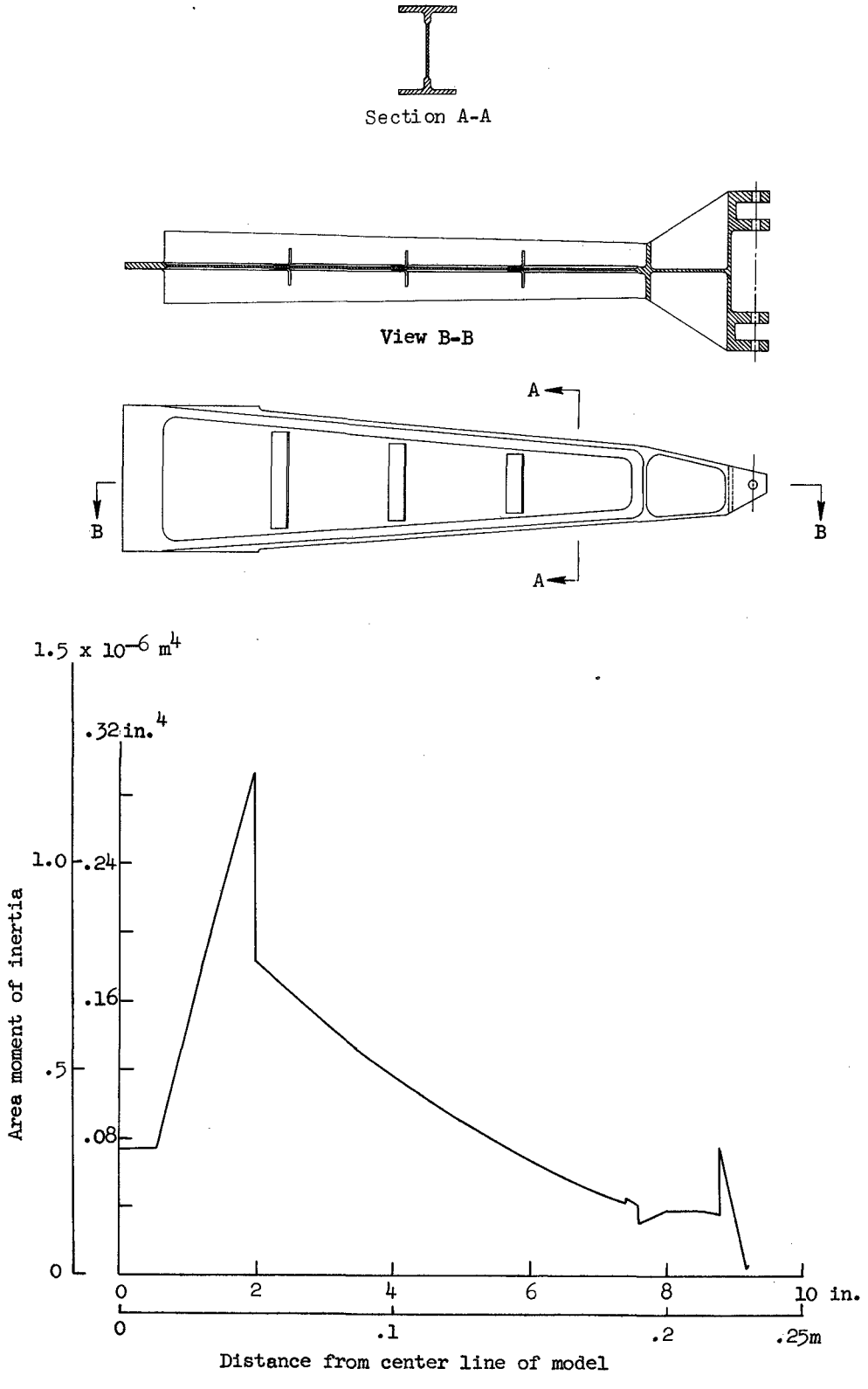

Figure 58.- Configuration and moment of inertia of one S-II cross beam.